Bose-Einstein condensation and the atom laser

A thesis submitted for the degree of
Doctor of philosophy at the Australian National University

Nicholas P. Robins

Canberra, April 14, 2004

Declaration

This thesis contains no material which has been accepted for the award of any other degree or diploma in any university. To the best of the authors knowledge, it contains no material previously published or written by another person, except where due reference is made in the text. The research has been conducted under the supervision of Dr. John Close, Dr. Craig Savage and Prof. Yuri Kivshar.

Nicholas P. Robins
April 14, 2004

Acknowledgements

My deepest gratitude and thanks go to my three supervisors, John Close, Craig Savage, and Yuri Kivshar, for all the opportunities you gave me to become a better physicist. At different stages in the three years of my PhD, each one of you has fulfilled the role of primary supervisor, and not once in that time have my questions been unanswered or your answers been incomprehensible.

Theoretical modeling of an atom laser is fun, but, for me, making one was better. Thank you to John Close for trusting my conviction that I could do the job, and for giving me the opportunity to join the 'dark side'.

My best wishes go to my fellow students, in particular Cameron (are you antagonising me?) Fletcher, Jessica (Frisbee) Lye, Simon (my atom laser is better than yours) Haine and Adele (Hmmm) Morrison. My thanks go also to Joseph Hope and Hans Bachor for taking part in my scientific development.

Finally, to my wife Lena and daughter Nina, I thank you for your support, unconditional love, and carrot muffins with a pecan nut on top.

Abstract

The research presented in this thesis describes primarily experimental investigations of ultra-cold atoms from an atom laser perspective. In Chapters 1 and 2, we outline the background theory required to understand the contents of later chapters, and although much of the information can be found elsewhere, it is presented here for completeness. Chapter 3 presents a detailed description of the construction and operation of the 'atom laser' upgrade of our double MOT machine for producing Bose-Einstein condensates. This second generation BEC machine replaced or significantly improved all facets of the machine, except vacuum setup, computer control and the base laser system. Specifically addressed are the construction and implementation of an Ioffe-Pritchard magnetic trap and associated switching and a completely new optics system (collection and science MOTs, pumping and imaging). The final part of this chapter presents evidence for BEC in the new system, including a detailed discussion related to extracting quantitative data from images of Bose condensed atoms. Chapter 4 describes the production of an atom laser. The implementation of both continuous and pulsed atom lasers using radio-frequency output coupling is presented. This chapter investigates in detail the multi-component flux limiting dynamics of a pulsed atom laser and presents the first detailed comparison between an atom laser experiment and a full three-dimensional GP simulation of the system (performed by Dr. Craig Savage). Chapter 5 relates to the pumping of an atom laser. We demonstrate with an original theoretical model that three body recombination acts to stabilise the pumped atom laser in much the same way as gain saturation stabilises the output of an optical laser. Chapter 6 discusses the design and partial construction of our next generation atom laser machine, and includes a detailed procedure for optimising the efficiency (power generated versus geometric trapping frequency) of a QUIC magnetic trap for atom laser studies. Two appendices follow the final chapter. Appendix 1 presents a new modulation free laser locking technique (a system central to producing a BEC). Appendix 2 details the numerical methods used in this thesis.

Publications

The research carried out for this PhD thesis spanned both theoretical and experimental physics. This led to the publication of 5 papers related to the theoretical dynamics of multiple spin state Bose-Einstein condensates (BEC), including atom lasers, and 4 experimental papers on atom lasers and related techniques. The diverse nature of the topics covered, reflect a change from theoretical to experimental physics half way through my PhD. In order to produce a cohesive document, a judicious selection of material was essential. Starred publications, in the list below, have been emphasised in this thesis.

- A model of a pumped continuous atom laser, N. Robins, C. Savage, E. Ostrovskaya, in "Directions in Quantum Optics : A Collection of Papers Dedicated to the Memory of Dan Walls", eds. H. Carmichael, R. Glauber, M. Scully (Springer, 2000).
- *Atom laser dynamics, N. P. Robins, C. Savage, and E. A. Ostrovskaya, Phys. Rev. A, **64** 043605 (2001).
- Modulational instability of spinor condensates, N. P. Robins, W. Zhang, E. A. Ostrovskaya, and Y. S. Kivshar, Phys. Rev. A, **64** 021601 (2001).
- Stability of continuously pumped atom lasers, S. A. Haine, J. J. Hope, N. P. Robins, C. M. Savage, Phys. Rev. Lett., **88** 170403 (2002).
- A self-locked magneto-optic trap, C. S. Fletcher, J. E. Lye, N. P. Robins , and J. D. Close, Opt. Commun. **212** 85 (2002).
- *Interferometric, modulation-free laser stabilization, N. P. Robins, B. J. J. Slagmolen, D. A. Shaddock, J. D. Close, M. B. Gray Optics Letters, **27** 1905 (2002).
- Bose-Einstein condensate collapse: a comparison between theory and experiment, C. M. Savage, N. P. Robins, and J. J. Hope, Phys. Rev. A, **67** 014304 (2003).
- *Dynamical effects of back-coupling on an atom laser, N. P. Robins, J. E. Lye, C. S. Fletcher, S. A. Haine, J. Dugue, C. Breme, J. J. Hope and J. D. Close, in "Laser Spectroscopy - Proceedings of the XVI International Conference

(ICOLS 2003)" P. Hannaford, A. Sidorov, H. Bachor, and K. Baldwin eds., (World Scientific Publishing, Singapore, 2004).

- *Classical noise and flux: the limits of multi-state atom lasers, N. P. Robins, C. M. Savage, J. J. Hope, J. E. Lye, C. S. Fletcher, S. A. Haine, and J. D. Close, (submitted, see cond-mat/0311361).

Contents

Acknowledgements i

Abstract iii

Publications v

1 Introduction **15**
- 1.1 Motivation: the pumped atom laser . . . 15
- 1.2 Bose-Einstein statistics . . . 16
- 1.3 BEC and the macroscopic wavefunction . . . 17
- 1.4 BEC and ultra-cold atoms . . . 18
- 1.5 Experimental History of BEC . . . 19
- 1.6 The definition of an atom laser . . . 19
  - 1.6.1 The optical laser . . . 20
  - 1.6.2 Properties of a generic laser beam . . . 21
  - 1.6.3 An ultra-cold laser . . . 23
  - 1.6.4 The theory of atom lasers . . . 26
  - 1.6.5 The continuously pumped atom laser . . . 27
- 1.7 This thesis . . . 27

2 Experimental and theoretical background **29**
- 2.1 Atomic properties and hyperfine structure of ^{87}Rb . . . 29
- 2.2 Pushing atoms around . . . 30
- 2.3 Optical molasses & the magneto-optical trap . . . 31
  - 2.3.1 Doppler and sub-Doppler cooling . . . 31
  - 2.3.2 Polarisation gradients . . . 33
  - 2.3.3 The magneto-optic trap . . . 35
  - 2.3.4 The limits of optical cooling . . . 36
- 2.4 Magnetic trapping . . . 37
  - 2.4.1 The Ioffe-Pritchard configuration trap . . . 39
- 2.5 Forced evaporative cooling . . . 40
  - 2.5.1 Losses and magnetic trap lifetimes . . . 41
- 2.6 Calculating numbers and temperatures . . . 42
  - 2.6.1 Calculating the atom number . . . 42

2.6.2 Temperature calculations 43
2.7 The Gross-Pitaevskii equation 45
2.8 Atom laser output coupling 46
2.8.1 Raman output coupling 47

3 The atom laser source 49
3.1 Magnetic trap MkII 49
3.1.1 Trap construction 51
3.1.2 Coil geometry 53
3.2 Trap characterisation 53
3.2.1 Power dissipation 53
3.2.2 Magnetic field strength 56
3.2.3 Measurement of trap frequencies 56
3.2.4 Magnetic trap lifetime 57
3.3 Magnetic trap switching scheme 59
3.4 Optical pre-cooling 60
3.4.1 Fluorescence measurement of atom number 62
3.4.2 The laser system 64
3.4.3 Upper MOT 64
3.4.4 Push loading 65
3.4.5 Optimising a single push 66
3.5 Lower MOT 68
3.5.1 The repumper 69
3.6 Three steps to stability 69
3.6.1 Retro-reflection lower MOT 69
3.6.2 Polarizing beam splitters 70
3.6.3 Gaussian beam profiles 70
3.7 Optical pumping 71
3.8 New imaging system 71
3.9 Summary of optical pre-cooling and transfer 72
3.10 Evaporative cooling 73
3.11 Fitting to column density 74
3.12 Bose-Einstein condensation 76
3.12.1 Sudden increase in optical depth 77
3.12.2 Bimodal distribution 77
3.12.3 Anisotropic expansion 77

4 The atom laser 81
4.1 Output coupling 82
4.1.1 The resonant width of the condensate 82
4.2 The model 83
4.2.1 Transforming to lower dimensions 84
4.3 The Rabi frequency 85
4.4 Production of a pulsed atom laser 88
4.5 Classical noise and flux: the limits of multi-state atom lasers 90

4.5.1 Experimental results 90
4.5.2 Theoretical results 93
4.5.3 Conclusion 94

5 Pumping an atom laser 97
5.1 The model 98
5.1.1 Numerical results 100
5.2 Conclusion 103

6 Next generation atom laser machine 105
6.1 Design philosophy 105
6.2 An optimized QUIC trap for BEC 106
6.2.1 Three loop QUIC trap 106
6.2.2 The ideal QUIC trap and figures of merit 110
6.2.3 Geometrical considerations 112
6.2.4 Concrete examples 114
6.2.5 Construction techniques 115
6.2.6 Experimental verification 115
6.2.7 Conclusions 116
6.3 Overview of the new system 117

7 Conclusions and outlook. 119

Appendices

A Atomic tilt locking 121
A.1 Background 121
A.2 Tilt locking 122
A.3 Atomic phase shift 123
A.4 Experimental setup and results 124
A.5 Conclusion 125

B Numerical Methods 127
B.1 Overview of the chapter 127
B.2 The split-step Fourier method 128
B.2.1 The approximation 128
B.2.2 Implementation for a generic NLS equation 128
B.2.3 Split-step scheme for the atom laser model 129

Bibliography 131

CHAPTER 1

Introduction

1.1 Motivation: the pumped atom laser

In 1995, a new state of matter, a Bose-Einstein condensate (BEC), was created [1]. BEC is a collection of ultra-cold dilute neutral atoms that occupy the same quantum state, which is usually the ground state of the potential of a confining magnetic trap. In this state, the de-Broglie wavelength of the individual atoms become comparable to the dimension of the entire atomic cloud. The atoms are no longer distinguishable and acquire collective properties, similar to those of photons in a coherent light wave produced by an optical laser. A consequence of BEC is that this giant ($\sim 10^6$ atoms) coherent matter wave can be released from the trap without disturbing the coherence. Then a directional beam of coherent, bright, spectrally narrow atoms forms an 'atom laser'. The output of an atom laser is a coherent matter wave where the wavelength is the de-Broglie wavelength of the atoms. We call it a laser by analogy with the device we are more familiar with, an optical laser (first demonstrated by Maiman in 1960 [2]), where a large number of photons are built up and stored in the laser cavity and are extracted continuously in order to form a beam. Ideally, an atom laser would consist of a trapped component (the Bose-Einstein condensate) surrounded by a thermal cloud, an outcoupling mechanism continuously transferring atoms from the BEC to the output component (laser beam), and a pump mechanism enhancing the thermal cloud and thus ensuring that the condensate can be continuously replenished.

Atom lasers with no pumping have already been demonstrated experimentally [3, 4, 5]. Atom laser beams have been photographed and manipulated, and a small number of experiments have been performed showing the first order coherence of the beam [6, 7]. To quote S. Rolston and recent Nobel laureate W. Phillips: "Although atom lasers show an analogy with photon lasers, they have yet to progress far beyond the demonstration stage" [8]. The similarities do not go far enough; the currently demonstrated systems are equivalent to an optical laser in which the power has been turned off, the output beam quickly draining the source. Many of the highly valued properties of an optical laser are achieved only through continuous operation [9]. We expect that the development of a continuously pumped atom laser will open the way to an almost entirely unexplored branch of physics. The optical laser gave researchers access to the quantum properties of light, forming the core of a new science - Quantum Optics. The atom laser will become one of the enabling technologies for the development of Quantum Atom Optics.

Despite the infancy of the field, a number of uses for the atom laser are already clear. From the perspective of pure research into ultra-cold atoms, an unpumped (quasi) continuous atom laser can be used as a sensitive probe of condensate properties such as coherence [10] and collective modes [11]. The atom laser is an obvious (although as yet unused) choice for experiments on the interaction of Bose-condensed atoms with surfaces, such as those undertaken recently on condensate fragmentation near a microchip surface [12, 13]. Applications of the atom laser as a technology are more speculative, primarily because of the low flux associated with the current generation of quasi-continuous atom lasers. The development of a neutral atom beam scanner [14] and the demonstration of atom laser reflection and focusing [15] light the way for future experiments. Using an atom laser as the primary component of a de Broglie wave microscope [16] or in a separated path interferometer [17] appear experimentally feasible.

The atom laser schemes currently conceived are possible only through the creation of a Bose-Einstein condensate (BEC). There follows a short, general review of the theoretical and experimental achievements in the field of ultra-cold atomic physics, that have led to the belief that it may be possible to create the atomic equivalent of an optical laser.

1.2 Bose-Einstein statistics

The theory of BEC, the effect on which atom lasers are based, is attributed to A. Einstein [18]. It was inspired by the work of S. N. Bose on photon statistics and the Planck radiation distribution law. Einstein's studies (1925) were centred around the statistical mechanics of an ideal monoatomic gas. He justified the use of Bose's *photon* statistics in describing the distribution function of an *atomic* gas by citing de Broglie's thesis (1924) on the existence of matter waves. Einstein maintained that if bosonic particles behave like waves, then they should obey the same statistics as photons. This work led him to formulate the Bose-Einstein distribution function for a system of N non-interacting, indistinguishable particles, where the mean number of particles in the ith energy state is given by

$$n_i = \frac{1}{e^{(\epsilon_i - \mu)/k_B T} - 1} \tag{1.1}$$

where ϵ_i is the particle energy in the ith state, k_B is the Boltzmann constant. The chemical potential, μ, and the temperature, T, reflect the constraints on the total number of particles in the system, N, and the total energy, E [19, 20]. Below a certain temperature, the lowest energy state of the system becomes macroscopically occupied. This phenomenon corresponds to the onset of Bose-Einstein condensation (Fig. 1.1). For a uniform Bose gas of noninteracting particles, the transition

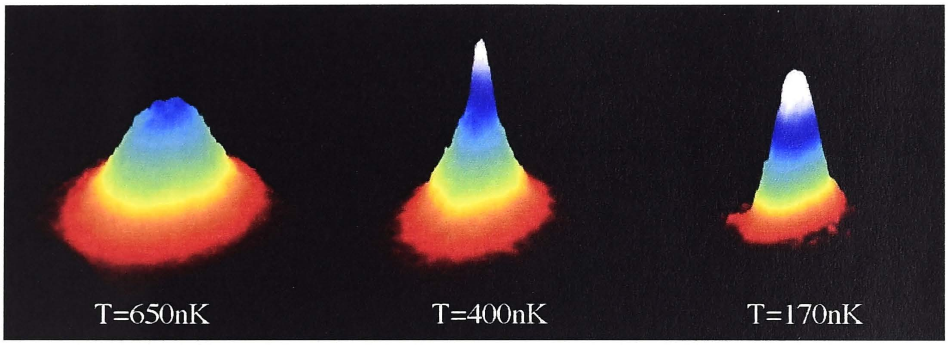

Figure 1.1: Demonstration of Bose-Einstein condensation in a dilute alkali gas of ^{87}Rb atoms, generated in the updated BEC machine described in this thesis. Shown are the raw data from consecutive runs of the experiment displaying the column density distribution from expanded cloud absorption imaging. The left image shows a thermal cloud of atoms just prior to condensation. The central image displays a characteristic ‘spike’ in the density distribution indicating the onset of BEC. The right image is an anisotropic distribution (reflecting the magnetic trap anisotropy) indicating an almost pure BEC. Each image is $\sim 0.4mm \times 0.4mm$. From left to right the total number of atoms are 7×10^5, 3.2×10^5, 1.3×10^5.

temperature at which this effect begins to occur is given by

$$T_c = \frac{2\pi\hbar^2}{k_B m}\left[\frac{n}{\zeta(3/2)}\right]^{2/3} \tag{1.2}$$

where m is the mass of a particle, ζ is the Riemann zeta function and the density, n, is given by the total number of particles, N, divided by the total volume of the system, V. The number of particles in the lowest energy state is given by

$$N_0 = N[1 - (T/T_c)^{3/2}]. \tag{1.3}$$

1.3 BEC and the macroscopic wavefunction

The development of many-body quantum mechanics [21] meant that the Hamiltonian of a weakly interacting dilute Bose gas confined by an external potential, V_{ext}, could be written down in terms of creation and annihilation field operators for bosons [22] in second quantisation formalism. In general, the field operators can be written as a sum of single-particle wavefunctions and their respective annihilation operators, for example,

$$\hat{\Psi}(\mathbf{r},t) = \sum_{\alpha} \Psi_\alpha(\mathbf{r},t)\hat{a_\alpha} \tag{1.4}$$

where the summation is carried out over all single-particle states, α and $\hat{a_\alpha}$ lowers the atom number in mode Ψ_α by 1. Because BEC occurs when the number of particles in a single ground state becomes very large compared to the occupation of other states, the condensate contribution to the field operator can effectively be separated out as follows:

$$\hat{\Psi}(\mathbf{r},t) = \Phi(\mathbf{r},t) + \hat{c}(\mathbf{r},t), \tag{1.5}$$

where $\Phi(\mathbf{r},t) \equiv \langle \hat{\Psi}(\mathbf{r},t) \rangle$ and $\hat{c}(\mathbf{r},t)$ is the annihilation operator for uncondensed particles. The function $\Phi(\mathbf{r},t)$ is a complex scalar field constituting an order parameter for the condensate, but is more typically called the macroscopic wavefunction of the condensate. In Landau's original work, the order parameter was a variable used to characterise the symmetry breaking that occurs in second order phase transitions [23].

The atoms in a BEC are essentially all in the same quantum mechanical state and can be thought of as forming a new state of matter, a quantum gas that behaves as a macroscopic system of a few million atoms, all evolving in a coherent way. The condensate forms a single quantum mechanical entity; to describe it mathematically, it is not necessary to keep track of the individual wavefunctions of the atoms forming the condensate. Rather, it is sufficient in many situations to describe the whole condensate in terms of one wavefunction, $\Phi(\mathbf{r},t)$. If the depletion of the condensate is slow then the fluctuation term $\hat{\Psi}'_\alpha(\mathbf{r},t)$ in Eq.(1.5) can be neglected. Then one can derive the Gross-Pitaevskii equation for the spatio-temporal evolution of the condensate wavefunction.

1.4 BEC and ultra-cold atoms

Apart from their direct contribution to the understanding of ideal gas behaviour, Bose-Einstein statistics, and BEC, have been used as a theoretical tool for the description of superfluid systems and the theory also has close links to the Bardeen, Cooper, and Schrieffer (BCS) theory of superconductivity [24]. By increasing the attractive two particle interaction between Cooper-paired electrons it is possible to go continuously from weak-coupling BCS superconductivity to the limit of tightly bound electron pairs which undergo Bose-Einstein condensation (BEC) [25, 26]. One of the most interesting results of these applications, at least from the perspective of the late 90s, stemmed from the study of the bosonic liquid, ^4He. Below a certain critical temperature ^4He displays a superfluid (flow without friction) behaviour, appearing to consist of two distinct components: a normal fluid and a superfluid. Over roughly thirty years (1937-1960s), a theory of superfluid ^4He was developed around the ideas of two-fluid hydrodynamics and BEC [27], and, as a result, much work was done on the 'unrealistic' system of a weakly interacting dilute Bose gas. This is precisely the system in which BEC is now most widely achieved experimentally [28].

1.5 Experimental History of BEC

The classic system of cold atoms is liquid ^4He, and the theory of BEC has had a mottled history with respect to this system [27]. The application of the theory to ^4He was marginalised for a time, but remained in the minds of some physicists. That a real system of trapped cold atoms in gas form could Bose condense was suggested as early as 1959 by Hecht [29], but it was not until the late 70s that experimental groups [30] began taking up the challenge. These early experiments were done in a dilution refrigerator using a stabilised gas of spin polarised hydrogen. Fundamental problems relating to recombination of the atomic hydrogen were encountered. It was realised that magnetic atom traps would overcome this difficulty by thermally separating the atoms from physical contact with the cooling apparatus [31]. From this configuration emerged the idea of evaporative cooling of atoms toward the BEC transition [32]. A theory of laser cooling of atoms [33, 34] had also been developing, together with subsequent experiments on trapped MgII ions [35]. By 1985, Steve Chu had experimentally studied the 'optical molasses' of laser cooled gaseous atoms made famous by the 1997 Nobel Prize in physics [36]. A retrospective look at the development of laser cooling is presented by the three co-winners of the prize in consecutive articles of the *Reviews of Modern Physics* (1998) [37]. By combining the ideas of laser cooling and magnetic trapping, the magneto-optical trap (MOT) was created (see Fig.1.2) [38].

This was a major step towards the creation of a BEC of gaseous atoms. BEC was actually achieved in 1995 using a combination of the MOT and a magnetic trap where atoms could be evaporatively cooled [1]. In 2001, the Nobel Prize was awarded to Eric Cornell, Carl Weimann and Wolfgang Ketterle for this early work [39]. There are now about 40 groups around the world working with BEC's in atoms as diverse as metastable He and ytterbium. Much of the experimental equipment used is now so refined that components such as the MOT are routinely built by talented undergraduate groups [40]. The theory of BEC has shown itself to be extraordinarily rich.

1.6 The definition of an atom laser

Because optical and atom lasers appear on the surface to be quite different, it is necessary to thoroughly define the atom laser. This definition will be approached in several ways. First, examination of the analogy between components of the atom and optical lasers reveals that it is difficult to arrive at any more than a superficial similarity between the two systems. Next, following Wiseman and Collett [41, 42], it is shown that the properties of the output beam are where the real similarities between optical and atom lasers lie. Finally, we review a number of measurements on Bose-condensed atoms and atom laser beams that confirm the presence of true laser like behaviour.

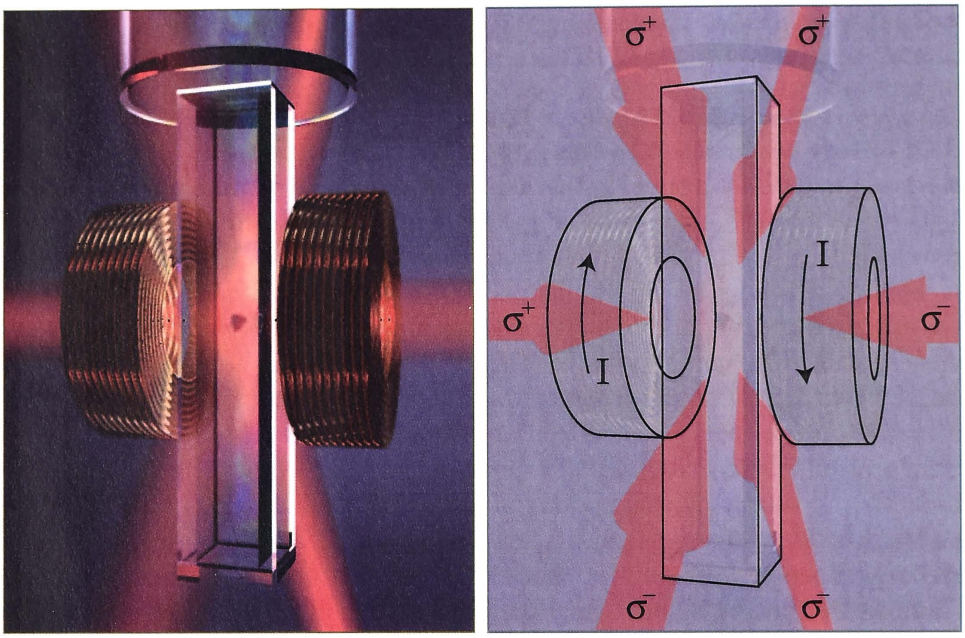

Figure 1.2: Left panel shows a rendering of a magneto-optical trap. The trapped atoms can be seen levitating at the center of six intersecting laser beams which cool the atoms below 1 mK. The atoms are contained within an ultra-high vacuum glass cell (3 cm by 3cm square in this image) to isolate them from thermal contact with any hot objects. Electromagnetic coils on either side of the cell create a trap for the atoms. Image created by the author using Pov-Ray. Right panel shows a labeled schematic of the MOT, including laser polarisation and orientation of current in the electromagnets.

1.6.1 The optical laser

The practical properties that set an optical laser apart from thermally produced light are its monochromaticity, unusual coherence, directionality and brightness or flux [43]. Monochromaticity refers to the very narrow spectral linewidth of laser light while coherence refers to first and higher order spatial and temporal correlation functions of the laser field. Directionality means that we are able to separate out the direction of wave propagation from the directions of diffraction, and brightness means that the power emitted in a single mode per unit area per solid angle from the laser is orders of magnitude greater than that for bright conventional sources. A laser is typically described in terms of its macroscopic mechanical components (see Fig. 1.3). These comprise a resonant cavity (ideally at a single frequency), an amplifier or gain medium, and a source of energy known as the pump. Traditionally, the gain medium is composed of an atomic or molecular media with a level structure that facilitates population inversion (on average there are more atoms in the excited state of the laser transition than the ground state of the laser transition) when pumped. This inverted population can then be used to coherently amplify a very narrow band of light resonant with the inverted transition, via stimulated emission. The cavity mirrors reflect the amplified light back into the gain medium producing a feedback system which leads to laser oscillation. Providing that the cavity has low losses, these coherent optical oscillations can build up to extremely large amplitudes. A partially silvered mirror allows some of this light to 'leak' from the cavity producing a beam with the previously mentioned qualities. The properties of monochromaticity, directionality and brightness can be seen intuitively to arise from this 'mechanical' description, however the coherence of the optical laser stems from subtleties of the quantum processes within the system that are not immediately apparent.

The above properties can be condensed into a one line definition for the (continuous) laser as follows:

- A laser system produces a beam with a very large number of bosons in a single mode, which is very well approximated by a classical wave of fixed intensity and phase [42, 44].

Optical lasers conform so closely to this definition that much of their study is related to the *noise* in both amplitude and phase around the wave. The remainder of this section outlines why this is so.

1.6.2 Properties of a generic laser beam

Arguably, the most important of the processes within an optical laser is the gain saturation [9] that leads to steady-state operation. Many of the useful properties of a laser output, in particular its low-intensity fluctuations and slowly varying phase (which are both related to coherence), rely upon this mechanism [41]. It is a standard result [20] that the gain coefficient of a typical laser medium is a function of the population difference between the excited and ground states of a laser medium, $N = N_2 - N_1$. This, in turn, is a function of the photon flux density, through the transition rate between the two levels. Thus the gain coefficient for the photon field is actually dependent upon the photon density to be amplified. This is a *nonlinear* process and one finds that the gain coefficient is a decreasing function of photon flux

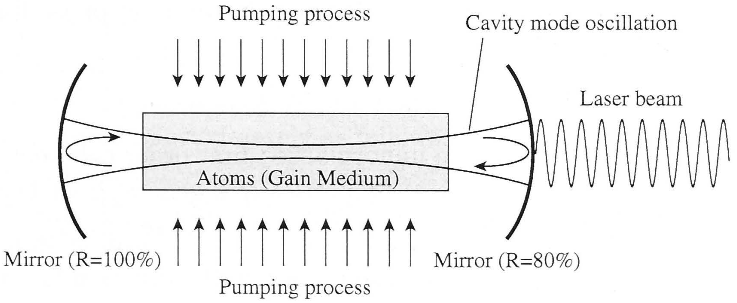

Figure 1.3: Schematic of a typical optical laser

density. This effect is termed gain saturation. When the saturated gain coefficient becomes equal to the loss coefficient (ie the sum of cavity and mirror losses) for the system, the laser reaches a steady-state regime. The intensity fluctuations of the laser field are damped by this dynamical negative feedback and the laser becomes approximately second order coherent. In terms of Glauber's second order normalized coherence functions [45] this can be expressed as

$$|g^2(\tau) - 1| \ll 1. \tag{1.6}$$

where $g^2(\tau) = \langle : I(t+\tau)I(t) : \rangle / \langle I \rangle^2$, $\langle :: \rangle$ denotes normal ordering, and I is the laser intensity (or atom laser density). For second order coherent light the quantum (or shot) noise is the only contribution to the intensity noise spectrum.

Given that gain saturation leads to laser oscillation of essentially constant intensity, fluctuations in the laser field's complex amplitude are dominated by phase noise [9, 42]. Phase noise in the laser is typically attributed to spontaneous emission [44]. Recently, Wiseman pointed out that this is not the case [46]. In fact, the phase diffusion has equal contributions from both the gain and loss. Just as stimulated emission in a linear amplifier causes intensity noise, *stimulated emission* gain in the laser causes phase noise. Taking a two time correlation of the field itself will characterise these phase fluctuations and this is generally expressed as the normalised first order correlation function $g^1(\tau) = \langle a^\dagger(t+\tau)a(t) \rangle / \langle a^\dagger a \rangle^2$ where a is the complex amplitude of the field. For $\tau = 0$ this is simply a measurement of the mean intensity (density for atoms). Ideally the phase, and hence $g^1(\tau)$, will remain constant for a long period. This *coherence time* of the laser can be characterised by

$$T = \int_0^\infty |g^1(\tau)| d\tau. \tag{1.7}$$

To make a precise measurement of the phase of the field, and hence $g^1(\tau)$, requires an interference experiment with a large number bosons in the field (the uncertainty in the measurement scales roughly with the inverse of the occupation number). This condition coupled with the requirement that the measurement time be shorter than the coherence time of the laser leads to the conclusion that spectral width of the laser beam should be much smaller than the output flux (defined in this comparison as number of bosons per unit time) [47]. Written in terms of phase fluctuations of the field this condition is:

$$1 \ll \int |G^1(\tau)| d\tau, \tag{1.8}$$

where $G^1(\tau) = \langle a^\dagger(t+\tau)a(t) \rangle$ is the unnormalised first order coherence function.

In summary, there are a number of properties of a generic laser beam which do not require a unique form of the actual laser system. These are [42]

- the beam should be highly directional
- the beam should be monochromatic ($\delta\omega \ll \overline{\omega}$ where $\overline{\omega}$ is the average frequency). For atoms these quantities refer to the frequency associated with the atomic kinetic energy.

- the beam intensity fluctuations are small ($|g^2(\tau) - 1| \ll 1$)
- the beam phase fluctuations are small ($1 \ll \int |G^1(\tau)| d\tau$)

The final condition can be made stronger by requiring that the laser linewidth be less than the bare cavity linewidth, an effect which is known as *linewidth narrowing.* The theoretical discovery of this effect is usually attributed to Schawlow and Townes [48], but a related result was actually derived three years earlier by Gordon *et. al.* [49]. As discussed by Siegman [9], the results of Schawlow and Townes predict a narrowing of the spectral linewidth (equivalent to a slowing of the rate of phase diffusion) of the laser mode as the coherent power of the laser is increased. The reader should note that in practice the limiting linewidth due to these *quantum noise fluctuations* is broadened significantly by effects such as mechanical jitter, thermal drift and other 'technical noise' [9]. Thus we do not use this stronger condition in defining a laser.

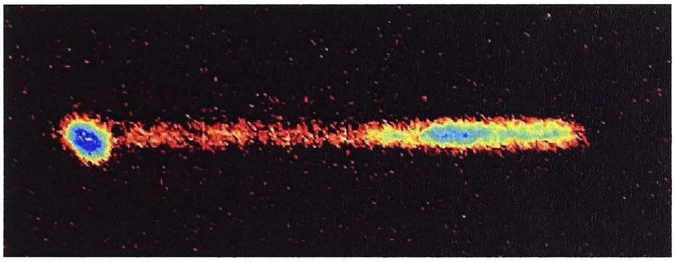

Figure 1.4: The atom laser described in Chapter 4 showing an atomic beam derived from a Bose-Einstein condensate of about 10^4 atoms over a 12ms period of continuous out-coupling. The magnetic trap has its weakly confining axis perpendicular to the output beam and gravity. The spatial extent of the beam is 0.7mm, and gravity is to the right.

1.6.3 An ultra-cold laser

In examining whether any of the properties of an optical laser could be emulated by an ensemble of ultra-cold atoms (see figure 1.4), we will show the physical analogies between an optical laser system and a trapped Bose-Einstein condensate. An optical laser works approximately as follows. Atoms are pumped by an external energy source into an excited state from where the atoms quickly decay into the upper laser level of the atom. The atom decays from this level by spontaneous or stimulated emission into the lower laser level which is quickly depleted due to a very short lifetime. This ensures that the atom cannot absorb photons from the optical field as it begins to build up in the laser cavity. Laser threshold is reached when the rate of stimulated emission from the upper laser level exceeds spontaneous emission and other loss mechanisms (like outcoupling). Stimulated emission is enhanced by the number of photons in the laser mode as compared to spontaneous emission. The feedback due to the cavity initiates laser oscillation and the number of photons in the mode dramatically increases.

The formation of a Bose-Einstein condensate is a non-equilibirum process determined by complicated many-body dynamics [50]. In particular, there is a significant body of evidence indicating that 'quasi-condensates' form prior to a true phase coherent BEC [51, 52]. Experimental and theoretical findings indicate that after the initial condensate nucleation, bosonic gain plays a significant part in the formation of a large phase coherent condensate [53]. In keeping with the description of the optical laser, the environment in which BEC occurs can be similarly described. Magnetically confined neutral atoms are cooled through a process of runaway evaporative cooling, where the most energetic atoms are expelled from the magnetic trap and the remaining atoms continuously rethermalise at a lower temperature, a process that never strays far from thermal equilibrium. As the atoms are cooled, their dimensionless phase space density $n(0)\Lambda^3$ approaches 1, and the average distance between the particles becomes comparable to their thermal de Broglie wavelength, $\Lambda = \sqrt{\frac{2\pi\hbar^2}{Mk_BT}}$. Here, $n(0)$ is the peak density. At a critical temperature determined primarily by the number of atoms in the system, a phase transition occurs and the atoms condense into the ground state of the trap. The final number of atoms in the trap is determined by the ratio of the actual temperature to the transition temperature.

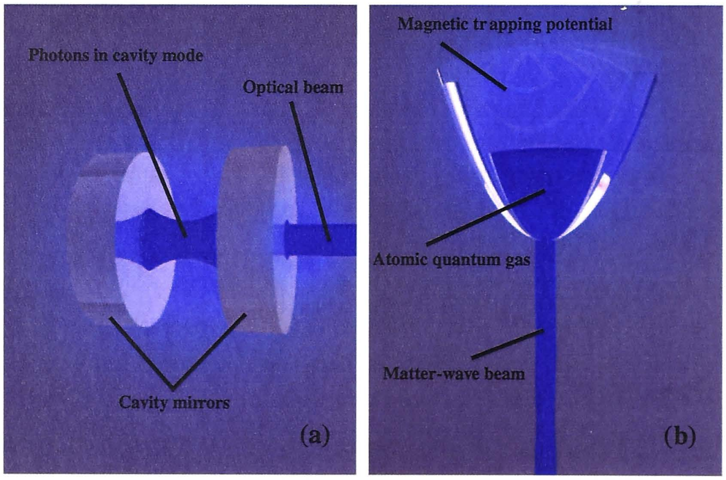

Figure 1.5: The atom laser consists of the same elements as the optical laser; a laser mode (the condensate) within a cavity (magnetic trap), a pumping mechanism (thermal cloud), which is not shown in the diagram, and an output beam.

Let us now consider figure 1.5 which shows a schematic comparison between the two systems. One can equate the macroscopic occupation of the cavity mode by photons with the macroscopic occupation of the ground state of a magnetic trap by bosonic atoms. Atoms can be coherently coupled from the trap by a number of means and this is equivalent to the traditional partially silvered mirror of an optical laser - a directional beam of bosons is produced in both cases. This comparison is the simplistic basis of the atom laser analogy, however there are far deeper similarities between the two systems: The Glauber coherence functions of first, $g^1(0)$, and second order, $g^2(0)$, of a condensate have been measured. Both correlation functions are required to have values of approximately 1 for the BEC to be considered laser like. The condensate has been demonstrated to have a first order coherence of close to one through interference experiments [53] and this has also been demonstrated for atom laser beams [10]. Preliminary work from the Boulder and MIT groups indicate the suppression of local density fluctuations through measurements of the mean field (or interaction energy) of the condensates [54, 55]. The most recent results are also consistent with $g^2(0) = 1$ [56]. However, to the best of our knowlege second order coherence has not been measured in an atom laser beam. These measurements indicate strongly that the *unpumped* atom laser actually goes a long way to fulfilling the requirements set out in the previous section for laser-like behavior. **The atom laser does not require continuous pumping or gain saturation effects to aquire its multiple order laser-like coherences.** These properties arise from the formation of the condensate and spontaneous symmetry breaking that leads to the condensate phase.

Despite these striking similarities, in order to achieve the utility of an optical laser the atom laser must be continuously pumped. In particular, this should boost the output flux and significantly reduce the operational linewidth (which is determined by the atomic reserviour drain time).

Although the atom laser was first demonstrated by the MIT group, at the present time the experimental investigation of atom lasers has been dominated by the contributions of T. Hänsch, I. Bloch, T. Esslinger and M. Köhl at the Max-Planck-Institut für Quantenoptik, in Germany. Experimental literature in the field is extremely limited and highlights in the literature, which actually comprise about 70% of the total experimental research published, are:

- Output Coupler for Bose-Einstein Condensed Atoms, M.-O. Mewes, M. R. Andrews, D. M. Kurn, D. S. Durfee, C. G. Townsend, and W. Ketterle, *Phys. Rev. Lett.*, **78** 582-585 (1997).
- Atom Laser with a cw Output Coupler, I. Bloch, T. W. Hänsch, and T. Esslinger, *Phys. Rev. Lett.*, **82** 3008-3011 (1999).
- A Well-Collimated Quasi-Continuous Atom Laser, E. W. Hagley, L. Deng, M. Kozuma, J. Wen, K. Helmerson, S. L. Rolston, and W. D. Phillips, *Science*, **283** 1706-1709 (1999).
- Measurement of the spatial coherence of a trapped Bose gas at the phase transition, I. Bloch, T.W. Hänsch, and T. Esslinger, *Nature*, **403** 166-170 (2000).
- Measuring the Temporal Coherence of an Atom Laser Beam, M. Köhl, T. W. Hänsch, and T. Esslinger, *Phys. Rev. Lett.*, **87** 160404 (2001).

- Optics with an Atom Laser Beam, I. Bloch, M. Köhl, M. Greiner, T. W. Hänsch, and T. Esslinger, *Phys. Rev. Lett.*, **87** 030401 (2001).
- Atom Laser Divergence, Y. Le Coq, J. H. Thywissen, S. A. Rangwala, F. Gerbier, S. Richard, G. Delannoy, P. Bouyer, and A. Aspect, *Phys. Rev. Lett.*, **87** 170403 (2001).
- Continuous detection of an atom laser beam, M. Köhl, T. W. Hänsch, and T. Esslinger, *Phys. Rev. A*, **65** 021606 (2002).
- Giovanni Cennini, Gunnar Ritt, Carsten Geckeler, and Martin Weitz All-Optical Realization of an Atom Laser, *Phys. Rev. Lett.*, **91** 240408 (2003).

1.6.4 The theory of atom lasers

In this section, we briefly discuss the ways in which atom lasers have been treated theoretically. In analogy with optical laser theory, the theoretical description of atom lasers can be broadly divided into three approaches: rate equation models, semiclassical (mean-field) models, and quantum models. Optical laser theory tends to increase in complexity when one moves from the level of rate equations to quantum formalism. This also applies to atom lasers, and there are many factors such as the interactions between atoms, the fact that atoms cannot be created or destroyed, and the quadratic dispersion relation of atoms, that make the dynamics of atom laser systems far less easy to tackle in more complex formalisms. At present, simpler models are able to take into account more physical contributions to the dynamics.

Using rate equation methods, theorists describe how the populations of atoms (in an atomic cavity, or atom trap, the output field and perhaps a pumping reservoir) evolve over time [57, 58, 59]. Rate equation models can also predict whether the atom laser system has a threshold or a steady state. They are well suited to describe the coarse properties of the system.

Ideally, the full quantum theory of an atom laser system, beginning with a complete Hamiltonian for the field operators of the system, would allow one to describe the quantum statistics of the atom laser completely [60, 61]. Many obstacles stand in the way of this 'complete' theory, mainly due to the mathematical and numerical complexity of the problem.

The mean field approach uses the Gross-Pitaevskii (GP) formalism discussed earlier to describe the time and space evolution of the macroscopic wavefunction of the condensate and output fields. In the framework of this approach, it is straightforward to include effects, such as interactions, that are hard to tackle with quantum statistics. However, because the GP formalism can only describe macroscopic dynamics of the atoms, we cannot extract their statistical behaviour.

A promising new approach is to use a stochastic GP equation approach based on a quasi-probability distribution. This method would incorporate stochastic terms into the 'user friendly' GP equations [62]. The quantum statistics of the system could be extracted by analysing the behaviour of a large ensemble of stochastic GP equations. In the semi-classical limit, this stochastic approach is formally equivalent to the full quantum theory [44].

1.6.5 The continuously pumped atom laser

At the time of writing, the longest an atom laser has been run continuously is about 300 ms [7], albeit at very low flux. More typical operating times are in the 10's of milliseconds. In all cases, current atom lasers are limited by typical condensate sizes of around 10^6 atoms. The atom laser beam quickly drains the condensate. Despite this, atom laser brightness [44] outperforms traditional atomic sources such as Zeeman-slowers and laser cooled atoms by at least six orders of magnitude. With Fourier limited outcoupling a further four orders of magnitude could be gained to produce an atomic source of brightness 10^{28} atoms s^2m^{-5}. The closest advanced high flux source is a Cs atomic fountain created from 3D degenerate Raman sideband cooling in an optical lattice that produced a flux of 4×10^{22} atoms s^2m^{-5} [63]. In order to utilise the atom laser as a practical research tool, a method must be found to replenish the condensate atoms without disturbing the production of an atom laser beam. Significant experimental progress has been made toward this goal. The recent work of Chikkatur et. al. demonstrated a comprehensive technique for continuously making, transporting and storing condensates [64]. The group at Laboratoire Kastler Brossel in paris have made significant progress towards implementing evaporative cooling of a continuous atomic beam in a magnetic waveguide [65, 66, 67]. A continuously pumped atom laser may be able to operate at far higher fluxes than are currently experimentally feasible and will certainly open up the possibility of long time scale measurements such as continuous interferometric detection.

1.7 This thesis

The research presented in this thesis describes both theoretical and experimental investigations of ultra-cold atoms from an atom laser perspective. In Chapter 2, we outline the background theory required to understand the contents of later chapters, and although much of the information can be found elsewhere, it is presented here for completeness. Chapter 3 presents a detailed description of the construction and operation of the 'atom laser' upgrade of our double MOT machine for producing Bose-Einstein condensates. This second generation BEC machine replaced or significantly improved all facets of the machine, except vacuum setup, computer control and the base laser system. Specifically addressed are the construction and implementation of an Ioffe-Pritchard magnetic trap and associated switching and a completely new optics system (collection and science MOTs, pumping and imaging). The final part of this chapter presents evidence for BEC in the new system, including a detailed discussion related to extracting quantitative data from images of Bose condensed atoms. Chapter 4 describes the production of an atom laser. The implementation of both continuous and pulsed atom lasers using radio-frequency output coupling is presented. This chapter investigates in detail the multi-component flux limiting dynamics of a pulsed atom laser and presents the first detailed comparison between an atom laser experiment and a full three-dimensional GP simulation of the system (performed by Dr. Craig Savage). Chapter 5 relates to the pumping of an atom laser. We demonstrate with an original theoretical model that three body recombination acts to stabilise the pumped atom laser in much the same way as gain saturation stabilises the output of an optical laser. Chapter 6 discusses the design and partial construction of our next generation atom laser machine, and includes a detailed procedure for optimising the efficiency (power generated versus geometric trapping frequency) of a QUIC magnetic trap for atom laser studies. Two appendices follow the final chapter. Appendix 1 presents a new modulation free laser locking technique (a system central to producing a BEC). Appendix 2 details the numerical methods used in this thesis.

CHAPTER 2

Experimental and theoretical background

This chapter briefly reviews important theoretical and experimental results in the field of ultra-cold neutral atomic gases that form the underpinnings of the work described in later chapters. BEC with dilute alkali gases has so far been achieved only via evaporative cooling. Unless a completely new path to condensation is found, a machine designed to make BEC has only one core function: to create a long lasting, high atomic phase-space density. This core function is achieved by a two step process: laser cooling followed by evaporation in a storage potential. Below we describe the physics of the main components of a BEC machine. Unless otherwise specified, all quantities refer to the ^{87}Rb laser cooling transition.

2.1 Atomic properties and hyperfine structure of ^{87}Rb

> "...If one works hard enough, the probability that any given species can be evaporatively cooled to the point of BEC is actually quite high."
>
> - E.A. Cornell, J.R. Ensher, and C.E. Wieman [28].

Despite this optimistic comment, and strong evidence to support it (condensation of H [68], He[69, 70], Li[71], Na[72], K[73], Rb[74, 75], Cs[76] and Yb[77]), ^{87}Rb is the most popular choice of atom for producing Bose-Einstein condensation [112]. We attribute this to three important points. It was the first atomic species condensed and hence expertise was built up rapidly and is now widely available. Secondly, the laser cooling resonance at 780 nm (the rubidium D2-line) corresponds to exactly the wavelength used for compact disc music systems. As a consequence relatively cheap, high power diode lasers are available to cool this atom, which is an important consideration for new groups entering the field [28]. Finally, and most importantly, ^{87}Rb has just the right combination of low temperature scattering properties that it can be 'straightforwardly' evaporatively cooled to degeneracy (given a large number of cold atoms and a low background gas collision rate).

The atomic spectroscopy of ^{87}Rb is presented on the left hand side of figure 2.1, showing the D2 optical transition (saturation intensity 1.65 mW/cm^2 for $5S_{1/2}, F = 2 \rightarrow 5P_{3/2}, F' = 3$ or 4.1mW/cm^2 for random polarization), and the relevant hyperfine splitting. The $5S_{1/2}$ ground states are split by 6.835 GHz.

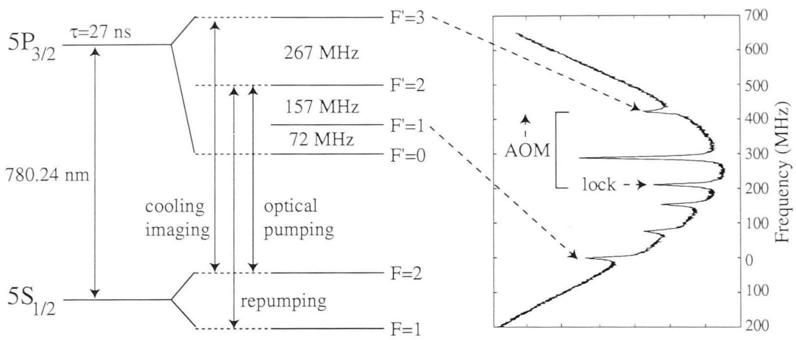

Figure 2.1: Some details of the ^{87}Rb spectroscopy relevant to the current experiment. On the right is a theoretical plot of the saturated absorption spectrum [79] calculated from the model of Appendix A. In our experiment the laser is locked to the $F = 2, F' = 1,3$ crossover and shifted onto resonance by a double passed 120 MHz acousto-optic modulator (AOM).

The right side of Figure 2.1 shows a typical saturated absorption spectrum of the $5S_{1/2}, F = 2 \rightarrow 5P_{3/2}, F'$ transitions. The cycling transition for laser cooling of ^{87}Rb is the $5S_{1/2}, F = 2 \rightarrow 5P_{3/2}, F' = 3$ which has a natural linewidth of $\gamma = 2\pi \times 5.9$ MHz. A laser able to resolve this transition must have an instantaneous ($\sim 1ms$) linewidth less than 5.9 MHz and be frequency stabilised in an absolute sense to greater than 1 part in 10^9. Despite such stringent requirements, there is a small probability ($\approx 10^{-3}$) of the cooling laser exciting the $5S_{1/2}, F = 2 \rightarrow 5P_{3/2}, F' = 2$ transition. From this hyperfine state there is significant chance (50%) of the atom decaying into the 'dark' lower hyperfine ground state. For saturation intensities, light resonant with the $5S_{1/2}, F = 2 \rightarrow 5P_{3/2}, F' = 3$ transition will optically pump an entire atomic sample into a non-resonant state and laser cooling will cease in a few milliseconds. To avoid this, an additional low power laser is applied resonant with the $5S_{1/2}, F = 1 \rightarrow 5P_{3/2}, F' = 2$ transition, pushing the atoms back into the optical cooling cycle. The fraction of laser cooled atoms in the dark state can then be controlled, ranging from 0 to 100%. A number of schemes rely on manipulating this effect either spatially [80] or temporally [81] to increase magneto-optic trap densities, a factor critical to BEC. The optical pumping light resonant with the $5S_{1/2}, F = 2 \rightarrow 5P_{3/2}, F' = 2$ transition is used to prepare an atomic sample for magnetic trapping and is discussed in detail in Chapter 3.

2.2 Pushing atoms around

The production of a Bose-Einstein condensate and an atom laser requires that the external (kinetic temperature) and internal (electronic) degrees of freedom of an atom must be manipulated with high precision. In order to manipulate atoms, we must apply a force to them. Three general tools are used to do this: the dissipative or radiation pressure force, the dipole force and the force on an atom due to interaction of its atomic spin with an inhomogeneous magnetic field. The radiation pressure force arises when a stationary atom absorbs photons from an optical traveling wave. Because the atom spontaneously emits photons absorbed from the laser in a random direction, it feels a net force (the acceleration can be huge - up to $10^5 g$) in the direction of the wavevector of the laser. This scattering force is dissipative and saturable. The atom also experiences a force proportional to the gradient of the spatially modulated light shift $\Delta = (\hbar\Omega^2\delta/(\delta^2 + \gamma^2/4)$, where Ω is the Rabi frequency, γ is the transition linewidth and δ is the laser detuning from the atomic resonance. This force is called the dipole force. It is conservative and does not saturate. The scattering and dipole forces can be used in combination or separately to produce a variety of optical cooling and/or trapping schemes. Although we will not discuss the dipole force any further in this thesis, it plays an integral part of the new atom optics of Feshbach resonances in optical dipole traps [82]. The magnetic force is well known through the experiment of Stern and Gerlach on the separation of atomic spin [83, 84]. It takes the form $\mathbf{F} = -\nabla(\mu \cdot \mathbf{B})$ where μ is the atomic magnetic moment and $\mathbf{B}$ is the magnetic field. Each force has its own unique benefits and, as will be discussed in the following sections, when judiciously combined to make use of their strengths, they can increase the phase space density of a small number of atoms (10^6) by at least 12 orders of magnitude.

2.3 Optical molasses & the magneto-optical trap

The magneto-optical trap (MOT) [38] cools atoms from a diffuse room temperature vapor to a small cloud of atoms at a few hundred micro-kelvin in milli-seconds. As mentioned in the introduction, this dramatically efficient cooling system forms a key step in the production of a Bose-Einstein condensate. When the MOT is followed by an optical molasses cooling stage [37], the temperature of an atomic sample can be lowered another order of magnitude to approximately 50μK. Optical molasses cooling relies on a velocity dependent form of the scattering force as described below.

2.3.1 Doppler and sub-Doppler cooling

For a two level atom moving in a single optical travelling wave (one beam), the optical Bloch equations [85] can be used to find that the radiation pressure force on the atom has the form $F = F_0 - \beta\nu$ where β is a cooling coefficient dependent on the laser detuning from the atomic transition, the laser intensity and the laser wave-vector, and ν is the atomic velocity. F_0 is the force on an atom at rest, approximately $\hbar k$ times the scattering rate, where k is the wavevector of the optical field. For red detuned light the second term leads to a force that compresses the atomic velocity distribution on a timescale of approximately $100\mu s$ but does nothing to lower the average velocity. If an optical standing wave is used, the rest force, F_0, on the atoms averages to zero. Then a true velocity dependent damping force arises. Not only is the velocity distribution narrowed, but the average atomic velocity is lowered towards zero. This effect is known as Doppler cooling and can be intuitively understood by studying a two-level atom moving in a red detuned traveling wave as in Fig. 2.2. An atom that is moving towards one of the cooling beams will be Doppler shifted *towards* the atomic resonance, while an atom traveling in the opposite direction will be shifted *away* from resonance. Because an atom is more likely to absorb photons on resonance, it preferentially scatters photons opposing its motion. In this way, the motion of an atom in a one dimensional optical standing wave is quickly damped. This cooling effect is limited by the random momentum kick the atom receives from spontaneous emission following the absorption of a directional cooling photon. By equating the diffusive heating of spontaneous emission with this velocity selective cooling mechanism, one arrives at the Doppler cooling limit to the temperature: $T = \hbar\gamma/(2k_B)$ where γ is the linewidth of the atomic transition and $\mathrm{k_B}$ is Boltzmann's constant. For rubidium, this temperature corresponds to about $140\mu K$. By using three pairs of orthogonal laser beams to produce optical standing waves in three orthogonal directions, this system can be extended to create a full three dimensional cooling scheme. The atoms are cooled so quickly in the laser fields that they move according to simple Brownian motion due to spontaneous emission. Because of this, the atoms diffuse out of the trap on the time scale of 10 to 10^2 milli-seconds; the atoms are effectively confined over these short times, and this has become known as optical molasses [37] (figure 2.3).

Temperatures significantly lower than those predicted by Doppler cooling are possible in this type of laser configuration due to interaction between the polarisation of the molasses and the complex internal structure of the atom (rather than the two level atom used to model Doppler cooling). Temperatures of a few times the recoil limit $T = (\hbar k)^2/(Mk_B)$, where k is the wavevector of the laser beams and M is the mass of an atom (about 400 nK for Rb), are theoretically possible [37] but in practice radiative effects limit the temperature of optical molasses to a factor of about 10^2 higher than the recoil limit.

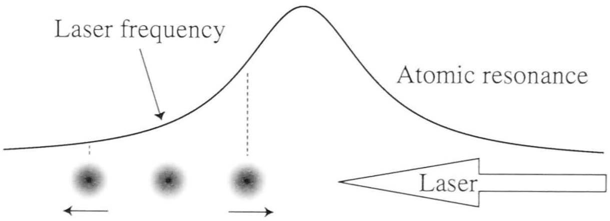

Figure 2.2: The mechanism of the Doppler cooling scheme. Atoms absorb more photons when they are traveling towards a red de-tuned laser, because they are shifted onto resonance.

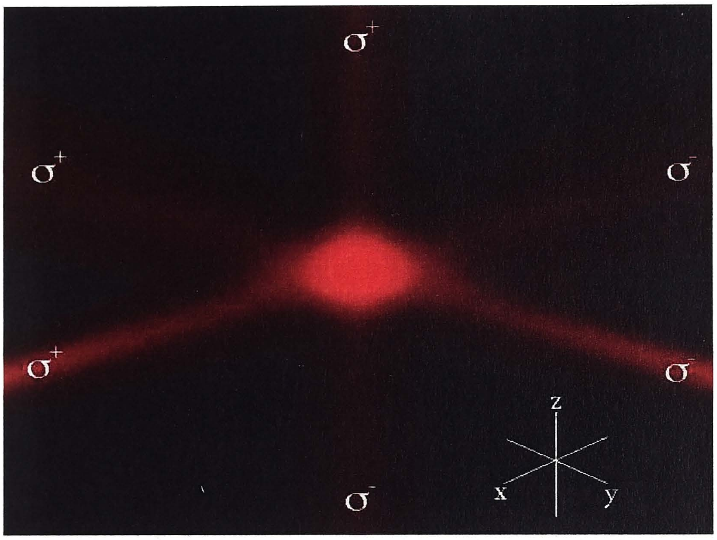

Figure 2.3: Three spatially orthogonal, counter-propagating pairs of oppositely circular polarized light form an optical molasses as used in many Bose-Einstein condensation experiments.

2.3.2 Polarisation gradients

Consider the light field generated by two red-detuned counter-propagating oppositely circular polarized lasers of the same wavelength, λ. If the amplitude of the lasers is the same then along the axis of the beams the local polarisation is always linear and varies helically with a pitch of λ. For a two level atom, characterised by a transition linewidth of γ, moving in this configuration of lasers simply results in the Doppler cooling described in the previous section. A *real* atom has multiple Zeeman states of the ground and excited levels. A velocity dependent sub-Doppler cooling mechanism arises in this configuration due to a combination of polarisation-dependent optical pumping and constant (but different) light shifts ($\Delta = (\hbar\Omega^2\delta/(\delta^2+\gamma^2/4)$ where Ω is the Rabi frequency, γ is the transition linewidth and δ is the laser detuning from the atomic resonance) on each of the atomic Zeeman states due to the presence of the optical field. This effect can be described by considering an atom with a $J = 1 \rightarrow 2$ transition (the simplest case for which this cooling scheme can work), consisting of three initially degenerate Zeeman ground states, $m_F^g = -1, 0, 1$ and five excited states $m_F^e = -2, -1, 0, 1, 2$. Because of the selection rules for π atomic transitions (absorption of linearly polarised light), a stationary atom quantised in the direction of the local polarisation will quickly be optically pumped into steady state population distribution of 0.235:0.53:0.235 for the $m_F^g = -1, 0, 1$ states respectively, according to the appropriate Clebsch-Gordon coefficients. In addition, a π transition from $m_F^g = 0$ is 1.33 times as strong as a π transition from the $m_F^g = \pm 1$ states and so the light shift is larger for the $m_F^g = 0$ state. An atom *moving* along the axis of the laser field will experience a fast change in the polarisation direction, which leads to a non-adiabatic coupling between the Zeeman ground states experiencing different light shifts. A lengthy calculation [86] reveals that in the moving frame of the atom a population difference between the $m_F^g = 1$ and $m_F^g = -1$ arises proportional to the atomic velocity divided by the $m_F^g = 0$ light shift. For red detuned lasers, the light shift is negative. As shown schematically in figure 2.4, if an atom is moving toward the σ^+ laser, it will have a greater population in the $m_F^g = +1$ states. For an atom in this state, the scattering probability for σ^+ light is a factor of six higher than that for σ^- light. A similar argument applies for atoms moving towards the σ^- light. The radiation pressures exerted by the lasers will be unbalanced and atoms will scatter more light from the counter-propagating laser, giving rise to velocity dependent cooling. The time scale for optical pumping is equal to the inverse of the linewidth of the ground state, γ_G (which is due to the mean scattering rate of photons). In the limit of low laser power (Rabi frequency $\Omega \ll \gamma$), the optical pumping time is very long compared to the lifetime of the excited state and hence $\gamma_G \ll \gamma$. Because of this clear separation of internal timescales, there are two regimes in which this 'induced orientation' cooling force acts depending on the velocity of the atom, v;

- when $kv \ll \gamma_G$ there will be significant cooling due to the mechanism described above.
- when $kv \gtrsim \gamma$ the coherences between Zeeman states will be negligible and the force on the atom roughly equals the Doppler force.

In figure 2.5, the force on the atoms over a large range of velocities is presented [86]. It is clear that this cooling mechanism is extremely versatile. It has a large capture range (similar to Doppler cooling) but can also reduce the kinetic temperature of atoms well bellow the Doppler limit. The scheme is very sensitive to an external magnetic field because it relies on the spin orientation of the Zeeman states. A field of the order of 10 mG will dramatically disrupt the low velocity cooling [37]. Finally all of the above analysis relies on the fact that an atom travels directly along the axis of the cooling beams, which is clearly not the case in reality. The polarisation experienced by an atom moving off axis is far more complex than described here and other types of cooling mechanisms (such as Sysiphus cooling [86]) occur as well. Although Doppler cooling and induced orientation cooling can dramatically reduce the temperature of an atomic system (to 10's of μK) they are still only viscously

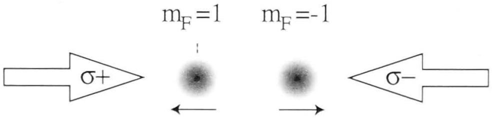

Figure 2.4: Schematic of the $\sigma^+ - \sigma^-$ polarisation cooling scheme, indicating the population imbalance for moving atoms.

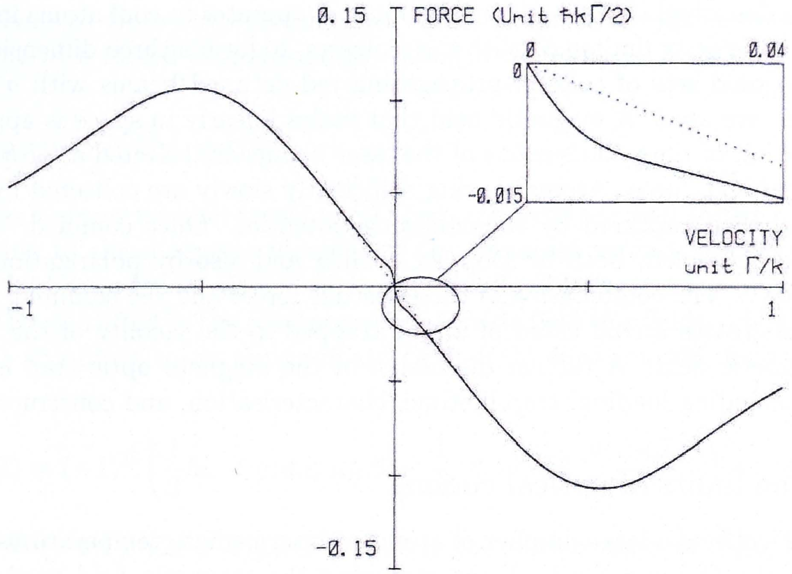

Figure 2.5: The complete cooling scheme of $\sigma^+ - \sigma^-$ polarisation showing the force on an atom as a function of its velocity. Schematic from J. Dalibard and C. Cohen-Tannoudji [86]. The inset to the figure shows the increased slope of the cooling force coinciding with sub-doppler cooling region in comparison to the standard doppler cooling slope.

confining (a feature described by the optical Earnshaw theorem [87]). In order to produce a true trap we need to introduce a spatially dependent mechanism to localise the atoms.

2.3.3 The magneto-optic trap

The interaction of the internal structure of the atoms with an external field can be used not only to create a viscous force as described in the previous section, but also a trapping potential that will localise the atoms in space (see figure 2.6). By using linear magnetic fields in addition to the laser fields of an optical molasses, a magneto-optical trap (MOT) can be created [38]. The ground and excited magnetic states will be shifted in energy by the Zeeman effect. Two red-detuned counter-propagating beams, one with σ^+ polarisation and one with σ^- polarisation illuminate the atoms. Because the σ^+ polarisation drives only $\Delta m = +1$ transitions, the magnetic field can be arranged so that when the atoms move away from the point where B=0 towards the σ^+ beam, the atom sees that beam shifted into resonance. More photons will be scattered from the σ^+ beam than the σ^- beam and the atom will be pushed back towards the point where $B = 0$. In the same arrangement of fields and lasers, atoms that move towards the σ^- beam will also be pushed back to B=0. In addition to the trapping provided by this scheme, the orientation cooling mechanism described in the previous section still operates to cool atoms in both the high and low velocity limits. As with the molasses, to form a three-dimensional trap, three orthogonal sets of counter-propagating red-detuned beams with σ^+ and σ^- polarization are used. A magnetic field that varies linearly in space is applied, and the orientation of the polarisations of the laser beams are selected appropriately to create a confining force. Atoms moving sufficiently slowly are collected by Doppler cooling and then captured by the confining potential. Once confined, the atoms continue to be cooled, both by Doppler cooling and also by polarization-gradient cooling (PGC). The combination of these viscous forces and the confining magneto-optic forces creates a cold cloud of atoms trapped in the vicinity of the minimum in the magnetic field. A further discussion of the magneto optic trap is given in chapter 3 including loading, trap lifetime, characterisation, and construction.

2.3.4 The limits of optical cooling

A MOT collects a large number of atoms at intermediate temperatures typically just below the Doppler limit. Upon removing the magnetic field used to create the trapping in a MOT, a much larger portion of the atomic cloud experiences the conditions necessary for orientational cooling. We mentioned previously that the theoretical limit to PGC is extremely low, around a couple of μK. In fact, optical techniques, such as Raman sideband cooling [63], are available that can lower the temperature of an atom cloud significantly below the *recoil limit* of 400 nK. However, achieving Bose degeneracy requires a phase space density of the order of 1, and although very low temperatures are achievable with optical cooling, the atomic density is severely limited. At such high densities and low temperatures the large number of trapped atoms becomes optically thick; it is likely that a cooling photon will be scattered multiple times. This leads to a repulsive radiative force between the atoms, which limits the density of the sample to less than 10^{11}atoms/cm^3 [81]. The presence of the laser light also introduces density-dependent light-assisted collisional losses in the MOT [135]. The combination of these effects limits the phase space density of a MOT to around 10^{-7} and a PG cooled sample to an order of magnitude less. In order to increase the density, it is clear that the resonant cooling light

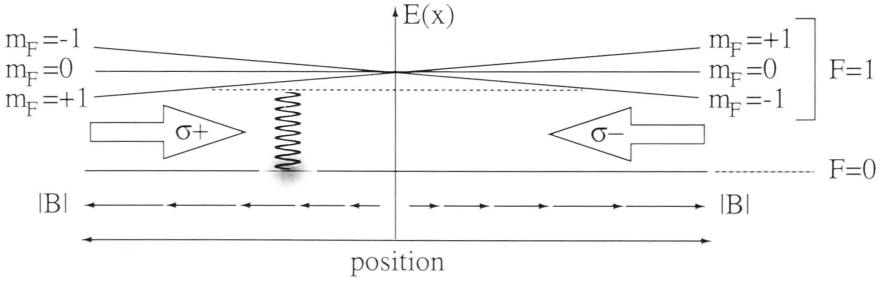

Figure 2.6: Schematic of the operating principle of a magneto-optical trap.

must be removed from the system completely. Magnetic trapping takes over the confinement with forced evaporation providing the cooling.

2.4 Magnetic trapping

The alkali atoms typically used in BEC experiments are well suited to magnetic trapping due to the magnetic moment of the unpaired valence electron. For the magnetic field magnitudes described in this thesis, the degeneracy of the Zeeman states of ^{87}Rb are lifted in the presence of a magnetic field (for fields < 80 G by about 1 MHz/G) according to an approximate Breit-Rabi equation [88] for the Zeeman energy:

$$E_{F,m_F}(B) = (-1)^F \left(\frac{1}{2}\hbar\omega + g_F m_F \mu_B B + \frac{1}{16}(4 - m_F^2)\frac{(g_S \mu_B B)^2}{\hbar\omega} \right) + const. \quad (2.1)$$

where $g_F = (-1)^F 1/(2I+2) g_S$, $I = 3/2$ is the nuclear spin of ^{87}Rb, $\omega = 2\pi \times 6.835$GHz and $g_S = 2.0$ is the electron g-factor. The first term is the hyperfine splitting between ground states. The second term is the linear Zeeman effect. The third term contributes significantly for magnetic fields above about 100 G. The magnetic traps used for the work presented in this thesis operate near zero magnetic field and hence the energy of an $|F, m_F\rangle$ state can be well approximated by the linear Zeeman effect $E = g_F m_F \mu_B |\mathbf{B}|$. As an atom moves through space, its moment will precess around the spatially varying magnitude and direction of the magnetic field, with a Larmor frequency of $\omega_L = g_F \mu_B |\mathbf{B}|/\hbar$ (for a field of 1 G $\omega_L \approx 2\pi \times 0.7$ MHz). If the field varies slowly, the precession will adiabatically follow the field, and the atom's Zeeman energy will depend only on the amplitude of the field. Thus, the atom will remain in a particular Zeeman state and will move in a potential defined by the Zeeman energy:

$$V(\mathbf{x}) = g_F m_F \mu_B |\mathbf{B}(\mathbf{x})|. \quad (2.2)$$

Wing's theorem [89] proves that Maxwell's equations do not permit a maximum in the magnitude of DC magnetic fields in free space. They do, however, allow a magnetic field minimum. Thus, to make a magnetic trap for atoms we require that the product $g_F m_F$ be positive. To be trappable in the low field limit, an atom's Zeeman energy must increase with increasing magnetic field. For the two hyperfine ground states of ^{87}Rb there are three low field seeking, magnetically trappable states : $|F = 2, m_F = 2\rangle$, $|F = 2, m_F = 1\rangle$, and $|F = 1, m_F = -1\rangle$. The state $|F = 2, m_F = 2\rangle$ is uneffected by the quadratic Zeeman effect. The $|F = 2, m_F = 0\rangle$ also feels a weakly confining potential due to the quadratic term in Eq. 2.1. If the direction of the field changes quickly compared to the Larmor frequency, the atom will make a non-adiabatic Marjorana transition [90] to its neighboring m_F states where it may be lost from the trap. The effect of such a transition is shown in Figure 2.7 where one can clearly see a number of the Zeeman states of the F=2 level produced by sweeping a zero in the trapping magnetic field through the atomic cloud. The following section quantifies the effect of these Majorana transitions for a harmonic trap in terms of the Landau-Zener coefficient for an avoided level

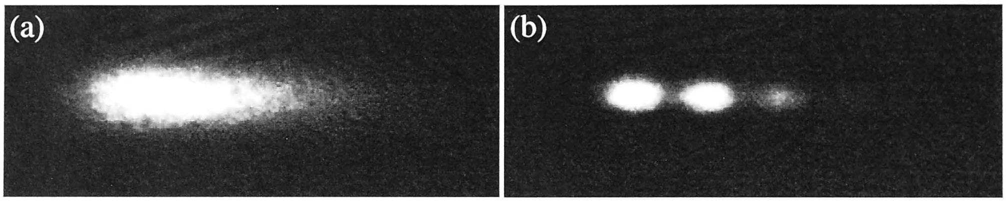

Figure 2.7: BEC spectroscopy of the Zeeman sublevels of the F=2 ground state of ^{87}Rb performed on the BEC machine described in this thesis. Shown are 5 ms expansion absorption images of a cloud of atoms through which a magnetic field zero crossing has been swept. (a) Cloud just prior to BEC and (b) well below the transition temperature. From left to right of image (b) is the $m_F = 2$, $m_F = 1$, $m_F = 0$ and a faintly visible $m_F = -1$

crossing [91]. The adiabaticity criterion can be established by requiring that the rate of change of the magnetic field direction is significantly smaller than the Larmor frequency, $|\mathbf{v_T} \cdot \nabla \hat{\mathbf{B}}| \ll \omega_L$ where $|\mathbf{v_T}| = \sqrt{\frac{8k_BT}{M\pi}}$ is the thermal velocity of the atom of mass M and temperature T and $\hat{\mathbf{B}} = \mathbf{B}/|\mathbf{B}|$ is the magnetic field unit vector. This condition can be approximated in one dimension by $v_T\frac{dB_\rho}{d\rho} \ll \frac{g_F\mu_B B_\rho^2}{\hbar}$. For a temperature of 1 mK and a magnetic field gradient of 200 G/cm, this condition is easily satisfied for field magnitudes greater than about 200 mG. For atoms at BEC temperatures less than 1 μK, this adiabaticity condition is relaxed dramatically.

The simplest way to create a trapping magnetic field geometry is to use a pair of coils with opposite but equal current. The magnitude of the magnetic field produced increases linearly from zero in all directions and hence is able to trap neutral atoms. Although this geometry was used for the first demonstration of magnetic trapping of neutral atoms [92], an extreme version of Majorana transition occurs in this configuration. The Larmor frequency goes to zero at the trap centre producing a Majorana flop, and this mechanism introduces a catastrophic loss of atoms at low temperatures [93]. To avoid this effect, different trapping geometries have been developed, all based on keeping the magnetic field minimum (or bias) in the adiabatic regime. One solution is the so called time-orbiting potential (TOP) trap which employs a time varying magnetic field to create a finite magnetic field bias. This trap was used for the first observation of Bose-Einstein condensation in rubidium atoms [74]. The MIT group solved the problem of creating a bias by adding a blue detuned focused laser to the magnetic trapping potential [72]. The dipole effect forced atoms into regions where they could adiabatically follow the magnetic field. Later, many groups moved to a DC trap known as the Ioffe-Pritchard (IP) conguration [94], in which the atoms experience a harmonic potential with a nonzero bias magnetic field at its centre.

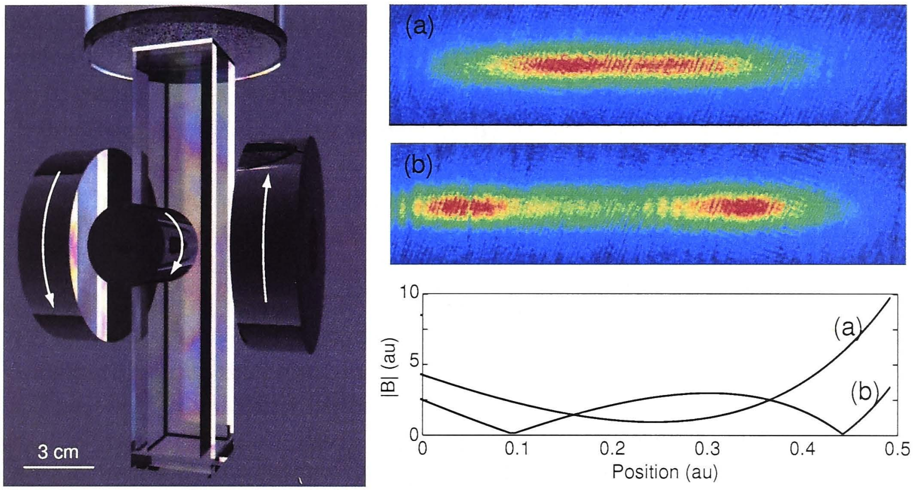

Figure 2.8: Left panel: Schematic of the QUIC magnetic trap, showing the relative position of each coil and the direction of current flow in the coils. The two large coils are the quadrupoles. Right panel: Absorption images of 10^8 ^{87}Rb atoms in the QUIC trap described in Chapter 3. In (a) the magnetic coils are adjusted to produce a harmonic IP trap, while in (b) the Ioffe coil has been moved axially outward by approximately $20\mu m$ producing two quadrupole traps. The barrier height is low enough that the $50\mu K$ atoms spill between the wells.

2.4.1 The Ioffe-Pritchard configuration trap

The IP configuration provides the strongest DC trapping potential with an inherently non-zero bias field. For an IP-type trap, the field is approximately harmonic about a non-zero field minimum (B_0), the radial (tight) trapping direction scaling with the inverse of B_0. If the temperature of the trapped atoms satisfies the relation $kT \ll |\mu| B_0$, the trapping potential around the trap minimum is well described by a harmonic function [95]:

$$V(z,\rho) = |\mu| \left(B_0 + \frac{1}{2} B''_\rho \rho^2 + \frac{1}{2} B''_z z^2 \right) \tag{2.3}$$

where z is the axial coordinate, ρ is the radial coordinate and $B''_\rho = {B'_\rho}^2 / B_0 - B''_z/2$. The $'$ denotes magnetic field derivatives with respect to the spatial coordinates. The radial and axial trapping frequencies are then given by:

$$\begin{aligned} \omega_z &= \sqrt{\frac{\mu_B g_F m_F B''_z}{M}} \\ \omega_\rho &= \sqrt{\frac{\mu_B g_F m_F B''_\rho}{M}}. \end{aligned} \tag{2.4}$$

The adiabaticity criterion can be recast in terms of the trapping coefficients using the Landau-Zener formalism [91] as:

$$\frac{g_F \mu_B B_0^2}{\hbar m_F B_\rho' |\mathbf{v_T}|} \ll 1 \tag{2.5}$$

In the work described in this thesis, we use a three coil IP trap conceived by Söding *et.al* [96] and developed into the tightly confining quadrupole Ioffe configuration (QUIC) design at Munich [97]. The configuration of the QUIC trap is shown in the left panel of Figure 2.8. In this setup an Ioffe-Pritchard trap is generated by two quadrupole coils (oriented along the y-axis) with opposite current which produce a field $\mathbf{B_Q}$ that increases linearly in all directions from a zero at the origin. The Ioffe coil (oriented along the z-axis) produces a non-linear magnetic field, $\mathbf{B_I}$, that, when summed with the linear quadrupole field, gives an approximately harmonic field along the z-axis. In the radial directions, the Ioffe field equalises the gradient produced by the quadrupole coils to produce a radially symmetric trap. When arranged appropriately, the three coils produce a magnetic field, $|\mathbf{B}|$, consisting of either two quadrupole traps or a harmonic trap with a magnetic bias, B_0, as shown in the right panel of Figure 2.8.

2.5 Forced evaporative cooling

To date, forced evaporation is the only method that can produce a Bose-Einstein condensate. Typically, evaporative cooling is implemented in a magnetic trap, however the condensation of Rb by evaporation in an optical dipole trap [98] opened up the possibility of cooling atoms with magnetically unfavourable scattering properties at low temperature [76]. In the present experiment, once the atoms have been loaded into the magnetic trap, they are cooled by preferentially removing high energy atoms from the trap while leaving the remaining atoms to re-thermalize to a lower temperature via elastic collisions. Radio-frequency transitions between different magnetic sublevels provide a spatially selective means of removing the most energetic atoms from the trap. The resonance between the magnetic field and applied RF radiation is defined by

$$|B_{cut}| = \frac{\hbar \omega_{ev}}{g_F \mu_B} \tag{2.6}$$

where ω_{ev} is the RF frequency and B_{cut} is the value of the magnetic field at which atoms interact with the RF mechanism. Atoms with an energy of approximately the truncation energy $E_{cut} = g_F m_F \mu_B (B_{cut} - B_0)$ have a high probability of being removed from the system via transitions from trapped to untrapped states. The precise probability can be calculated numerically via a set of coupled Schrödinger equations for the relevant interaction Hamiltonian[99, 100]. By continuously lowering the truncation energy the evaporation can be forced to proceed at a constant rate, which is parameterised by the truncation coefficient

$$\eta = \frac{E_{cut}}{k_B T} = \frac{g_F m_F \mu_B (B_{cut} - B_0)}{k_B T} = \frac{\hbar m_F (\omega_{ev} - \omega_0)}{k_B T} \tag{2.7}$$

where $\omega_0 = g_F \mu_B B_0 / \hbar$ is the resonance frequency at the trap minimum. The evaporation rate is defined as $\frac{1}{E_{cut}} \frac{dE_{cut}}{dt}$. A number of simple models [101, 103] can be used to predict the behaviour of the atomic cloud temperature as a function of the truncation coefficient and elastic collision rate. For sufficiently high cooling efficiencies, denoted by $\xi = d\ln(T)/d\ln(N)$, the elastic collision rate, $\tau_{el}^{-1} \sim n(0)T^{1/2}$ can actually increase as the cloud cools because of a dramatic rise in the peak density, $n(0)$. This effect routinely occurs in BEC experiments and is known as *runaway* evaporative cooling. In a real experiment, the efficiency of evaporative cooling is reduced because of the competition of other losses. These mechanisms are:

- 2-body collisions with hot background gas atoms, the rate of which depends on the quality of the experimental vacuum.
- 2-body inelastic collisions. The dipolar relaxation rate is directly proportional to n, the density of the atomic cloud.
- 3-body inelastic collisions. Molecule formation within the cold cloud occurs at densities on the order of 10^{14} atoms/cm^3 and the rate is proportional to n^2.
- absorption of stray resonant photons which each carry an energy of about 400 nK.

Monte-Carlo simulations provide a complete description of a typical evaporative cooling run, providing insight into how to optimise the cooling for realistic loss parameters [104]. Finally, sympathetic evaporation [73] has been used to cool multiple spin states and combinations of Li, Rb, and K.

2.5.1 Losses and magnetic trap lifetimes

Because the optical pre-cooling stage can provide only a finite number of dense cold atoms, BEC via evaporative cooling is a battle against the odds, as by definition this cooling method removes the majority of atoms from the trap. Apart from the need to operate evaporative cooling in a regime where the rate of elastic collisions (the thermalisation mechanism) exceeds inelastic two and three body collision rates (loss mechanisms), all other losses from the magnetic trap must be kept to a minimum. For a wide range of kinetic temperatures and densities, background gas collisions are the dominant loss mechanism [53]. Experimentally, these losses can be avoided by confining the atoms in an extreme ultra-high vacuum (UHV) environment. As mentioned above, Majorana flops (spin flip) losses due to atoms experiencing a magnetic field zero are avoided in IP traps due to a non-zero bias field at the trap minimum [94]. It is important to note the relationship between the trap lifetime (an indication of the quality of vacuum) and the elastic collision rate. The ratio, $R = \tau_{trap}/\tau_{elastic}$, should be greater than 400 to have the runaway evaporative cooling needed to reach the BEC transition [103]. Since the elastic collision rate is proportional to the geometric mean of the trapping frequencies, it is clear that as a general rule, the tighter the confinement, the less stringent the vacuum requirements (However, this condition can lead to large three body loss rates at low temperatures and high densities).

Finally, it should be mentioned that, although not usually considered in lifetime measurements, losses due to resonant photons appear to play a strong role in magnetic trap lifetime. Our measurements (discussed in chapter 3) reveal that the lifetime of atoms in our magnetic trap is half of our UHV MOT lifetime which indicates that resonant photons (to which atoms trapped in the MOT are not susceptible) are the dominant loss mechanism. This is despite extensive baffling of the experiment to block resonant light. Indeed, we find that further (extremely careful) baffling always increases the magnetic trap lifetime. At the pressures of interest Metcalf [85] calculates that the trapping time due to background collisions is $10^{-8}/P$, where P is the UHV pressure in torr. This indicates that a moderate pressure of 10^{-10} torr would provide a lifetime of 100 seconds which is more than adequate to produce BEC. Comments by other groups indicate otherwise [53]. For example, in the apparatus used by J. Walraven's group [105] the vacuum is measured to be below 3×10^{-11} torr but the magnetic trap lifetime is 64 seconds. According to Metcalf's estimate the lifetime of this trap should be well over 300 seconds. Similar reports from other groups also stress that a background pressure in the low 10^{-11} torr range is necessary to obtain magnetic trap lifetimes of one minute. Based on this apparent discrepancy, it appears that the lifetime in typical systems may be limited by stray resonant photons rather than by background gas collisions.

2.6 Calculating numbers and temperatures

In the absence of a robust, nondestructive, continuous measurement system for ultra-cold atoms, absorption imaging of cold clouds is used in the present experiments (described in detail in chapter 3). For this type of destructive imaging we are able to extract only a single image for each experimental run. It is therefore critical that the maximum amount of information be obtained from each image. From an image, we deduce the size of the cloud, its temperature and the number of atoms. All other quantities are derived from these measurements. This is true only of ultra cold clouds and long expansion times. For hotter clouds (5-150 μK), only the size and number of atoms can be accurately extracted from an image. Two consecutive images at different expansion times must be used to calculate temperature.

2.6.1 Calculating the atom number

We conservatively calculate the number of atoms assuming a closed transition on the $|2,2>$ to $|3',3>$ resonance via

$$N = \frac{2\pi}{3\lambda^2}\frac{(\Delta\omega)^2 + (\gamma/2)^2}{(\gamma/2)^2}\left(\frac{p}{M}\right)^2 \Sigma\O(x,y) \tag{2.8}$$

where λ is the wavelength of the imaging light, $\Delta\omega$ is the detuning from resonance, γ is the natural linewidth of the transition in angular frequency and p/M is the CCD pixel size (our pixels are square) divided by the magnification factor of the imaging system. $\Sigma\emptyset(x,y)$ is the sum over pixels of the optical depth measured at each pixel of the imaging CCD camera. The optical depth is found using the Beer-Lambert law [20] to write the intensity distribution $I(x,y)$ of the detection light after passing through the cloud as

$$I(x,y) = I_0(x,y)e^{-\emptyset(x,y)} \tag{2.9}$$

where $I_0(x,y)$ is the intensity distribution of the detection beam before absorption. Thus two images of the atomic cloud must be taken, the first with the atom cloud and a second 'bright field' image $I_0(x,y)$. A detailed understanding of Eq. 2.8 can be found by a combined reading of the review paper by W. Ketterle, D.S. Durfee, and D.M. Stamper-Kurn [53] and Siegman [9] (which includes a detailed discussion of the notorious factor of three).

2.6.2 Temperature calculations

There are three different regimes of the experiment in which one would like to accurately calculate the temperature of cold atoms. The first regime coincides with relatively hot atoms, such as those in a MOT, PGC or in the early stages of evaporative cooling. These large, hot clouds require two images (and hence two consecutive experimental runs) to accurately calculate the temperature, and the calculation stands on a very simple theoretical footing. The second regime is for much smaller, colder atomic clouds observed towards the end of evaporative cooling, but not Bose-condensed. Accurate measurement of the temperature requires only a single run of the experiment, but a more complex theory. In a gas just prior to, and below condensation, a semi-classical analysis of a single image may yield the temperature of the combined condensate-thermal cloud system [22]. In the following, we will briefly outline the relevant physical concepts and apply them to each of the aforementioned regimes.

Within the frame-work of the grand canonical ensemble, the total number of atoms at a temperature T in a trap is given by [22, 105]:

$$N = \sum_{n_x,n_y,n_z} \frac{1}{e^{(\epsilon_{n_x n_y n_z}-\mu)/k_B T} - 1} \tag{2.10}$$

where k_B is the Boltzman constant and

$$\epsilon_{n_x n_y n_z} = (n_x + \frac{1}{2})\hbar\omega_x + (n_y + \frac{1}{2})\hbar\omega_y + (n_z + \frac{1}{2})\hbar\omega_z \tag{2.11}$$

is the spectrum of exitations in a harmonic trap; n_x, n_y and n_z are integers, and μ is the chemical potential. When μ becomes equal to the energy of the ground state, the number of atoms in the this state approaches the total number of atoms in the system. Setting the number of atoms in the ground state to N_0 and substituting the chemical potential, $\mu = \frac{1}{2}\hbar(\omega_x + \omega_y + \omega_z)$, of the lowest energy state into the rest of the sum, one finds

$$N - N_0 = \sum_{n_x,n_y,n_z=1} \frac{1}{e^{\hbar(n_x\omega_x + n_y\omega_y + n_z\omega_z)/kT} - 1}. \tag{2.12}$$

where ω_n are the trapping frequencies in the directions (x, y, z). Converting the sum to an integral over n_x, n_y, and n_z and evaluating we have

$$N - N_0 = \frac{\zeta(3)}{\omega_x \omega_y \omega_z} \left(\frac{k_B T}{\hbar} \right)^3, \tag{2.13}$$

where $\zeta(3)$ is the Riemann zeta function. The critical temperature for a given number of atoms N at the phase transition is given by $(N_0 = 0)$

$$T_c \approx 0.94 \frac{\hbar \bar{\omega}}{k_B} N^{1/3}, \tag{2.14}$$

where $\bar{\omega} = (\omega_x \omega_y \omega_z)^{(1/3)}$ is the geometric average of the trapping frequencies.

The semi-classical density of an ideal Bose gas of atoms with mass M at thermal equilibrium is given by [22, 105]

$$n_{th}(x, y, z) = \frac{1}{\lambda_{dB}^3} g_{\frac{3}{2}} \left(\mathcal{Z} e^{\frac{-U(x,y,z)}{k_B T}} \right) \tag{2.15}$$

where $\lambda_{dB} = \sqrt{\frac{2\pi\hbar^2}{mk_B T}}$ is the de Broglie wavelength, $\mathcal{Z} = e^{\frac{\mu}{k_B T}}$ is the fugacity, $U(x, y, z) = \frac{1}{2}(\omega_\rho^2(x^2 + y^2) + \omega_z^2 z^2)$ is the cigar shaped trapping potential produced in the QUIC magnetic trap and $g_\alpha(\theta) = \sum_i^\infty \frac{\theta^i}{i^\alpha}$ is the polylogarithm (or Bose) function.

This distribution is significantly simplified well above the transition temperature T_c. In this limit $|\mu| \ll k_B T$ and $\mu < 0$, and the density distribution becomes Gaussian;

$$n_{th}(x, y, z) = \frac{N}{\pi^{3/2} \prod_{j=x,y,z} \sigma_j} e^{-\sum_{j=x,y,z} \left(\frac{j^2}{2\sigma_j^2} \right)} \tag{2.16}$$

where $\sigma_j = \sqrt{\frac{k_B T}{m\omega_j^2}}$ is the rms width of the distribution. Note that the density in this regime is separable as $n(x, y, z) = n(x)n(y)n(z)$. The final equation required for extracting temperature values from our images is the relationship between the initial velocity distribution and the imaged distribution at a time $t = \tau$. It is given by

$$\sigma_x^2(\tau) = \sigma_x^2(0) + \tau^2 \sigma_v^2, \tag{2.17}$$

where σ is the variance of a distribution [53]. Since the rms velocity for each degree of freedom in the trap is $\sigma_v = \sqrt{k_B T/m}$, and the initial variance is known from the above theories, then the temperature can be calculated from the variance of the experimental images, $\sigma_x^2(\tau)$. For example, using the variance of Eq. 2.16 leads to

$$T = \frac{m\omega^2 \sigma_x^2(\tau)}{k(1 + \omega^2 \tau^2)} \tag{2.18}$$

For the case of high temperature clouds we use Eq. 2.17 for each image taken on consecutive runs of the experiment, taking the difference of the values $\sigma_x^2(\tau)$ for each expansion time gives

$$T = \frac{m}{k} \frac{\sigma_x(\tau_2) - \sigma_x(\tau_1)}{\tau_2 - \tau_1}. \tag{2.19}$$

2.7 The Gross-Pitaevskii equation

To a very good approximation, the dynamics of a BEC can be described in terms of the time-dependent Gross-Pitaevskii (GP) or nonlinear Schrödinger equation for the macroscopic wavefunction of the condensate [106]. The GP equation has been successful in describing the macroscopic dynamics of trapped and un-trapped Bose-Einstein condensates in a variety of experimental situations [22]. The derivation of the GP equation is as follows. The standard many body Hamiltonian for a bosonic system is formulated in terms of the creation and annihilation operators $\hat{\Psi}^\dagger(\mathbf{r})$ and $\hat{\Psi}(\mathbf{r})$ which create or destroy a particle at position $\mathbf{r}$. The operators act on states of the form $|n_0, n_1, n_2, ...\rangle$ where the integer values n_x represent the occupation of some convenient orthogonal eigenvectors for the system of interest. In second quantised formalism, the Hamiltonian reads

$$\hat{H} = \int d\mathbf{r}\hat{\Psi}^\dagger \left[-\frac{\hbar^2}{2M}\nabla^2 + V_{ext}(\mathbf{r})\right]\hat{\Psi} + \frac{U}{2}(\hat{\Psi}^\dagger\hat{\Psi})^2, \tag{2.20}$$

where M is the mass of an atom, $V_{ext}(\mathbf{r})$ is the trapping potential, and a contact interaction potential, $U(\mathbf{r}' - \mathbf{r}) = \frac{4\pi\hbar^2 a}{M}\delta(\mathbf{r}' - \mathbf{r})$, with an s-wave scattering length of a (5.77 nm for ^{87}Rb $|2,2\rangle \rightarrow |2,2\rangle$) has been assumed [107]. We then write the Heisenberg equation of motion for the Hamiltonian using the commutation relations $[\hat{\Psi}(\mathbf{r}'), \hat{\Psi}^\dagger(\mathbf{r})] = \delta(\mathbf{r} - \mathbf{r}')$, $[\hat{\Psi}^\dagger(\mathbf{r}), \hat{\Psi}^\dagger(\mathbf{r}')] = 0$ and $[\hat{\Psi}(\mathbf{r}), \hat{\Psi}(\mathbf{r}')] = 0$:

$$i\hbar\frac{\partial\hat{\Psi}}{\partial t} = \left[-\frac{\hbar^2}{2M}\nabla^2 + V_{ext}(\mathbf{r})\right]\hat{\Psi} + \frac{4\pi\hbar^2 a}{M}\hat{\Psi}^\dagger\hat{\Psi}\hat{\Psi}. \tag{2.21}$$

As discussed in the introduction to this thesis, we now take the field to be of the form:

$$\hat{\Psi}(\mathbf{r}, t) = \Phi(\mathbf{r}, t) + \hat{c}(\mathbf{r}, t), \tag{2.22}$$

where $\Phi(\mathbf{r}, t) \equiv \langle\hat{\Psi}(\mathbf{r}, t)\rangle$. $\hat{c}(\mathbf{r}, t)$ is the annihilation operator for uncondensed particles and has the property that $\langle\hat{c}(\mathbf{r}, t)\rangle = 0$. $\Phi(\mathbf{r}, t)$ is the order parameter, having the meaning of a macroscopic wavefunction of the condensate so that $|\Phi(\mathbf{r}, t)|^2$ is the density of atoms. These approximations, and the range of their validity are discussed in some detail in the recent work by Stenholm [23]. Substituting (2.22) into the equation of motion and taking the expectation value of both sides we find:

$$i\hbar\frac{\partial\Phi}{\partial t} = \left[-\frac{\hbar^2}{2M}\nabla^2 + V_{ext}(\mathbf{r})\right]\Phi + \frac{4\pi\hbar^2 a}{M}\Phi^*\Phi^2 + \frac{4\pi\hbar^2 a}{M}[2\Phi\langle\hat{c}^\dagger\hat{c}\rangle + \Phi^*\langle\hat{c}^2\rangle + \langle\hat{c}^\dagger\hat{c}^2\rangle]. \tag{2.23}$$

The first term in the square brackets, $2\Phi\langle\hat{c}^\dagger\hat{c}\rangle$ is known as the normal density and represents all trapped atoms not in the BEC. The term $\Phi^*\langle\hat{c}^2\rangle$ is the anomalous density related to spatial correlations between atoms. The final term represents three body effects. Assuming that nearly all particles are in the condensate, we can, to a very good approximation, neglect all terms in the square brackets to obtain the well known Gross-Pitaevskii equation:

$$i\hbar\frac{\partial\Phi(\mathbf{r}, t)}{\partial t} = -\frac{\hbar^2\nabla^2}{2m}\Phi(\mathbf{r}, t) + V_{trap}(\mathbf{r})\Phi(\mathbf{r}, t) + \frac{4\pi\hbar^2 a}{M}\Phi(\mathbf{r}, t)|\Phi(\mathbf{r}, t)|^2 \tag{2.24}$$

The external trapping is usually of the form

$$V_{trap}(\mathbf{r}) = \frac{m}{2}(\omega_x^2 x^2 + \omega_y^2 y^2 + \omega_z^2 z^2), \tag{2.25}$$

where $\omega_{x,y,z}$ are the characteristic frequencies of the trap along corresponding axes.

In a large condensate ($>$ 1000 atoms) the interaction energy is significantly larger than the kinetic energy of the atoms. In this situation the condensate is well approximated by an inverted parabolic density profile (the Thomas-Fermi approximation) [110]. In 3D the density profile is:

$$n(x,y,z) = \frac{1}{U_{int}}(\mu - U(x,y,z)) \qquad for \quad \mu > U(x,y,z) \tag{2.26}$$

where $U_{int} = \frac{4\pi\hbar^2 a}{M}$ is the two-body interaction strength. The condensate chemical potential $\mu = \frac{1}{2}(15a\hbar^2 M^{1/2}\omega_z\omega_\rho^2 N)^{2/5}$ (significantly modified by the presence of interactions) is determined from the normalisation condition

$$N = \int_V n(x,y,z)dxdydz = \int_0^{\pi}\int_{-z_{TF}}^{z_{TF}}\int_0^{r_{TF}} \frac{1}{U_{int}}(\mu - U(r,z))rdrdzd\theta \tag{2.27}$$

where V is the volume of the condensed cloud, $z_{TF} = \sqrt{\frac{2\mu}{M\omega_z^2}}$ and $r_{TF} = \sqrt{\frac{2\mu}{M\omega_\rho^2} - \frac{\omega_z^2 z^2}{\omega_\rho^2}}$.

If a coherent coupling mechanism between trapped and untrapped states is used to extract atoms from the condensate, as described in later chapters of this thesis, the macroscopic behaviour of the output beam of the atom laser can also be described by a spatio-temporal evolution equation similar to Eq. (2.24).

2.8 Atom laser output coupling

Mewes et al [3] demonstrated the first atom laser output coupler based on the application of pulsed radio-frequency (RF) fields to induce controlled spin flips from magnetically trapped to un-trapped states of a Bose-Einstein condensate. Later it was shown by Hagley et al [4] that pulsed Raman output coupling could be used to achieve a quasi-continuous multi-state atomic beam. Bloch *et al* [5] achieved continuous RF output coulping for up to 300ms, producing a single state atom laser beam, and showed that this beam could be coherently manipulated in direct analogy to the optical laser [6, 7, 15]. Both Raman and RF output couplers can be used in the pulsed or continuous regime, however there has been no demonstration of a continuous Raman atom laser. In addition to the methods mentioned above, an atom laser can also be produced by coherent tunneling of atoms from trapped to un-trapped states. Anderson and Kasevich demonstrated this scheme using a BEC loaded into a tilted optical lattice [111]. This produced a vertical array of trapped condensates. Gravitational acceleration induced tunnelling between the traps, and the interference between the condensates resulted in pulses of atoms. More recently an atom laser was demonstrated by lowering the depth of an optical trap containing only $m_F = 0$ atoms [117]. The RF output coupler forms the basis of the experiments

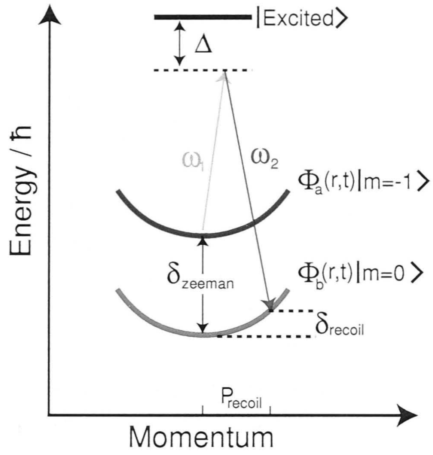

Figure 2.9: Schematic representation of the Raman coupling mechanism following [4], and described in the text.

described in chapter 4, and its workings are described in detail in that chapter. In the following we briefly outline the Raman output coupling mechanism, on which the model of atom laser pumping in chapter 5 is based.

2.8.1 Raman output coupling

Raman coupling of two atomic levels was originally suggested as a mechanism for atom laser outcoupling by Moy et. al. [59], and demonstrated experimentally by Hagley et al [4] in pulsed mode in 1999. This outcoupling method has been well studied theoretically by a number of groups (see eg. [118, 119]. The scheme is based on the stimulated absorption and emission of photons from two laser beams. The process is coherent, and inherently controllable. When a magnetically trapped atomic state is coupled to a magnetically untrapped state a highly collimated and directional atomic beam is produced. The Raman output coupling scheme [120] can be described as follows. Let us imagine an atom in the trapped BEC occupying the magnetic quantum state $\Phi_a(\mathbf{r},t)|m=-1\rangle$, as shown in Fig. (2.9). We apply laser fields with a frequency difference $\delta = \omega_2 - \omega_1$ to the atom. Both lasers are detuned by an amount Δ from the intermediate atomic energy level $|Excited\rangle$ to suppress spontaneous emission. A Raman transition occurs when the atom coherently absorbs a photon from ω_1 and is stimulated to emit a photon into ω_2, thus changing its internal state to an untrapped magnetic level, $\Phi_b(\mathbf{r},t)|m=0\rangle$. This process is reversible and untrapped atoms can be coherently transferred back into the condensate. An atom, initially at rest, acquires a kinetic energy of $\hbar\delta_{recoil} = \hbar^2(\mathbf{k}_2 - \mathbf{k}_1)^2/2m$ where $\mathbf{k}_{1,2}$ are the wavevectors of the lasers and m is the mass of the atom. The laser geometry can range from co- to counter-propagating, and this will determine, in part, the magnitude and the direction of momentum kick received by the atoms. Conservation of energy requires that the detuning of the lasers must account for the total change in energy of the atom, thus $\hbar\delta = \hbar\delta_{zeeman} - \hbar\delta_{recoil}$. The directional momentum kick the atoms receive in this output coupling scheme produces a number of effects which are not present in the RF output coupler. Firstly, the output coupler does not require gravity to operate, and hence the atoms can be pushed in any direction. For example, with a total detuning of $\delta/2\pi = 6.4$ MHz between the Raman lasers (and the correct relative orientation) an output pulse could be kicked directly upward at least 0.5 mm before beginning to fall under gravity. Secondly, it may be experimentally feasible to localize the output coupling region to a small part of the condensate by adiabatically expanding the condensate and by tightly focussing the Raman lasers. Finally, the momentum kick reduces the interaction time between output coupled atoms and the condensate, leading to a significantly reduced transverse momentum width in the atom laser [4]. The interaction energy between atoms is released in a time $t < 1/\omega_\rho$ (for the magnetic trap described in this thesis $t < 0.6$ ms). If the output coupled atoms leave the condensate in a time much shorter than this, they will not feel the repulsive mean field of the condensate and their momentum width will be smaller. For example, it takes a gravity driven RF atom laser pulse about 1 ms to fall across a condensate $5\mu m$ wide in the radial direction. A Raman output coupled pulse with the previously mentioned detuning crosses the condensate in $50\mu s$, well below the time require for interactions to broaden the momentum distribution.

CHAPTER 3

The atom laser source

The source for an atom laser is provided by Bose-condensed atoms in a magnetic trap. Our original BEC machine, constructed over a period of 2 1/2 years by Jessica Lye, Cameron Fletcher, Ulrich Kallmann and John Close, produced Bose-Einstein condensation of ^{87}Rb on 3 May, 2001. The results of that work are presented in the PhD dissertation of Dr. Jessica Lye. A number of months later it was decided by the group that the machine needed a major upgrade in order to produce and study atom lasers; in particular a new magnetic trap was required. In this chapter we will discuss in detail the construction of the ANU's second generation BEC machine from design to the production of a condensate. The work presented in this chapter was undertaken solely by the author.

3.1 Magnetic trap MkII

The first ANU BEC machine was constructed around a QUIC magnetic trap, a simple, low current trap created from three many turn solenoids [97]. The first trap made by the group (designed by Cameron Fletcher) consisted of three elaborately water cooled coils each on separate mounts. The smaller Ioffe coil was conically shaped to allow access for MOT laser beams, while the quadrupole coils were mounted on a substantial copper inner tube. The quadrupole coil formers were split to reduce eddy currents and the Ioffe coil had a solid copper core. It was decided that, because of our accumulated experience with the QUIC magnetic trap, a similar system should be constructed for the next machine. The 'BEC MkII' trap was designed at an intermediate stage of the trap optimization work presented in Chapter 6. For the trap described in this chapter, we used an iterative refining of the trap properties and were able to design a trap to run at 25 A with trapping frequencies of approximately $\omega_\rho = 2\pi \times 320$ Hz and $\omega_z = 2\pi \times 21$ Hz for the radial and axial trapping frequencies of the $|F = 2, m_F = 2\rangle$ state, according to Eq. 2.4. The designs for this trap are shown over the following pages. Our ultra high vacuum glass cell sits relatively high off the optical bench and hence a substantial mounting system was required for the mechanical stability of the magnetic trap. This system proved useful in two ways, the first was that it allowed all coils to be placed exactly perpendicular to one another. Secondly, micrometer adjustment allowed straightforward and extremely accurate positioning of the Ioffe coil. Once

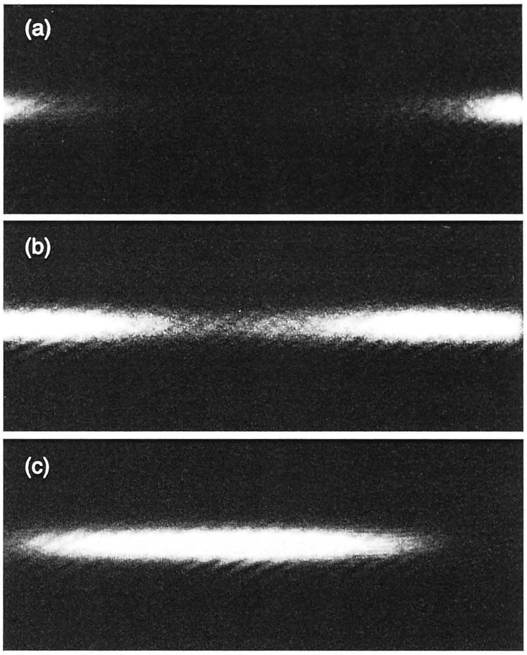

Figure 3.1: Formation of the Ioffe-Pritchard trap. In-situ absorption images of $\approx 30\ \mu K$ atoms after 2 sec in the magnetic trapping potential. The images (a),(b) and (c) were taken on consecutive runs of our experiment, the only adjustment being a small number of turns of the micrometer screw controlling the position of the Ioffe coil. The current in the coils is 25 A.

atoms had been transferred to the quadrupole trap, it was a simple matter to screw in the Ioffe micrometer and watch for the formation of the Ioffe-Pritchard trap as shown in Figure 3.1. This process typically took only 10 to 15 minutes to complete. The quadrupole coils had large inner radii to allow complete optical access to the BEC. In addition, the Ioffe coil was also designed with a 4 mm hole for axial optical access to the BEC. Design of the magnetic coils was primarily undertaken using the commercial software 'BiotSavart' [121]. The program was checked for accuracy against analytic expressions for the axial field of a finite solenoid and found to be in good agreement. The final design of the magnetic coil system was arrived at through an iterative method, as follows:

- Given the glass cell size (36mm×36mm, wall thickness is approximately 4mm), the internal diameter of the quadrupole coils can be chosen so as to give complete optical access to the glass cell, say 30 mm inner diameter. The outer diameter and length of the quarupole coils was then assigned to give a desired magnetic field gradient. The Ioffe coil is somewhat more complicated. The axial curvature along the Ioffe coil scales as R^3/I, where R is the external radius of the coil and I, the current, and hence at the currents achievable by our present power supply (< 40 A) the average radius of the coil should be kept to a minimum. The coil must be conically shaped, or tapered, in order to accommodate the diagonal MOT beams. The internal diameter of the Ioffe coil should be large enough to allow good optical access to the BEC and the external diameter is limited by the position of the quadrupole coils to around 38 mm.

- Once geometric considerations have been taken into account, the winding wire should be chosen to achieve a reasonable balance between diameter and length (resistance) and inductance (number of windings).
- Consideration should be given to the construction of the coil formers and positioning system, taking into account the availability of the various components.
- Finally, the configuration can be programmed into BiotSavart, the relative position of the coils can be fine tuned and the currents can be adjusted to achieve the desired trapping frequencies.

Generally, one must repeat this process many times to find the right combination of geometry, components, and current.

In hindsight, the methodology described above was simplistic, and we later developed a rigorous technique for optimising our magnetic traps which is described in Chapter 6 of this thesis.

3.1.1 Trap construction

The trap former is made of three plates of solid aluminum, with a large 35 mm hole drilled at 45 degrees for MOT beam access. This former provides a solid base for the three coils of the magnetic trap (see Figure 3.2). Each coil former is made from a copper block, split to avoid eddy currents. In the present design, the split faces toward the aluminum base plate and the water cooling loops over the top. We should have reversed this with the split facing uppermost. As it stands, the aluminum base plate completes a full loop allowing for the possibility of eddy currents. We have not noted any ill effects from this. In particular, the measured coil switching times were around 400 μs. The coil formers were shaped such that brass guides, set square with one another, and placed around them, allowed the coils to slide easily in and out from the glass cell. Micrometers were mounted behind the coils and allowed precise forward positioning of each coil individually. A number of M4 nuts were placed along each guide so that, when the coils had been finely positioned with the micrometers, they could be firmly bolted into place. The coils themselves were wound directly onto the copper formers using a manually turned lathe and a teflon friction feed-through for the wire to keep tension. The quadrupoles were wound in one sitting using a teflon front former. Each layer was wound and then a thin (but complete) covering of a high thermal conductivity epoxy resin (Cotronics, Duralco 132) was applied before winding the next layer. The outermost layer had a 2 mm layer of epoxy resin to fully encapsulate the coil for mechanical strength. The Ioffe coil was wound one layer per day in a similar manner to the quadrupoles, however

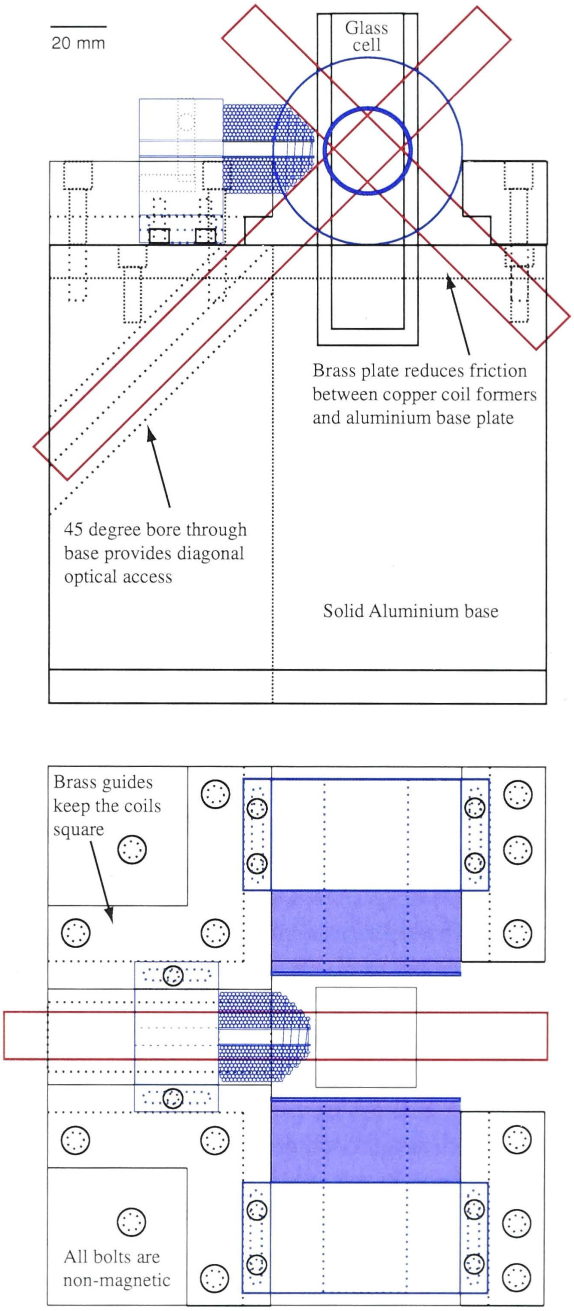
20 mm
Glass cell
Brass plate reduces friction between copper coil formers and aluminium base plate
45 degree bore through base provides diagonal optical access
Solid Aluminium base
Brass guides keep the coils square
All bolts are non-magnetic

Figure 3.2: An overview of the magnetic trap construction diagrams, showing the diagonal MOT beams and brass guides for the coils. The red boxes represent the path our diagonal MOT laser beams follow.

we found it very difficult to keep the wire tracking correctly in order to match the design specifications. In the final design, we used wire diameters of 1.4 mm for the Ioffe coil and 1.6mm for the quadrupole coils.

3.1.2 Coil geometry

The final geometry of the coils is as follows (see also Fig. 3.3): the quadrupole coils have an internal radius of 16.675 mm (defined as the radius to the cross-sectional centre of the first layer of wire) and an external radius of 32.075 mm (defined in the same way). The internal radius is determined by the copper tube available - 31.75 mm OD. They are 18 windings long and are wound staggered to give a length of 29.6 mm. The coils are layered 12 deep. The total number of turns is 216. The total length of wire used in each coil is 32 m giving a resistance of 0.317Ω. The Ioffe coil has an internal radius of 3.84 mm (defined as the radius to the cross-sectional centre of the first layer of wire) and an external radius of 15.54 mm (defined in the same way). The internal radius was determined by the copper tube available - 6.35 mm OD. The length of the Ioffe is 32.585 mm, with the conical section being approximately 12mm long. The coils are layered 10 deep. The total number of turns is 212. The total length of wire used is 12 m, giving a resistance of 0.176Ω. A sequence of photographs showing the fully assembled trap is presented in Figure 3.4.

3.2 Trap characterisation

A number of properties of the magnetic trap are important to an experiment in Bose-Einstein condensation, and need to be measured to fully characterise the magnetic trap, these are:

- Trap power dissipation, which is a significant contributing factor to the stability of the magnetic trap through heating effects.
- Magnetic field strength, an important indicator that the coils have been built to specification.
- Direct measurement of the trap frequencies, once the trap is installed. In particular, for our three coil design, there is some uncertainty about the final positions of the coils around the trap due to the micrometer fine tuning of the relative coil positions.
- Coil inductance and switching times. These are less important as one can use an external scheme to speed up switching, such as that described in section 3.3.

3.2.1 Power dissipation

Power dissipation was measured by running the coils at a given current and measuring the voltage. These tests were done over short intervals of approximately

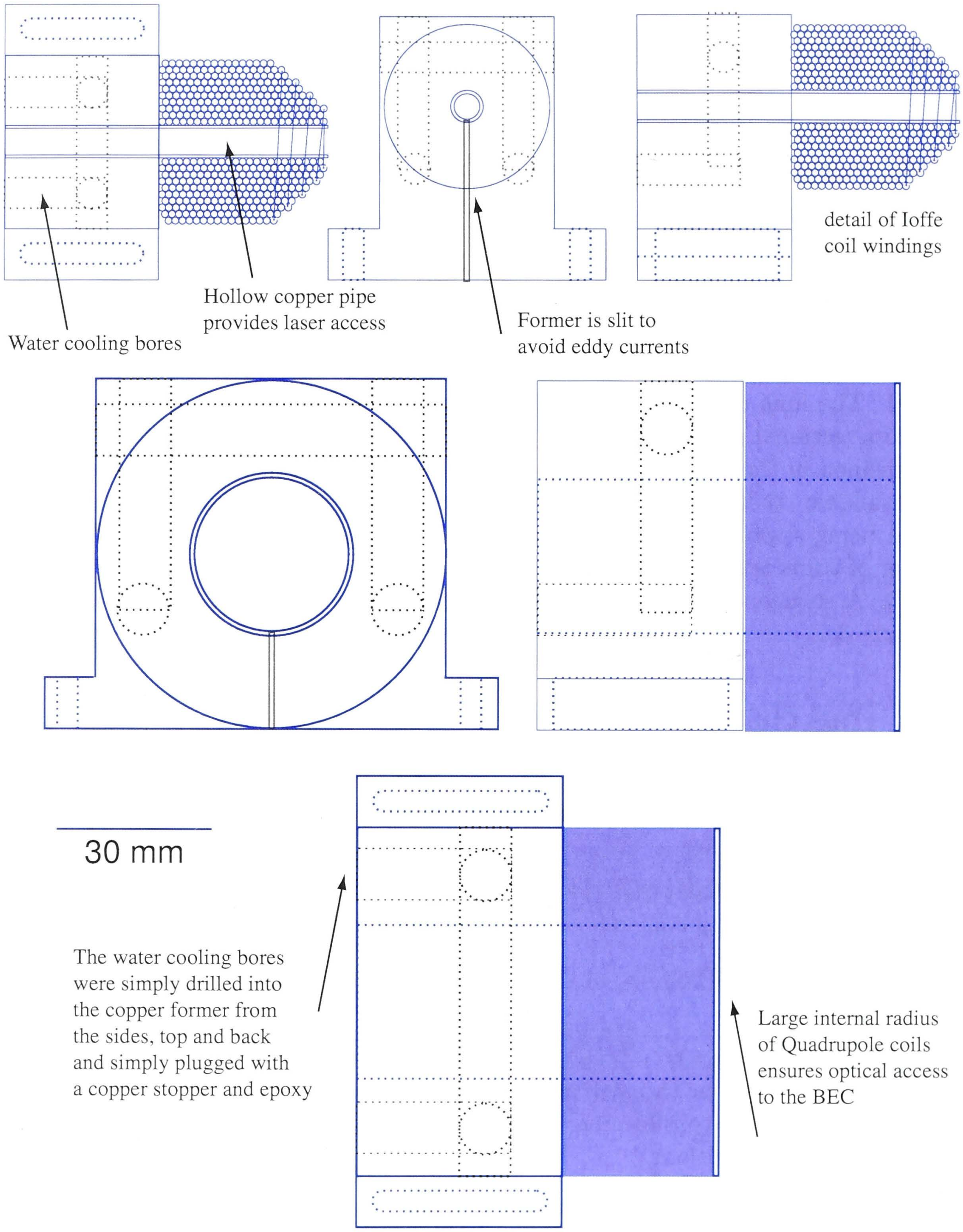

Water cooling bores

Hollow copper pipe provides laser access

Former is slit to avoid eddy currents

detail of Ioffe coil windings

The water cooling bores were simply drilled into the copper former from the sides, top and back and simply plugged with a copper stopper and epoxy

Large internal radius of Quadrupole coils ensures optical access to the BEC

Figure 3.3: Some details of the quadrupole and Ioffe coils. Note the water cooling bores in the copper formers and the positioning guides along the side of each former.

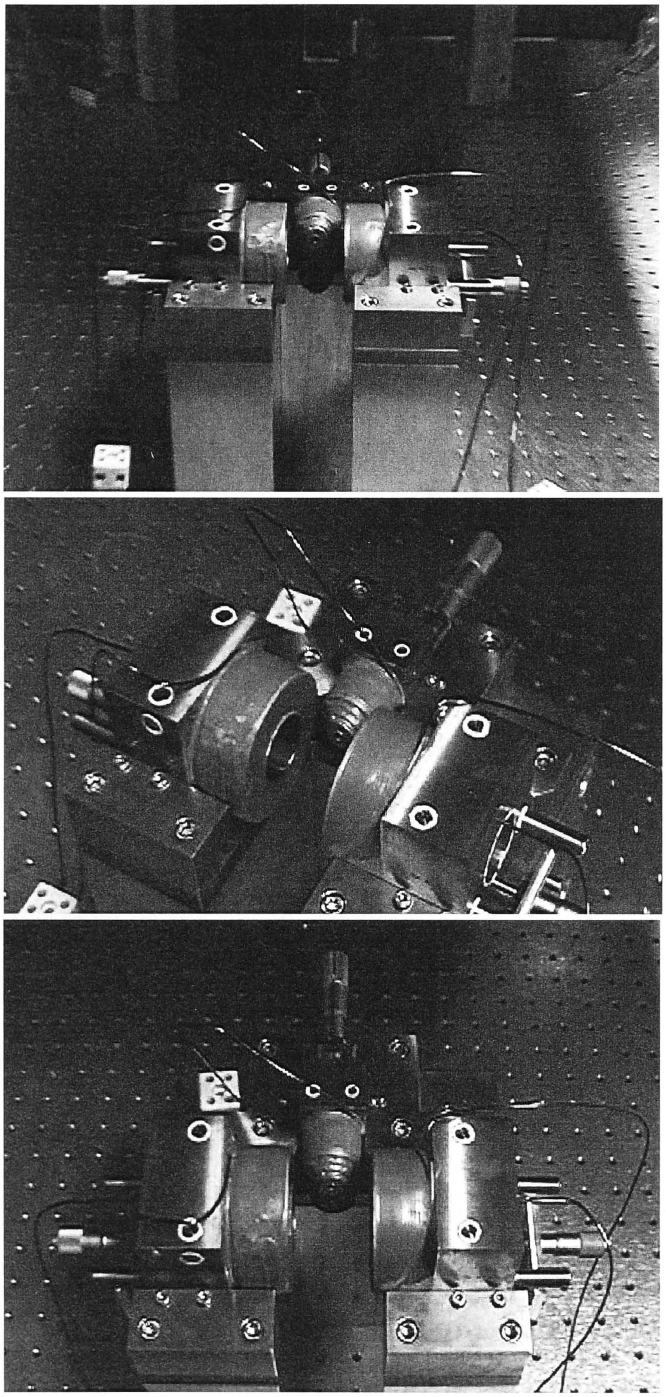

Figure 3.4: A sequence of images showing the assembled trap complete with micrometer screws, just prior to installation around the vacuum chamber. Scale: Optics table holes are 2.5 cm apart.

25 seconds to imitate the duty cycle of our original BEC machine, and matched the theoretically calculated values (from $P = I^2R$). However, initially, we did not measure the *equilibrium* power dissipation, which is achieved by imitating the complete duty cycle of the BEC experiment for about an hour. If we had done so, we would have discovered that the Ioffe coil has a high resistive heating over a number of consecutive runs resulting in a significantly higher equilibrium power dissipation for the overall system of approximately 700 W when run at 25 A - a significant portion of which was dissipated in the Ioffe coil leading to temperatures above 70 degrees in this coil. This places an uncalculated burden on the water cooling system of the Ioffe coil. If the water pressure stays constant then the magnetic trap displays reliable operation. However, during the daytime hours the pressure fluctuated significantly leading to experimental repeatability issues. Due to this constraint, the machine was run mainly in the early hours of the morning (2am-9am) to take advantage of the low demands on the university water system at this time of night.

3.2.2 Magnetic field strength

The magnetic field strength was measured for each of the coils independently as well as in the Ioffe-quadrupole configuration. We made the individual coil measurements to ensure that the coils had been wound to specification, and found that the Ioffe coil did not match specifications (as we had expected when winding it) running at around 78 percent of its expected magnetic field strength. This correction was included into the full model of the coil system reducing the expected trapping maximum trapping at 25 A to $\omega_\rho = 2\pi \times 260$ Hz and $\omega_z = 2\pi \times 20$ Hz for the radial and axial trapping frequencies of the $|F = 2, m_F = 2\rangle$ state according to Eq. 2.4. The coils were then arranged in the full Ioffe-quadrupole configuration and measured with a Hall probe (model) with an accuracy of ± 0.01 G in 100 G full range. The probe was mounted on an xy translation stage and data was taken along the Ioffe axis. The quadrupole coil spacing was measured with a micrometer, however the Ioffe coil position was uncertain at the mm level relative to the centre of the quadrupole trap. In comparing the model and experimentally measured magnetic field, the model coil was moved in until the Ioffe trap first formed. The field along the Ioffe coil was then plotted versus the measured data and showed excellent agreement between our theory and the constructed coils, as shown in Figure 3.5. Although the final configuration of the coils provided more than adequate performance, the conical Ioffe coil proved to be the weak link in the system.

3.2.3 Measurement of trap frequencies

To measure the trapping frequencies, we took advantage of the first collective excited mode of the magnetically trapped atoms, termed the "Kohn" or sloshing mode [122, 22]. The trap frequencies were measured using small clouds (10^6) of ≈ 1 μK atoms, produced via an evaporative cooling run down to 1 MHz (trap minimum was at 770 kHz). An additional coil was placed along the Ioffe axis (coil radius 15 cm and placed 25 cm away from the centre of the quadrupole coils) and a small current

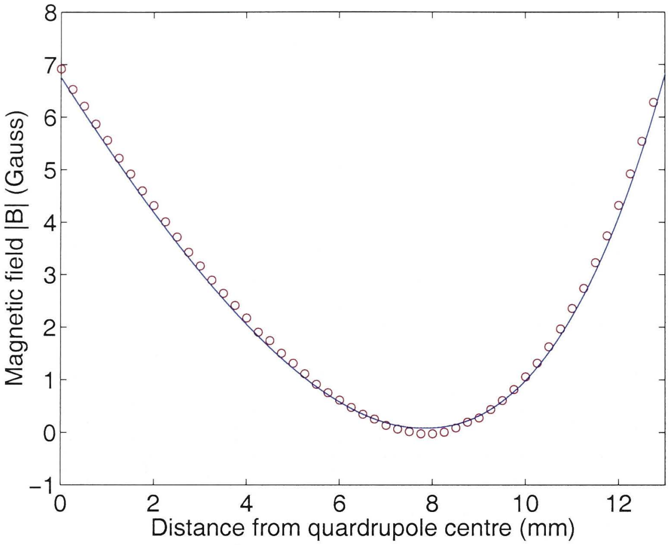

Figure 3.5: Comparison between the theoretical model of the Ioffe-Pritchard trap and magnetic probe measurements taken with the coils running in series at a current of 3 A. The data show the field along the weak trapping axis. Open circles are the experimental data.

(6 A) was used to displace the minimum of the Ioffe trap towards the centre of the quadrupoles (maximum displacement 24 μm). This 'push' coil was then abruptly turned off ($< 50\mu s$), and at intervals increasing by 5 ms in each consecutive run, the cold cloud was imaged in-situ. The center of mass of the excited cloud was plotted as a function of the evolution time. This yielded the measurement of the weak axial trapping frequency $\omega_z = 20$ Hz as shown in Figure 3.6(a). In order to measure the tight radial trapping frequencies, we installed a second pulse generator to act as a variable delay to the imaging pulse. This allowed us to image the trapped atoms at below the temporal resolution of the computer control program (limited in a practical sense to 1 ms time steps). For this measurement, a coil was added along the quadrupole coil axis, and a drive of 200 Hz was applied for 5 seconds. The atoms then evolved freely in the trap until an in-situ image was taken. This was done at intervals of 200 μs over 7 ms. A sine wave was fitted to the data yielding a tight trapping frequency of $\omega_\rho = 253$ Hz as shown in Figure 3.6(a).

3.2.4 Magnetic trap lifetime

Although the magnetic trap lifetime is not a property of the magnetic trap, it is essential that this figure be measured. It is the ratio of good (elastic) to bad (inelastic) collisions that plays a large part in determining whether runaway evaporative cooling will be successful or not (see section 2.5.1). We measured the trap lifetime using a 50 push loading cycle, followed by PGC, optical pumping

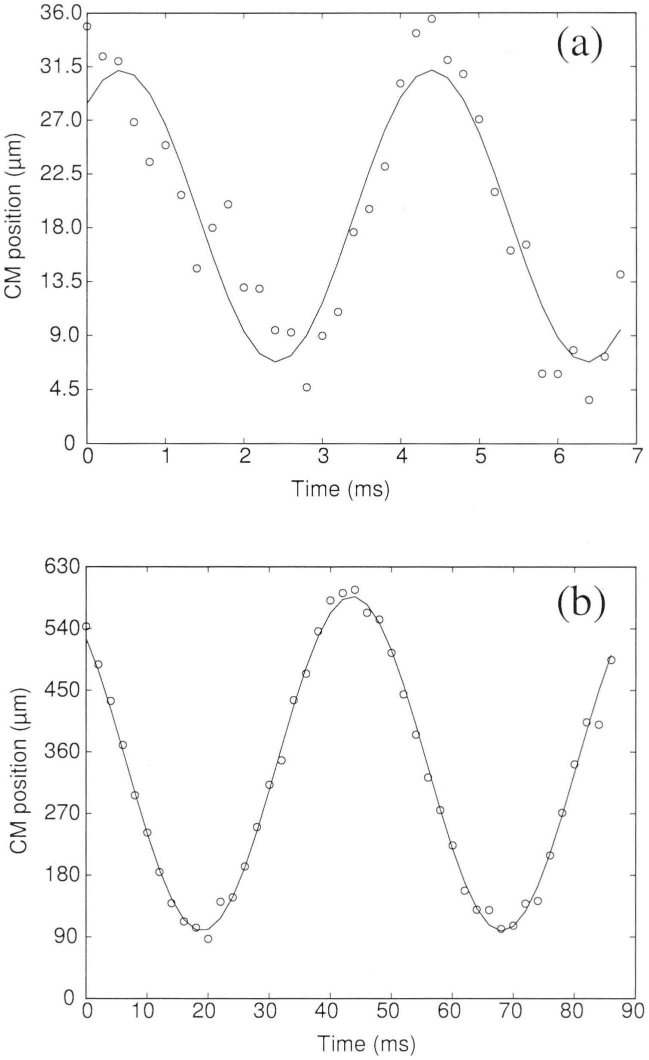

Figure 3.6: Trapping frequency measurements as described in the text. Shown are measurements of the centre-of-mass motion of (a) Tight radial trapping frequency ω_ρ. (b) Weak axial trapping frequency ω_z. Error bars on both measurements are approximately $\pm 2\mu m$.

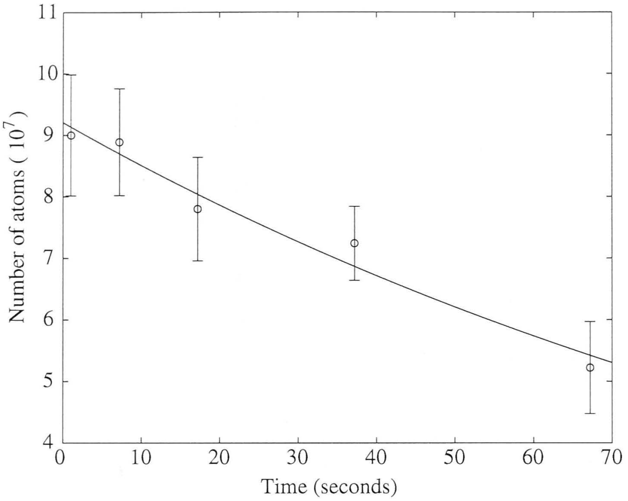

Figure 3.7: Magnetic quadrupole trap lifetime as described in the text. The temperature of the atoms in these measurements is 45 μK.

into the F=2, m_F=2 state, and capture in a 12 A (~ 120 G/cm axial gradient) quadrupole trap. The number of atoms remaining in the trap was measured at 1, 7.2, 17.2, 37.2, and 67.2 seconds (see Figure 3.7) via 10 ms expansion absorption imaging. Each data point represents 10 separate runs of the experiment. An exponential decay ($e^{-t/\tau}$) fitted to the data via a least squares algorithm yields a lifetime of of τ = 126 seconds. According to the discussion in section 2.5.1, this indicates a background gas pressure of 8×10^{-11} torr. In a further experiment, we measured the background collision rate using a continous fluorescence measurement on a small MOT. As pointed out by Myatt *et al* [101], at low trapping laser intensities with small numbers of trapped atoms, collisional losses due to radiative and density effects are negligible, and the background collision rate can be directly measured. We measured lifetimes of up to τ = 250 s via this method (calculated from a 50 s oscilloscope trace of the MOT flourescence). This indicates that the magnetic trap lifetime is still limited by losses due to absorption of stray resonant photons reaching the magnetic trap through our baffling rather than from background gas collisions (see discussion in section 2.5.1). Indeed, with every increase in the amount of protective baffling around the magnetic trap, we observe an increase in the magnetic trap lifetime.

3.3 Magnetic trap switching scheme

Our updated switching circuit is shown in Figure 3.8. The idea behind this scheme was to make it as simple and robust as possible. A similar scheme was described in the thesis of Dan Stamper-Kurn [95], and a detailed discussion of switching (including feedback techniques) is given by Dedman et. al. [124]. In

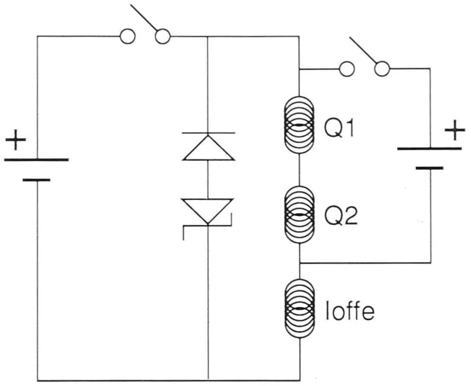

Figure 3.8: Magnetic trap switching scheme as described in section 3.3.

order to minimise the current noise in the trap, the three main coils are run in series with no other components (such as a resistor or FET) except the solid state switch (which we expect to eliminate in the future by using fast power supplies designed specifically for inductive loads (Kepco BOP 20-20M)). A diode/zener diode pair brings the current in all coils to zero within 500 μs as shown in Figure 3.9, and our measurements of the magnetic field decay (using a small test coil) agree, indicating that eddy currents are not a significant problem in the current setup. The trap switch on is limited by our main power supply (1200 W) and although the initial switching occurs in a couple of ms there are oscillatory fluctuations up to 100 ms later caused by overshoot in the power supply control circuit as shown in Figure 3.9. A second (set of) analogue controlled power supply is connected around the quadrupoles coils to run the MOT. At present this supply is limited to 10 A, 90 V. This supply is completely removed from the switching circuit during the early part of the evaporative cooling in order to obtain a clean switch off of the magnetic trap at the end of an experimental run. The analogue control of the two power supplies allows an extremely smooth ramping of the coil currents. At the beginning of the experiment the quadrupole coils are run from the MOT power supply at 1.2 A for 55 seconds. The MOT power supplies are abruptly switched off for PGC and then switched back on at 10 A 5 ms later to catch the atoms in a quadrupole magnetic trap. The main supply is then ramped up while the MOT supply is ramped down. The trajectories for the currents are calculated via a simple Matlab script to ensure that the transfer of atoms from the quadrupole to Ioffe trap has smooth acceleration and deceleration.

3.4 Optical pre-cooling

All optical cooling and magnetic trapping occurs within the original vacuum system designed by Dr. John Close and constructed and baked by Dr. Close, Dr.

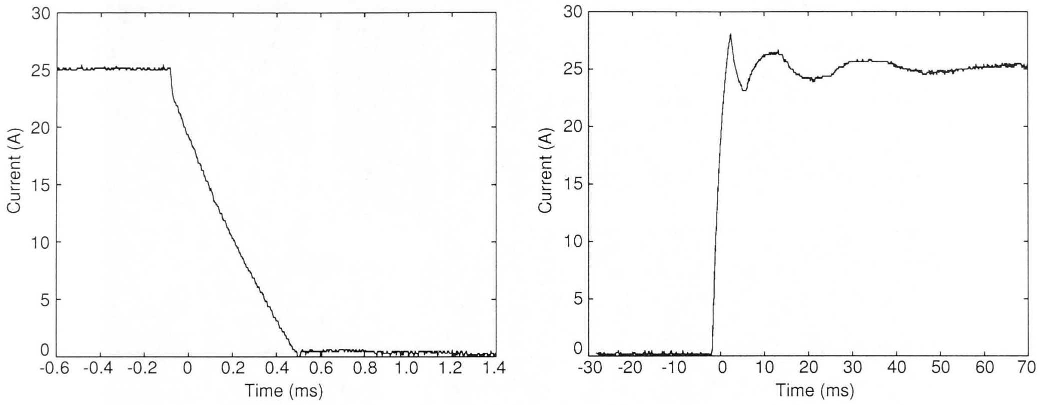

Figure 3.9: Experimental switching times. This figure shows a measurement of the current flowing in series through all coils as measured by a home built current shunt (constructed by Cameron Fletcher) placed in series with the coils. Left image is trap switch off, while right is trap switch on. Optical isolators were used to ensure accuracy of the measurement.

Kallmann, Dr. Lye and Cameron Fletcher. The rubidium used in the experiment is sourced from an SAES dispenser, installed a number of centimetres away from the centre of the collection MOT. The original Rb dispenser is still running after 4 years of steady operation. This is in contrast to the 1-2 years reported by other groups.

The geometry of the vacuum setup is illustrated in Figure 3.10. We use a vertical double MOT system for atomic cooling prior to magnetic trapping. This system provides a good compromise between simplicity and relatively high atom number. The principle of this system is to separate the vapour cell MOT (fast loading, or 'collection', MOT) from a UHV pre-magnetic trapping MOT ('science' MOT) and is discussed in detail by Myatt et al. [123] for a ^{85}Rb system. As shown in figure 3.10, the upper and lower MOTs are separated by 500 mm, with the previously mentioned impedance closest to the upper MOT. We use no guiding system and this combined with the large distance between the collection and science MOTs places some limitations on the system that will be discussed in the section on push loading.

In replacing the magnetic trap, the entire lower MOT optical system, including imaging and pumping optics had to be removed from the experiment (the empty table can be seen in the top panel of Figure 3.4). Once the magnetic trap and associated water cooling had been installed this 'clean slate' provided an obvious opportunity for us to implement a number of simplifications and additions to the optics system. These are discussed in the following sections and are summarised in the list below.

- Fluorescence based number counting was implemented on both MOTs.

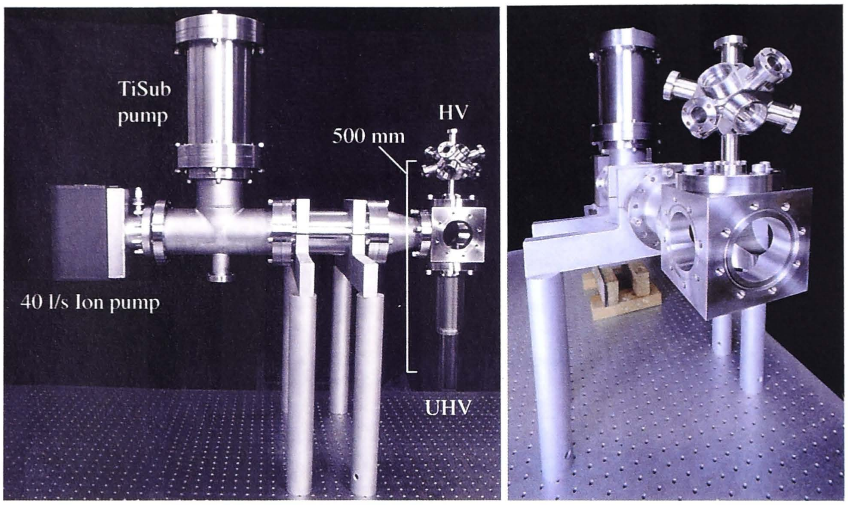

Figure 3.10: Two images of the main vacuum system. The right image shows the relative position of the main pumps and the HV and UHV chambers of our machine. The left image shows some details of the collection MOT chamber, which was machined from a single block of stainless steel.

- $F = 2 \rightarrow F' = 2$ light was added to the system for optical pumping.
- The lower MOT was rebuilt as a 3 beam retro-reflection system rather than a 6 beam configuration.
- A new camera and imaging system was added.
- A system of 3 sets of Helmholtz coils were added to better compensate Earth's magnetic field for improved molasses temperatures.

3.4.1 Fluorescence measurement of atom number

A clear path for improvement in the original apparatus was to add real-time atom number diagnostics to the upper and lower MOTs allowing us to remove our dependence on unreliable (very easily saturated) mini-ccd cameras for tuning the optical stages of the experiment. In particular, we were able to make quantitative measurements of the number of atoms in the upper and lower systems, and to optimise the transfer efficiency between the two MOTs. The current flowing from a photodetector can be related to the number of atoms in the MOT by considering the number of photons collected in a given solid angle from a fluorescing atomic sample. Let us say that the scattering rate per atom is given by R in photons/atom/second. Then the number of photons collected/second/atom is

$$n = \frac{RA}{4\pi r^2} \tag{3.1}$$

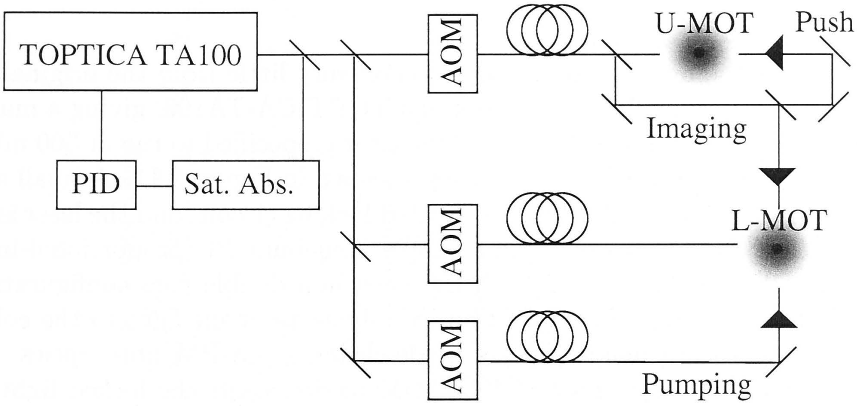

Figure 3.11: An overview of the optics of the experiment. The three AOMs drive the upper and lower MOTs and pumping. Imaging light used on the lower trap is derived from the upper MOT laser system as is the push light. The imaging light is shunted to the lower table by a shuttered telescope.

where A is the area of the collection region and r the distance to the collection region. We consider reflection losses to be minimal, which appears justified by the excellent agreement in atom numbers between self-calibrating absorption imaging and fluorescence measurements. The power in W/atom is

$$P_{atom} = \frac{RA}{4\pi r^2}\frac{hc}{\lambda}, \tag{3.2}$$

where λ is the wavelength of the resonant light and h is Planks constant. The current per atom produced by the collection photodiode is P_{atom} scaled by the quantum efficiency of the photodiode, η,

$$I_{det} = \frac{\eta RA}{4\pi r^2}\frac{hc}{\lambda}. \tag{3.3}$$

Hence for a given number of atoms, N, the current produced by the detector is

$$I_{det} = \frac{N\eta RA}{4\pi r^2}\frac{hc}{\lambda} \tag{3.4}$$

We connect our detector directly to an oscilloscope with an input impedance of Ω. Then the number of atoms as a function of the display voltage, V, on the CRO is given by

$$N = \frac{4\pi r^2}{A}\frac{1}{\eta}\frac{\lambda}{hc}\left(\frac{1+\frac{I}{I_{sat}}+4(\frac{\Delta\omega}{\delta})^2}{\frac{I}{I_{sat}}\pi\delta}\right)\frac{V}{\Omega} \tag{3.5}$$

The term in brackets is the inverse of the scattering rate R [40, 79]. The quantum efficiency of our photodiode (Coherent model No, 818SL) is $\eta = 0.45A/W$.

3.4.2 The laser system

This part of the optics system has changed very little from the original implementation by the group. The main laser is a TOPTICA-TA100, giving a maximum power of 300 mW after a 60 dB isolator (the laser is specified to run at 500 mW post isolator). A general overview of the optics is shown in Figure 3.11. A small amount (5 mW) of light is sent to a Zeeman-modulated locking circuit, and the laser is locked to the $F = 2, F' = 1, 3$ crossover via a simple homebuilt PI (proportional-integral) locking loop. Two AOMs (110 ± 20 MHz) each in a double pass configuration upshift the light to the trapping transition, supplying resonant light to the collection and science MOTs independently via mode-cleaning SM-PM fibre optics. In addition, we added a single pass 60 MHz AOM to downshift the locked light to the $F = 2, F' = 2$ transition for optical pumping. This light is also fibre coupled. The optical losses from this system are considerable; each pass through an AOM attenuates the light by 20% and the best coupling of the (shaped) TOPTICA-TA100 light to the fibre is 55%. Thus only about 100 mW is available to supply the upper and lower traps, imaging, pumping and push systems. In an ideal world the loss of power would be significantly offset by the benefits of the AOM control; they should provide 'instant' (10 μs) control of the laser frequency and power. Unfortunately, this is not the case for laser power control. The extinction ratio of the AOMs is specified at 1000:1 and they must be combined with mechanical shutters (Uniblitz) to completely extinguish the laser light. In addition, we have found an extremely poor response of the AOMs to sudden power changes. Figure 3.12 shows the measured response of the post-fibre laser power, measured with a 1 GHz photodetector, after a 'TTL on' signal is sent to our AOM controllers. We have found similar effects across a number of different commercial AOM controllers. Thus for many of the fast pulses required in the experiment (such as imaging and pumping) the applied power is significantly lower than the measured CW power. When the machine is running at its full 90 s duty cycle the loading efficiency of the collection and science MOTs is also degraded by this extremely slow switch on.

3.4.3 Upper MOT

The upper collection MOT vacuum chamber was constructed by Mr. Brett Brown (technical staff) from a single piece of solid stainless steel. It has six 1-inch optical ports for the MOT beams, oriented such that a standard cartesian configuration (x, y, z), with z vertical, has been rotated 45 degrees around the x-axis and the x-axis lifted 45 degrees from horizontal. A pair of opposing ports oriented vertically provide optical access for the push beam and the vacuum impedance leading to the UHV chamber. Four viewports, the vacuum pump and a feed-through for the dispensers complete the system. The magnetic coils for the MOT are mounted directly on one pair of the MOT ports. The coils operate at a calculated 18 G/cm gradient from 6 A, and, like the main magnetic trapping coils, are switched with a diode/zenner diode pair. The MOT is run in a 3 beam retro-reflected configuration [38]. The main points of the upper MOT optics system are shown and described

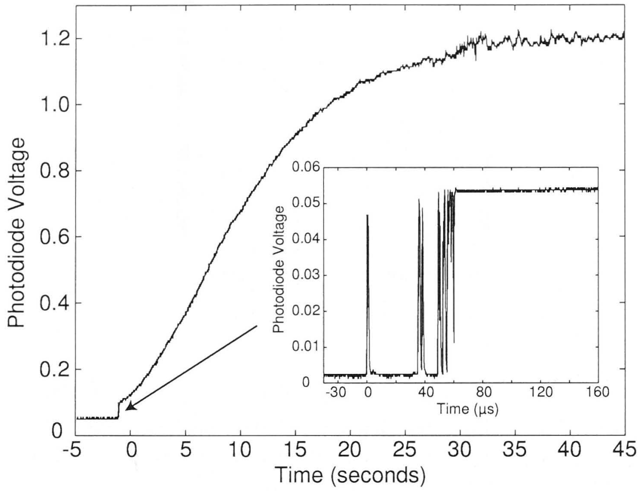

Figure 3.12: The figure shows laser power measured on a photodiode after an AOM has been switched from zero to full RF amplitude.

in Figure 3.13. Implementation of the photodiode fluorescence measurement on the collection MOT revealed that the maximum number of atoms achievable with the original optics setup was 3×10^7 atoms. This number was iteratively optimised with respect to the MOT vapour pressure, alignment, magnetic field gradient, detuning and laser power. We were guided in this optimisation process primarily by Ref. [125], and our final conclusion was that beam size was the limiting parameter. Almost an order of magnitude increase in the number of atoms (to $\approx 1.5 \times 10^8$) was achieved by replacing a number of key 1-inch mirrors with 2-inch optics to allow the transmission of full 1-inch beams to the MOT.

3.4.4 Push loading

After a short loading time (200 ms), the collection MOT beams and coils are momentarily turned off and a vertically oriented 5 ms pulse (via shutter control) of circularly polarised light is focused into the centre of the MOT. This has the effect of 'flinging' a large fraction of cold atoms down into the lower UHV vacuum chamber, through the 5 cm by 5 mm impedance. If the transfer conditions are right, the science MOT can collect some of these atoms and, with multiple loading and push cycles, a large number of trapped atoms may be built up in UHV. Ultimately the maximum number of atoms collectable in the science MOT is a function of the number of atoms transferred per second from upper to lower MOTs and the loss rate from the lower MOT. In the following two sections, we discuss the optimisation of a single push to transfer the maximum number of atoms between the two MOTs, and the optimization of the lower MOT for maximum total number of atoms from multiple loads.

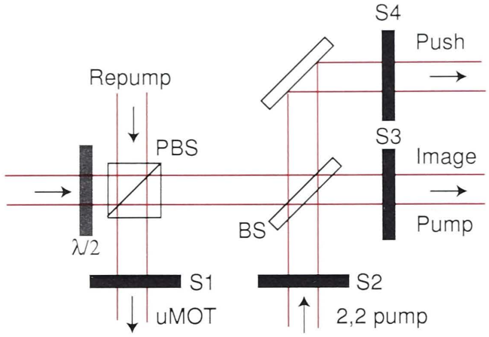

Figure 3.13: Detail of the upper MOT shuttering system. Shutters are S1, S2, S3 and S4. The trapping light from the left has exited from a fiber and is mixed with the repump on a PBS. The power is primarily shunted to the upper MOT. A small amount of trapping and repump light is sent to a 50:50 non-polarizing plate beamsplitter, the reflected light being used as a shuttered push beam and the transmitted light for imaging in the lower MOT. Also mixed on this beam splitter is the $F = 2, F' = 2$ pumping light which is also sent to the lower MOT. Under normal operation only S1 is open, for the push S1 is closed and S4 simultaneously opened. For imaging in the lower trap only S3 is open. Finally for pumping in the lower trap, the upper MOT AOM is switched off and S2 and S3 are opened.

3.4.5 Optimising a single push

In contrast to the original work by Myatt *et al* [123], we do not use any kind of magnetic guiding to help the atoms from upper to lower MOTs, mainly due to the design of the vacuum system. The large cube cross and round section of the glass cell do not lend themselves to the mounting of magnetic guides (see figure 3.10). An alternative that would not require guiding (and that around which the system was originally designed) would be to use a moving molasses push [126, 127]. In this configuration, a six beam MOT would be used whereby the magnetic fields are switched off and the upward (downward) propagating lasers beams are frequency down (up) shifted. This creates polarisation gradients of a couple of metres per second that would throw the atoms down to the lower trap with very little heating. The elaborately constructed upper MOT vacuum chamber and its very close proximity to the upper optics table meant that independent upward propagating MOT beams would have been very hard to implement. Thus our system was arrived at, comprising a simple 3 beam retro-reflected MOT and a single resonant push beam. The fluorescence measurement was invaluable in understanding and debugging the push system. In an initial measurement of the number of atoms being pushed from the upper MOT (defined as the difference in the number of atoms in the upper MOT before and after a single push pulse), we found that only about 13% of the atoms were being removed. The fluorescence from the lower MOT indicated that essentially 100% of the pushed atoms were being caught (about 10^7 atoms for a

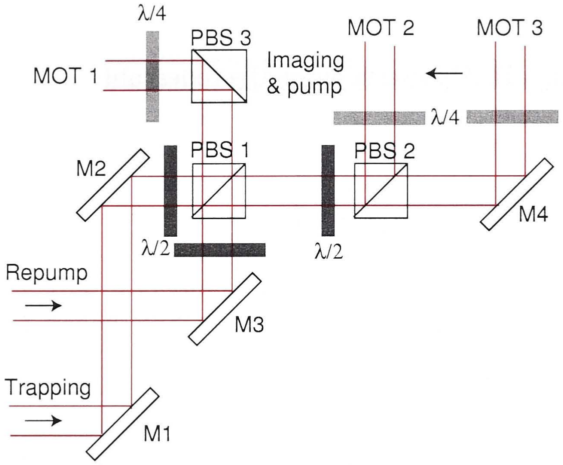

Figure 3.14: Schematic of the lower MOT optics. The imaging and pumping beams are mixed into the 'quadrupole' MOT beam at PBS 3.

single push). Previously reported work [101] indicated that an overall transfer efficiency from MOT to MOT of about 90% could be expected from a single push with a magnetic guiding system. Hence, our system was performing just as well, if not better than a system with guiding. With some adjustments of the push beam focus and intensity, we were able to boost the number of atoms being pushed from the upper MOT to almost 95 %, however despite many attempts we could never capture any more than $1 - 2 \times 10^7$ atoms per push into the lower MOT. This effect cannot be due to 'clipping' of the larger number atomic pulses as they travel through the impedance between the upper and lower systems, since the size of the large and small clouds is very similar. The expansion of the approximately 250 μK clouds over the 20 ms it takes for them to travel between upper and lower systems is also negligible. Myatt [101] reported a similar capture efficiency of 15% when guiding fields, both permanent and electromagnetic, were completely turned off. As each guiding system was switched on they reported an increase in the transfer efficiency, indicating that their lower MOT characteristics were not limiting the transfer of atoms. Myatt's transfer system was oriented at 45 degrees to vertical but collisions of the pushed atoms with the walls due to gravitational sag alone would have been negligible over the 20 ms push time they reported. In our system we speculate that our lower MOT single shot capture efficiency is limited by the parameters of the *lower* MOT.

The results of this study were that the push system was set such that the collection efficiency of the transfer to the lower MOT was as close to 100% as possible. This results in 13% of the atoms from the upper MOT being transferred to the lower MOT with each push.

3.5 Lower MOT

A critical point in a BEC experiment is the repeatable loading of a high number of atoms into the magnetic trap. The stability of the lower science MOT plays a considerable part in this process, and in our second generation BEC machine, we have significantly simplified many parts of the optical setup in pursuit of repeatability. Despite being used extensively in countless research and undergraduate labs around the world, the temporal and spatial behaviour of magneto-optical traps is not well understood in the limit of large numbers of atoms. The large MOTs achieved in UHV are renowned for their unpredictable behavior to the point where one of W. Ketterle's students labelled the tweaking of the MOT components for the maximum number of trapped atoms as "voodoo" [128]. In contrast, the Doppler and sub-Doppler cooling of atoms in a purely optical trap (molasses) has been thoroughly investigated and is known to occur due to polarisation gradients in the overlapping laser beams of the molasses [129]. A number of careful studies of MOT performance have been conducted [130, 131] and have demonstrated that MOTs operate in three different regimes related to small, medium and large atom number. In the large number limit, MOTs generally consist of a cold core of atoms surrounded by a diffuse hotter cloud, corresponding to the bimodal shape of the magneto-optical trapping potential [132, 133]. The spatial distribution of this diffuse cloud is very sensitive to small changes in beam profile, intensity and alignment and this can lead to significant fluctuations in the maximum number of atoms that can be held in the trap [132]. In our system, the maximum load rate of atoms from the collection MOT is about 6×10^7 atoms per second (this corresponds to 4 loads per second with each load transferring an average of 1.5×10^7 atoms). The number of atoms, N, in the lower MOT can be described by a simple rate equation of the form

$$\frac{dN}{dt} = r - \left(\frac{1}{\tau_1} + \frac{1}{\tau_2}\right) N \tag{3.6}$$

where r is the loading rate, τ_1 is the lifetime of atoms in the MOT due to collisions with background atoms and τ_2 represents other losses such as light assisted collisions [81]. The UHV MOT operates in a regime where background gas collisions are minimal. When the MOT is run at low intensities, with small numbers of atoms we measure MOT lifetimes in excess of 250 seconds. However, under the typical experimental conditions needed to trap large numbers of atoms, light assisted collisions dominate the loss rate (with lifetimes corresponding to about 10 seconds). With our loading rate, we need a MOT lifetime of at least $\tau_2 = \frac{N_{max}}{r} = \frac{5 \times 10^9 atoms}{6 \times 10^7 atoms/s} = 83$ s. Thus the parameters of the MOT that theoretically allow large numbers, lead to large light assisted collision rates and, in our system, to two orders of magnitude less atoms in the steady state than would be expected if light assisted collisions were not taken into account (down from 1.5×10^{10} to 6×10^8). This is the real crux of making a BEC in a double MOT system, and is the reason why the number of atoms reported by most groups in the lower MOT does not vary widely. Of course, simply raising the loading rate will dramatically increase the steady state number of atoms in the MOT. The MIT group uses this to great effect with their

Zeeman-slower [134], and more recently Dieckmann *et al* [105] demonstrated that a $2D^+$-MOT can also supply the massive flux required to beat light assisted collisional losses and trap over 10^{10} atoms in a few seconds.

3.5.1 The repumper

In combination with techniques to maximise the loading rate of the UHV science MOT, gains can be made by removing atoms from the resonant MOT light by manipulating the ratio of atoms in $S_{1/2}F = 2$ and $S_{1/2}F = 1$ states via the repump light. By 'shelving' atoms in the 6.8 GHz detuned $S_{1/2}F = 1$ state light assisted collisional losses can be significantly reduced. The MIT group invented the 'dark-spot' MOT [80] in which the central part of the repump laser beam is blocked - atoms in the central part of the MOT quickly fall into the F=1 state and no longer interact with the resonant light. This system was used primarily to obtain a density increase in the UHV MOT, but it was quickly pointed out by the JILA BEC group that this system can be used to boost the lifetime of atoms in the MOT if light assisted losses are a limiting factor to peak atom number [81]. We are extremely limited in our control of repump light in our experiment. The light is locked to the appropriate transition and we can turn it on and off via a shutter, but that is the extent of our manipulation of this section of the experiment. The total power from the repump is 12 mW and this supplies both upper and lower MOTs. The repump is distributed equally between the three lower MOT beams. By careful adjustment of the cw intensity of the repump (and hence the time atoms spend in the F=1 dark state) we achieve longer MOT lifetimes and hence larger numbers of atoms at the end of a loading cycle. We achieve repeatable UHV MOTs of 8×10^8 atom as measured by fluorescence and absorption imaging. Since calculation of numbers for both measurements assume a spin polarised sample, which the atoms in the MOT are not, the actual numbers are probably closer to three times this value.

3.6 Three steps to stability

Further to the measures described above to reach a large atom number in the lower MOT, we also require repeatable behaviour from the system. Three main changes to the lower MOT optics system were made and are described below. When combined, these techniques achieved a high level of stability ($\approx \pm 8\%$ of final atom number after PGC) in the lower MOT. We were able to run our machine for almost three months without a single adjustment to any optics (except optimisation of fibre coupled power).

3.6.1 Retro-reflection lower MOT

In its previous incarnation, the machine had operated with a six independent beam lower MOT. This construction was based on comments from NIST/JILA regarding beam attenuation in large MOTs [135]. However in our situation the

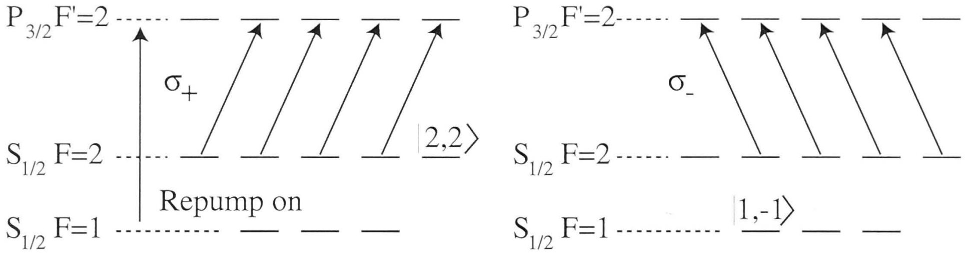

Figure 3.15: Schematics of optical pumping with σ_+ (left) and σ_- (right) light.

MOT beams are oriented diagonally in the vertical plane due to the geometry of the vacuum system; alignment of six beams in this setup is difficult and the number of optics required (compared to a retro-reflect setup) doubles. Based on the idea that a simplified system would be more reliable, and that other groups had reported BEC with three beam setups [97], we rebuilt the MOT in the simplified configuration. All optics were upgraded from 1 to 2-inch diameter to reduce overall alignment and beam clipping issues, and the system was designed so that all reflection angles were 45 degrees to preserve polarisation. In order to balance the power in the retro-reflected beams the lasers were slightly focused [130].

3.6.2 Polarizing beam splitters

A combination of half-wave plates and large polarizing beam splitter cubes are used to shunt lasers around the lower MOT (see Figure 3.14). The benefits of this system are three-fold; it is straightforward to adjust the powers in each MOT beam for a 1/3 split, no light is wasted, and the power-splitting is insensitive to small changes in angle of the splitters (the latter is not the case for plate beamsplitters).

3.6.3 Gaussian beam profiles

Traditionally in our lab we have always expanded our MOT beams to 3-4 cm 1/e Gaussian beams and then apertured using an iris to produce a 1.5 cm diameter beam with essentially a constant intensity ('top hat' beam profile). We have found no indication in the existing literature that this would affect the MOT stability. Nevertheless, we decided to trial a reduction of the beam expansion in the lower MOT so that the majority of the Gaussian beam profile fell within a circle of 1.5 cm diameter. After reducing the overall power so it was equivalent to the original apertured beam we noticed an immediate and dramatic improvement in the repeatability and spatial structure of the lower MOT. Without further study we cannot confirm this effect, as it may have occurred due to some unknown subtlety of the alignment.

3.7 Optical pumping

Generally, in a magneto-optic trap, atoms are distributed approximately equally across all hyperfine states. In order to achieve high transfer efficiencies from the MOT to the magnetic trap, we need to spin polarise the atoms into a magnetically trappable state. For ^{87}Rb, we have a choice between the $S_{1/2}F = 2, m_F = 2$ and $S_{1/2}F = 1, m_F = -1$ states. We initially chose the $F = 2, m_F = 2$ state, as the characteristic frequency of the magnetic trap is $\sqrt{2}$ larger than that for the other state. The higher trapping frequency leads to higher collision rates which are advantageous for evaporative cooling. Cornell and Wiemann showed that by controlled misalignment of a MOT one can achieve significant spin polarisation [38]. However, having created the large, stable MOT described in the previous section, we use optical pumping to achieve the desired result. A circularly polarised beam is pulsed on for 5 ms and directed through the quadrupole coils as shown in Figure 3.17. A small pumping coil is place between the front face of the first quadrupole coil and the glass cell to provide a fast switching magnetic field of about 0.5 G to provide a well defined quantisation axis for the optical pumping. Thus the atoms react to σ_+ light which drives transitions with $\Delta m_F = +1$. If the repump light is left on for the duration of the optical pumping cycle, all the atoms in the sample are quickly polarised into the $|F = 2, m_F = 2>$ 'dark' state, illustrated schematically in the left panel of Figure 3.15. Alternatively by reversing the magnetic field and shuttering the repump the atoms can pumped into the $|F = 1, m_F = -1>$ state as shown in the right hand side of Figure 3.15.

To demonstrate the effectiveness of optical pumping for spin polarising the sample, we have included the sequence of images in Figure 3.16. The atoms have been transferred from a polarisation gradient cooled sample of 8×10^8 atoms into a quadrupole magnetic trap, where they are held for 200 ms (long enough for all un-trapped atoms to fall away), released and then imaged with σ_+ light after a 20 ms expansion. We have varied the steps taken to optically pump the atoms prior to the magnetic trap being switched on. In (a) we have not used the magnetic coil to provide a quantisation axis. In (b) the coil is used in conjunction with σ_+ light tuned to the $F = 2$ to $F' = 3$ transition (the same configuration used to image the atomic clouds). This is the optical pumping scheme used in the original machine. In (c) the coil is used with the newly installed AOM supplying pumping light coinciding with the $F = 2$ to $F' = 2$ transition. In (d) the optical pumping time was doubled. This resulted in almost 95% of the PGC atoms being transferred to the magnetic trap. This pumping scheme is extremely robust due to the dark state and, providing the pumping laser power remains constant, we have found little variation in the machine's performance at this step.

3.8 New imaging system

We can take an absorption image of the cold cloud at any time during the experiment from the beginning of the lower MOT loading cycle to after the formation

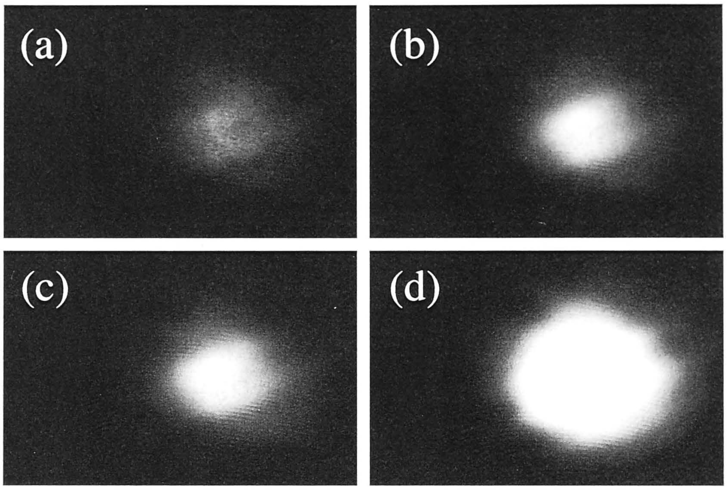

Figure 3.16: Experimental demonstration of the effect of optical pumping on the number of atoms transfered to the magnetic trap. Explanation of figure can be found in section 3.7.

of the BEC. Of course, some adjustments must be made to image at each end of the imaging scale. The imaging beam enters the system along the same path as the pumping laser (as shown in Figure 3.17). We use σ_+ light tuned to the $F = 2$ to $F' = 3$ transition (quantisation provided by the pumping coil). We use a 2 inch lens with a focal length of 10 cm, placed approximately 15.7 cm from the atoms. The CCD camera, a Photometrics SenSys with $9\mu m$ square pixels and a 786 × 512 array is placed in the image plane 27.5 cm from the lens (M=1.75). The camera is mounted on a stabilised x,y,z translation stage to allow precise positioning at the image plane. Because the imaging beam follows the same path as the MOT beam a quarter wave plate and polarising beam splitter cube are placed after the imaging lens. The MOT beam polarisation is arranged such that it is deflected by the PBS while the image beam travels straight through. A mirror is placed at the focus of the MOT beam to create the retro-reflect system. Careful attention to polarisations in the experiment keeps losses to a minimum. For physically large atomic clouds such as the MOT, a demagnifying lens is added to the system, and the camera is shifted 8mm on the translation stage such that the centre of the CCD array coincides with the centre of the MOT. The magnification of the imaging system was calibrated using free falling atomic clouds, and compared favorably with the calculated magnification.

3.9 Summary of optical pre-cooling and transfer

In this section, we include a brief summary of the steps used in the current experiment including some of the exact timing and powers used in the optical part of the experiment. An optical cooling cycle begins with the lower and upper MOT

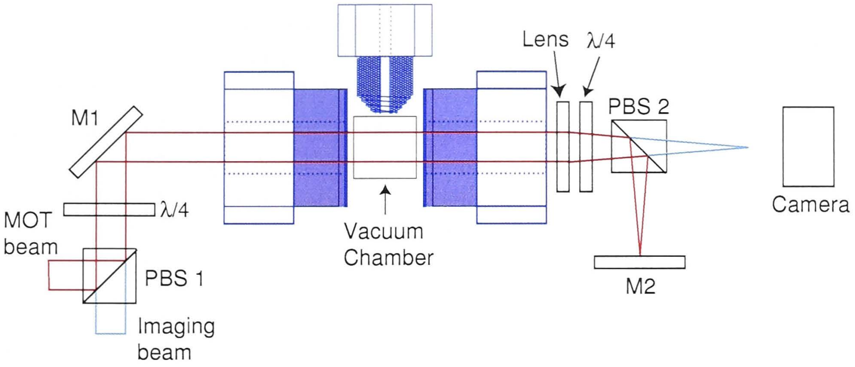

Figure 3.17: Schematic of the imaging system. Optical pumping light also follows the imaging beam path.

light and coils being switched on (Upper MOT: 18G/cm quadrupole trap, 12 MHz detuned and 14mW total power into three retro-reflected 2 cm Gaussian beams. Lower MOT: 12G/cm quadrupole trap , 14 MHz detuned and 20mW total power into 3 retro-reflected 1.5 cm Gaussian beams). The upper MOT fills for 250 ms. The MOT light and coils are switched off momentarily (5 ms) and a pulse (5 ms) of near resonant light (12 MHz detuned) controlled by a shutter, pushes atoms from the upper to lower MOT, after which the upper MOT light and coils are switched on again. This process is repeated about 200 times and fills the lower MOT to 10^9 atoms. The upper MOT light is then extinguished via the AOM and shutters. The lower MOT is allowed to settle for 100 ms. The lower MOT lasers are de-tuned a further 8 MHz to 22 MHz for 20 ms, and then the quadrupole coils are abruptly switched off via the analogue control of the secondary power supplies. The lower MOT lasers are left on for a further 4 ms of PGC [129] before being extinguished. The pump coil is then switched on and the pump pulse applied for 2 ms. The quadrupole coils are switched on again via the secondary power supply to their maximum of 10 A. The lower MOT light and repump light are entirely extinguished with shutters and the AOM at this point. The atoms are now in the dark. The primary power supply is ramped up and the secondary supply ramped down creating an adiabatic compression [136] as the atoms are transferred to the full Ioffe trap for evaporative cooling.

3.10 Evaporative cooling

We use the simplest conceivable scheme to achieve evaporative cooling to BEC. An SRS345 signal generator set to a maximum output power of 7 dBm is triggered to produce a *single* 25 sec logarithmic sweep from 30 MHz to $\approx$ 770 kHz. The signal amplitude is controlled via an external RF analogue switch (minicircuits); this gives a much better extinction ratio than the built-in analogue amplitude control. The signal is then fed to a 35dB RF power amp (minicircuits) with a maximum input power of 7 dBm. The signal from the power amp is transferred to the RF antenna via a shielded coaxial cable. We spent a significant amount of time investigating the optimum winding of the RF coil, including using a tuned capacitor and impedance matching [137]. Our research led us to the conclusion that a small single loop of wire (30mm diameter, 1mm enamelled copper wire) with a capacitor tuned resonance gives the largest magnetic field amplitude over the range of frequencies (30-0.5 MHz) used in the experiment.

3.11 Fitting to column density

In an absorption image of the atomic cloud, the intensity of the absorbed light is proportional to the column densities of the three dimensional atomic distributions

$$\tilde{n}(x, z) = \int n(x, y, z)dy, \tag{3.7}$$

and hence the fitting functions described in chapter 2 must be similarly integrated for an accurate calculation of the temperature. In the high temperature regime the separable density distributions retain the same form in 2D as 3D. As discussed in section 2.6.2, the thermal distribution for very cold clouds is given by

$$\tilde{n}_{th}(x, z) = \tilde{n}_{th}(0, 0) \frac{g_2\left(\mathcal{Z} e^{\frac{-U(x,z)}{k_B T}}\right)}{g_2(\mathcal{Z})}, \tag{3.8}$$

and the column density of the condensate is given by

$$\tilde{n}_c(x, z) = \frac{4\sqrt{2}}{3U_{int} m^{\frac{1}{2}} \omega_{rho}} (\mu - U(x, z))^{\frac{3}{2}} \tag{3.9}$$

Our fitting algorithm runs as follows (with reference to a sample data set presented in Figure 3.18) :

- A region of interest is specified in the absorption image (no larger that 256*256)
- The maximum optical depth Ø is found in this region, and two vectors through this point are extracted ($V_x(x, 0)$ and $V_z(0, z)$).
- These vectors are analysed and a decision is made as to whether to fit to a purely thermal or a bimodal distribution. This is generally done subjectively as we have not yet devised a robust algorithm for automatically determining a bimodal distribution and the interface between thermal and condensed gases.
- For thermal distributions the 2D data file is passed to a nonlinear least squares algorithm which fits Eq. 2.16 to the experimental data.

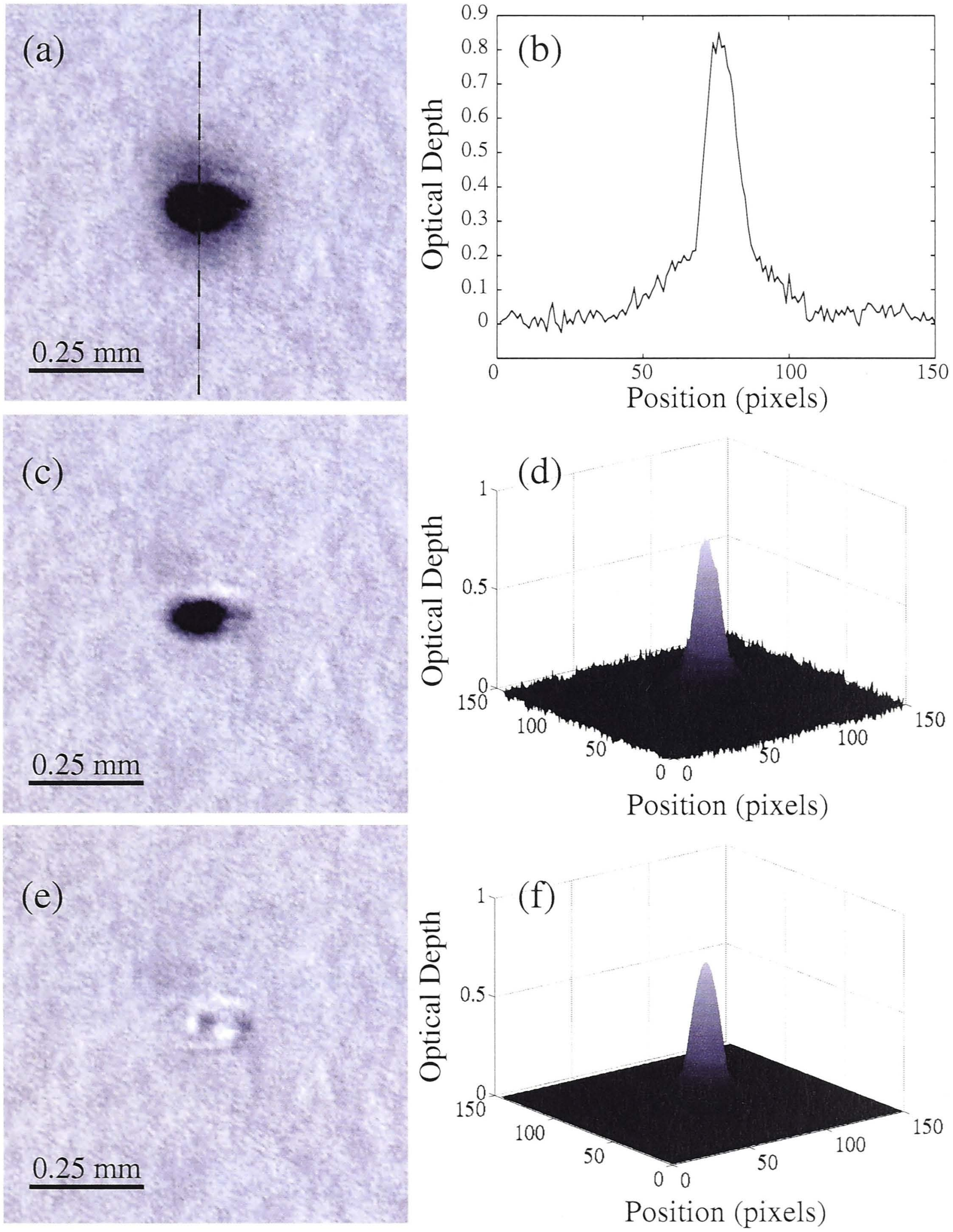

Figure 3.18: Illustration of the steps taken in the fitting algorithm. (a) Experimental image of a partially condensed cloud of 5×10^4 atoms. (b) 1D slice through the data along the z-axis (vertical dashed line in (a)) - this image is used to determine the interface between condensate and thermal cloud. (c) The theoretical surface fitted to the thermal distribution has been subtracted from the experimental data leaving a pure condensate. (d) the residual after the data of (c) is fitted to a condensate distribution and the theoretical surface subtracted from the experimental data. (e) Surface plot of the experimental data. (f) Surface plot of the fitted theoretical bimodal distribution.

- For bimodal distributions the wings of the distribution (defined as being well outside the central high density region) are fitted to Eq. 2.16 and the temperature along each axis is calculated according to Eq. 2.18 . Fitting the wings to Eq. 3.8 gives the same results - as pointed out by in [53] all such thermal distributions decay as a Gaussian.

- The fitted surface is subtracted from the distribution and the remaining 2D data is fit by Eq. 3.9

The analysis is not sufficiently fast to adjust experimental parameters of consecutive runs, but does allow the experimental data to be analysed as the next run of the experiment is taking place.

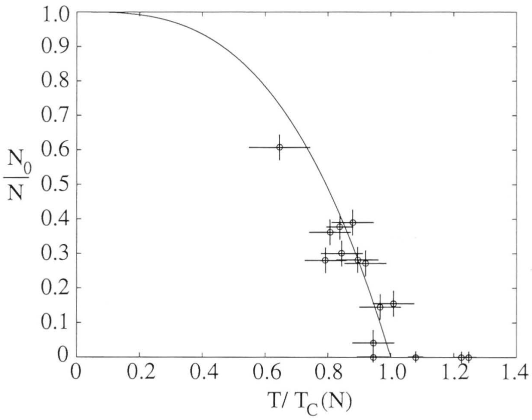

Figure 3.19: The ratio of Bose condensed to the total number of atoms. Each data point represents the average of up to five runs of the experiment. Solid line represents the theory calculated from Equation 3.10.

3.12 Bose-Einstein condensation

Given a large number of atoms in the magnetic trap and a clear indication that the system has achieved runaway evaporative cooling with the observation of steady or increasing optical depth as the cloud is cooled [138], then it is almost certain that BEC will be achieved. There are a number of clear signatures of BEC one expects to observe:

- Signature 1. The sudden onset of a steadily growing high density region in the centre of the cold cloud.

- Signature 2. A clear bimodal structure for partially condensed clouds.

- Signature 3. An anisotropic expansion of the cold cloud.

Our data shows both qualitative and quantitative evidence of BEC, as seen in our images of the cold clouds and based on our calculations of temperature and number of atoms, respectively. Each of the listed signatures is addressed in the following sections. At the end of an evaporative cooling run, the atoms are held in the magnetic trap for 100 ms (no RF shield), and then the trap is switched off. The atomic cloud is accelerated by gravity and expands as it falls. After a delay of typically 20 ms, an absorption image of the cloud is taken, followed closely (1 second later) by a 'bright field' image of the imaging laser. After a small amount of data processing (as described in section 3.8), we produce an image of the optical depth, $\emptyset$, of the expanded cloud. Further analysis as described in the previous section (3.11), produces quantitative atom numbers, temperatures and chemical potentials for the observed atomic clouds.

3.12.1 Sudden increase in optical depth

By substituting Eq. 2.14 into Eq. 2.13 one arrives at an expression, valid when $T < T_c$, for the ratio of condensed atoms (i.e. number of atoms in the ground state) to total number of atoms as a function of temperature:

$$\frac{N_0}{N} = 1 - \left(\frac{T}{T_c}\right)^3 \tag{3.10}$$

where T_c is given by Eq. 2.14. Thus, the number of atoms in the condensate grows quickly as the kinetic temperature of the atoms drops below T_c. An expansion image of a partially condensed cloud will show a dense 'core' of condensate atoms surrounded by a diffuse thermal cloud. The ratio of this dense core of atoms to the total number of atoms is plotted in Figure 3.19 from our experimental data and compared with the prediction of Eq. 3.10. In Figure 3.22, we show a series of absorption images of the condensate formation showing the apearance of the optically dense 'core' as the temperature is decreased.

3.12.2 Bimodal distribution

In the limits of high and low temperature, the atomic density is well characterised by a Gaussian or Thomas-Fermi (TF) distribution, respectively. However, as discussed in section 2.6.2, partially condensed clouds are composed of a mixture of condensate and thermal atoms and therefore exhibit two significantly different density distributions. A clear bimodal distribution is thus an excellent indicator of the presence of a condensate. Figure 3.20 shows a slice through our data displaying a very clear bimodal distribution.

3.12.3 Anisotropic expansion

An interesting feature of anisotropic magnetic traps is that the condensate should have a higher interaction energy in the tight trapping direction (ω_ρ) than the weak (ω_z). An anisotropic expansion of the condensed cloud is a convincing indication

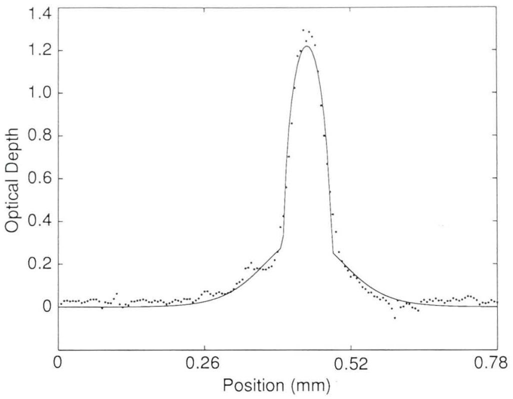

Figure 3.20: Bimodal distribution of a partially condensed cloud. A 1D slice of the experimental column density along the z-axis of the condensate (Dots). The solid line is a 1D slice through the theoretical surface fitted to the data as described in section 3.11.

that the interaction energy of the cloud is significantly higher than its (thermal) kinetic energy, thus demonstrating the existence of the mean field and a single macroscopic wavefunction. Using the time dependent GP equation to model the condensate expansion after its release from the trap, it can be shown [139, 22] that the aspect ratio R_ρ/R_z of the condensate during an expansion should be well described by

$$R_\rho/R_z = \lambda\frac{\sqrt{1+\tau^2}}{1+\lambda^2(\tau\arctan\tau - \ln\sqrt{1+\tau^2})} \tag{3.11}$$

where $\lambda = \omega_z/\omega_\rho$ and $\tau = \omega_\rho t$. This equation predicts a reversal of the condensate aspect ratio as the condensate expands. The demonstration of this effect is shown in Figure 3.21.

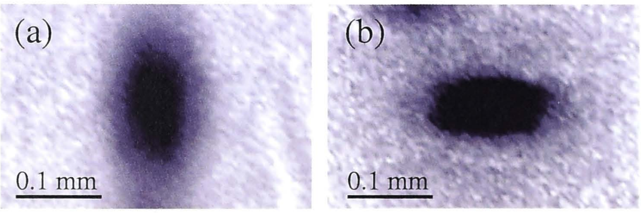

Figure 3.21: Anisotropic expansion of the condensate. Absorption images of (a) 5 ms expansion, and (b) 25 ms expansion. The aspect ratio of the condensate has reversed. The weak z-axis of the magnetic trap is along the horizontal in both images. In figure (a) the condensate appear larger than it actually is, due to complete absorption of the probe laser [54]

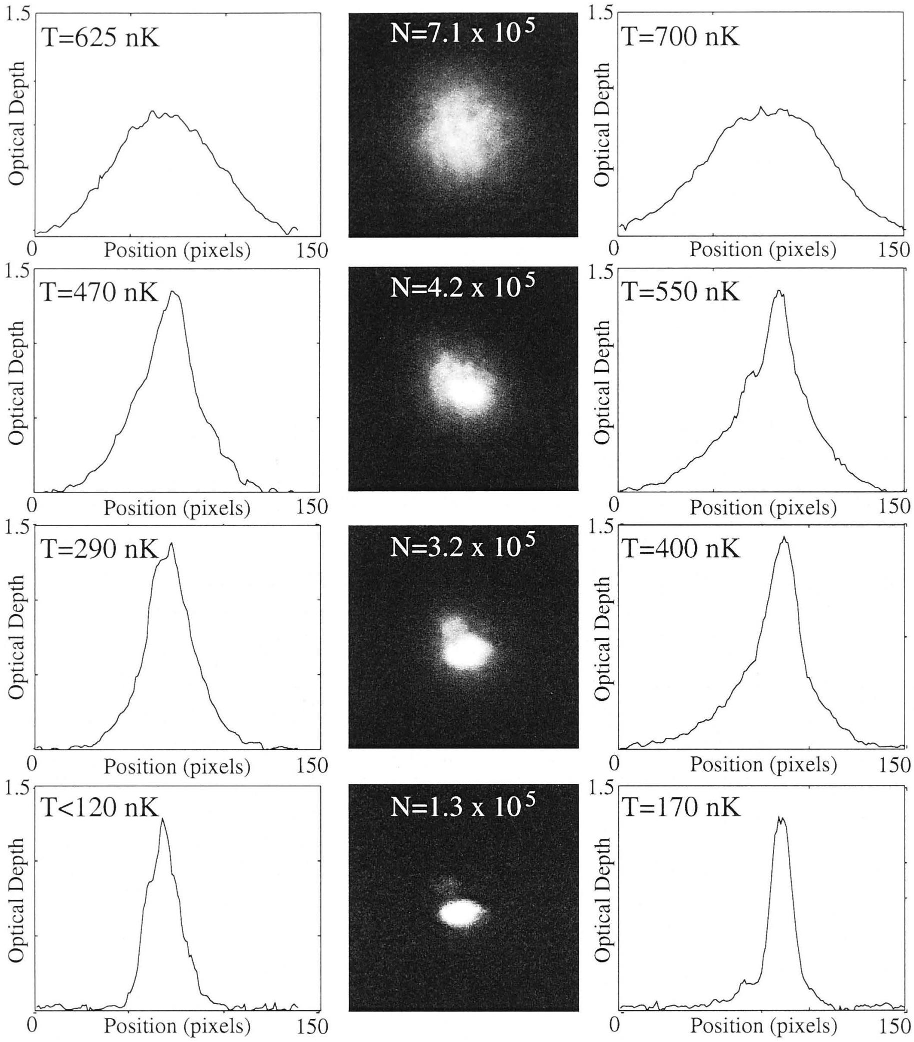

Figure 3.22: Experimental demonstration of BEC via a sudden increase in optical depth at the centre of the cold cloud. Four images taken after a 17 ms expansion, in consecutive runs of the experiment as the final RF evaporation frequency is lowered in steps of 7.5 kHz. The central sequence shows the experimental column density and total number of atoms in the image. On the left of the figure, a 1D slice through the centre of the cloud along the horizontal axis of the data is shown with the calculated temperature in this direction (corresponding to the axis of tight confinement). On the right, a similar slice through the centre of the cloud in the vertical direction (corresponding to the z-axis of the trap) is shown with the calculated temperature in this direction. Each pixel represents $\sim 5\,\mu m$. We have no explanation for the small difference in temperatures between axial and radial directions. This effect has been observed by other groups and some tentative explanation is given in Kai Deickmanns thesis ??.

CHAPTER 4

The atom laser

A simple pulsed atom laser can be produced by switching off the magnetic trap confining a BEC. In this case, a pure spin state 'pulse' of atoms falls under gravity. The pulse ballistically expands according to Eq. 3.11 of the previous chapter, and evolves into a pancake shaped cloud. Atom optics experiments on atom lasers of this sort have been performed including reflection from a repulsive potential known as the dramatic 'bouncing BEC' [140]. If more control of the number of atoms in a pulse or the duty cycle of the pulses (which is limited in the previous case to the duty cycle of the entire experiment) is needed, another method for producing an atom laser must be employed. Indeed, apart from the fact that many conceivable applications require a continuous beam of atoms, a 'true' atom laser must fulfill the requirements laid out in Chapter 1. Following the optical laser analogy introduced in Chapter 1, we distinguish between a truly continuous and quasi-continous atom laser. It is now generally accepted that to make a continuous atom laser a condensate should be continuously replenished by a cold atomic source and depleted in a controlled manner to form a beam (an alternative is to Bose-condense in a waveguide [65, 66, 67]). In this chapter, we focus on a quasi-continuous atom laser produced with radio frequency (RF) transitions.

A number of one-and two-photon methods exist for the coherent transfer of atoms from one internal atomic state to another, among them optical atomic Bragg diffraction or Raman coupling [141, 142, 4], microwave transitions between hyperfine ground states [143], and radio-frequency (RF) transitions between Zeeman states [3]. Of these techniques, RF and Raman have been demonstrated as output couplers. Theoretically it should be possible for these methods to produce highly controlled pulsed or continuous output coupling, however to date continuous coupling has been achieved only by using RF transitions [5, 116, 105].

Both temporal and spatial coherence of the atom laser have been measured, and it has been demonstrated that RF outcoupling preserves the coherence of the condensate [115, 10]. The beam divergence has been measured [116], and there has been one real time measurement of the flux of an atom laser beam [7]. Rabi cycling between Zeeman components, a manifestation of the non-Markovian nature of the atom laser [113, 114], was observed in the experiment of Mewes *et al.* and could be expected to significantly increase the amplitude, and possibly frequency, noise of the beam. There has been no investigation of the relationship between classical

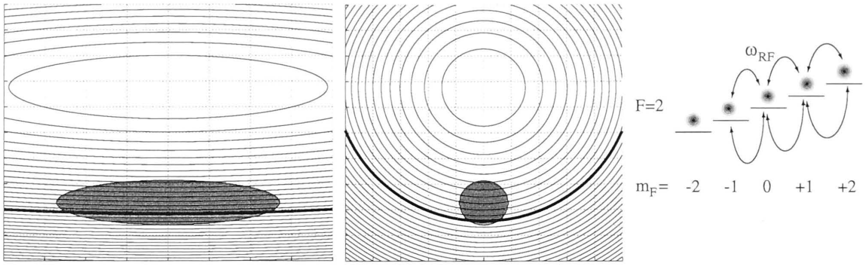

Figure 4.1: Schematics of RF output coupling. The left hand image views the condensate perpendicular to the weak trapping axis, while the middle image is a view along that axis. The contour lines represent absolute value of the magnetic field. The right hand image represents the coupling between Zeeman states of the F=2 ground state.

noise and flux in an atom laser, and, in the later part of this chapter, this aspect of atom laser output coupling is investigated both experimentally and theoretically.

4.1 Output coupling

A radio frequency output coupler uses the resonance between non-degenerate Zeeman states in the small bias field at the minimum of the magnetic trap. In our trap, the bias is around 1 G corresponding to a uniform splitting between Zeeman states of $v = 0.7$ MHz. Applying a monochromatic radio frequency magnetic field resonant with this splitting coherently couples atoms between Zeeman states (right image of figure 4.1). The magnetically trapped $F = 2, m_F = 2$ atoms can then be 'shunted' through the $F = 2, m_F = 1$ state to the $F = 2, m_F = 0$ state in which they no longer interact with the magnetic potential. Recall from Chapter 2 that the presence of the trapping magnetic field also introduces a spatial resonance associated with a given frequency allowing the centre of the resonance to be tuned within and around the condensate. The resonance condition is satisfied on the surface of an ellipsoid centred around the minimum of the magnetic field (left and middle images of figure 4.1). Gravity introduces an asymmetry such that the minimum of the *trapping potential* given by $\frac{1}{2}M\omega_\rho^2\rho^2$ is shifted down vertically by $G_{shift} = g/\omega_\rho^2$ from the centre of the magnetic field minimum. For our trapping frequency of $\omega_\rho = 2\pi \times 253Hz$, this corresponds to a shift of $G_{shift} = 3.9\mu m$. This asymmetry produces a 'preferred' direction of the coupling process, and the atoms fall out of the trapping region.

4.1.1 The resonant width of the condensate

Within the Thomas-Fermi (TF) approximation, the spatial extent of the condensate in the direction of gravity is $2R_{TF} = 2\sqrt{\frac{2\mu}{M\omega_\rho^2}}$, which for a typical chemical potential of $\mu = 1 \times 10^{-30}J$ is $2R_{TF} = 4.7\mu m$.

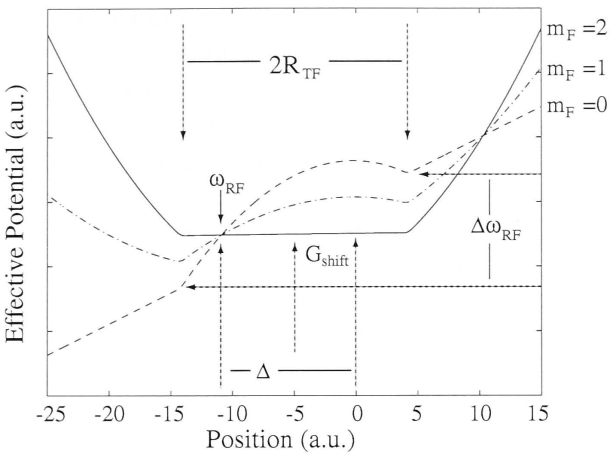

Figure 4.2: The effective potentials experienced by each of the three Zeeman states with the critical physical parameters indicated. Surfaces calculated using a one dimensional version of the model system of Eq. 4.2

Because the BEC sags in the magnetic trap into regions of higher magnetic field gradient, the resonant frequency width of the condensate is larger than its bare width given by μ/h. The resonant width is found by considering the difference in resonant frequencies between the lower edge of the condensate at $x_l = g/\omega_\rho^2 + R_{TF}$ and the upper edge at $x_u = g/\omega_\rho^2 - R_{TF}$. The magnetic field at any point in the vertical direction is given by $B = B_0 + 1/2B''_\rho\rho^2$ where $B''_\rho = \frac{M\omega_\rho^2}{g_F m_F \mu_B}$, and the resonant frequency is $\omega_{RF} = g_F\mu_B B/\hbar$. Thus the resonant width for the $|F = 2, m_F = 2\rangle$ state is given by

$$\Delta\omega_{RF} = \frac{M\omega_\rho^2}{2\hbar m_F}(x_l^2 - x_u^2) = \frac{g}{\hbar\omega_\rho}\sqrt{2M\mu} \sim \left(\frac{\omega_z}{\omega_\rho^3}\right)^{\frac{1}{5}}. \tag{4.1}$$

For our current trap and condensate size $\Delta\nu = 5kHz$, more than three times the bare width of the condensate. The lower limit on the width of the RF resonance itself is straightforwardly calculated as $\delta\omega_{RF} = 4\pi/\tau$ where τ is the radio-frequency output coupling duration [144]. For short output coupling times, $\delta\omega_{RF}$, can be significantly larger than the resonant width of the condensate, $\Delta\omega_{RF}$. Finally the detuning from the centre of the magnetic field is given by the difference between the outcoupling frequency and the frequency coinciding with the magnetic field minimum, $\hbar\Delta = \hbar\omega_{RF} - g_F\mu_B B_0$. Figure 4.2 shows the relationships between each of the principle quantities characterising RF output coupling.

4.2 The model

Further discussion of the atom laser system requires a model of the output coupling process. Ballagh et. al. [145] introduced the Gross-Pitaevksii equation as an effective tool for investigating the atom laser within the semi-classical mean-field approximation. A number of groups have found good agreement between theory and experiment [146, 147], using mean field models of the atom laser. The Gross-Pitaevskii theory of the atom laser derived for the full 3D dynamics of the $F = 2$ manifold of ${}^{87}Rb$ is described in an interaction picture by the following equations [148]

$$\begin{aligned}
i\dot{\phi}_2 &= (\mathcal{L} + V_T + Gy - 2\Delta)\phi_2 + 2\Omega\phi_1 \\
i\dot{\phi}_1 &= (\mathcal{L} + \frac{1}{2}V_T + Gy - \Delta)\phi_1 + 2\Omega\phi_2 + \sqrt{6}\Omega\phi_0 \\
i\dot{\phi}_0 &= (\mathcal{L} + Gy)\phi_0 + \sqrt{6}\Omega\phi_1 + \sqrt{6}\Omega\phi_{-1} \\
i\dot{\phi}_{-1} &= (\mathcal{L} - \frac{1}{2}V_T + Gy + \Delta)\phi_{-1} + 2\Omega\phi_{-2} + \sqrt{6}\Omega\phi_0 \\
i\dot{\phi}_{-2} &= (\mathcal{L} - V_T + Gy + 2\Delta)\phi_{-2} + 2\Omega\phi_{-1}\,,
\end{aligned} \tag{4.2}$$

where ϕ_i is the GP function for the ith Zeeman state. $V_T = \lambda^2(x^2 + y^2) + z^2$ is the trapping potential, and $\mathcal{L} \equiv -\frac{1}{2}\nabla^2 + U(\Sigma_{i=-2}^{2}|\phi_i|^2)$. Here $\lambda = \frac{\omega_r}{\omega_z}$ is the ratio of trapping frequencies ($\lambda = 12.65$ for the magnetic trap described in this thesis), Δ and Ω are respectively the detuning of the RF field from the B_0 resonance, and the Rabi frequency, measured in units of ω_z, U is the interaction coefficient and $G = \frac{mg}{\hbar\omega_z}(\frac{\hbar}{m\omega_z})^{1/2}$ gravity. The wave functions, time, spatial coordinates, and interaction strengths are measured in the units of $(\hbar/m\omega_z)^{-3/4}$, ω_z^{-1}, $(\hbar/m\omega_z)^{1/2}$, and $(\hbar\omega_z)^{-1}(\hbar/m\omega_z)^{-3/2}$, respectively, where ω_z is the axial (weak) trapping frequency.

These equations will be used in subsequent sections to model both temporal and spatial dynamics of the condensate components in the atom laser reserviour and atom laser output (state ϕ_0). As an initial condition for our simulations, we use the exact numerical solution to the time-independent GP equation for our trapping parameters and condensate atom number, found by either imaginary time propagation (3D) or the relaxation method (1D) [149]. The time-independent GP equation can be found from Eq. 4.2 using the substitution $\phi_2(\mathbf{r}, t) = \varphi(\mathbf{r})e^{i\mu t}$.

4.2.1 Transforming to lower dimensions

Numerical descriptions of an atom laser within the mean-field frame work are complicated by the large velocities that atoms reach when falling in a gravitational potential (see appendix B.2.3). The resultant small de-Broglie wavelengths require very fine temporal and spatial numerical grids in order to accurately follow the dynamics. Additionally, to run simulations that reflect experiments on a time scale longer than a few milliseconds, an apodising mechanism must be introduced to absorb the beam and hence avoid breakdown of the numerical techniques used. These factors make simulating and understanding atom laser dynamics a complicated proposition. In order to simplify the numerics, the 3D system can be rigorously transformed to lower dimensions. Because of the anisotropic nature of the trapping potential, the cigar shaped BEC is assumed to be quasi-one-dimensional and hence we use the ansatz $\phi_j(\mathbf{r}, t) = \Psi(x, y)\phi_j(z, t)$, where z is the direction of weak confinement, and $\Psi(x, y)$ is the wavefunction of the two-dimensional harmonic oscillator potential. The dimensionless interaction coefficients are then $U_{1D} = U_{3D}\alpha$, where $\alpha = \int |\Psi(x,y)|^4 dxdy / \int |\Psi(x,y)|^2 dxdy$ is the transverse structure factor. For simulations of the atom laser, most of the dynamics occur in the direction of gravity, perpendicular to the weak trapping axis. In order to create a model in one of the transverse directions, an ansatz of the form $\phi_j(\mathbf{r},t) = \Psi(x)\Phi(y)\phi_j(z,t)$ can be used in which $\Phi(y)$ is the TF (or exact numerical) solution along the weak trapping direction.

Alternatively, the dimensionality reduction can be performed *non rigorously* by writing an equivalent equation for the system in the dimension(s) of interest [148]. The nonlinear interaction strengths are derived in this situation by requiring that the 1D (2D) TF chemical potential be equivalent to the 3D case.

4.3 The Rabi frequency

The dynamics of either a pulsed or quasi-continuous atom laser are determined by the interaction between a number of fundamental time and length scales of the problem. The first important timescale is the inverse of the Rabi frequency, $\tau_R = 2\pi\Omega^{-1}$. It can be seen from Eq. 4.2 that the coupling occurs only between adjacent Zeeman states, mediated by the effective Rabi frequency (in physical units):

$$\Omega = \frac{g_F \mu_B B_{RF}}{2\hbar} \tag{4.3}$$

where B_{RF} is the magnitude of the driving magnetic field. For a driving field of 30 mG the effective Rabi frequency is $\Omega = 66kHz$ giving $\tau_R \approx 0.1ms$. The Rabi frequency also represents the *power broadened* width of the output coupling resonance [150].

The second major time scale is the time is takes the atoms to fall out of the RF resonance due to gravity. In order to calculate this, we need to relate the spatial width, $\delta\rho_{RF}$, of the RF output coupling resonance to its frequency width, $\delta\omega_{RF}$. Assuming that the resonance is centred on the condensate and using Eq. 4.1, the frequency width of the RF resonance is

$$\delta\omega_{RF} = \frac{M\omega_\rho^2}{2\hbar m_F}\left(\left(\frac{g}{\omega_\rho^2} + \frac{\delta\rho_{RF}}{2}\right)^2 - \left(\frac{g}{\omega_\rho^2} - \frac{\delta\rho_{RF}}{2}\right)^2\right) = \frac{Mg\delta\rho_{RF}}{\hbar m_F} \tag{4.4}$$

The frequency width of the RF resonance is determined from the larger of either, the 'pure' RF resonance, $\delta\omega_{RF} = 4\pi/\tau$, or the power broadened width given by the Rabi frequency, Ω. Rearranging Eq. 4.4 we find the *spatial* extent of the RF resonance is

$$\begin{aligned} \delta\rho_{RF} &= \frac{4\pi\hbar m_F}{Mg\tau}, \qquad if \quad \delta\omega_{RF} > \Omega \\ \delta\rho_{RF} &= \frac{2\hbar m_F \Omega}{Mg}, \qquad if \quad \delta\omega_{RF} < \Omega \end{aligned} \tag{4.5}$$

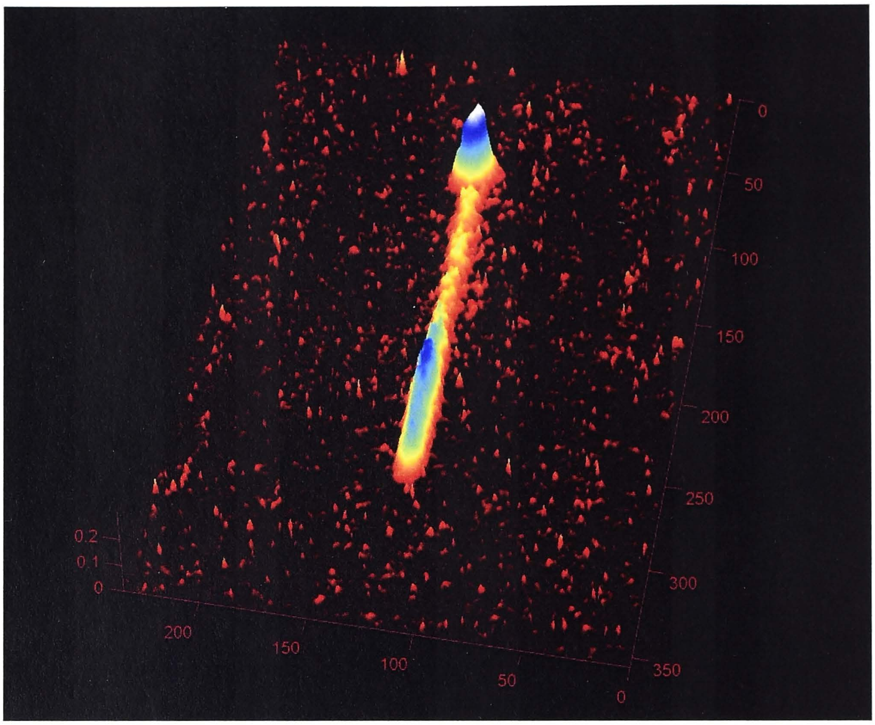

Figure 4.3: A quasi-continuous atom laser produced in the weak coupling regime. Total number of atoms in the image is about 1×10^5. Output coupling time was 12ms at a peak-to-peak magnetic field strength of 0.8mG. The detuning was set to $\Delta = 2\pi \times 2kHz$. Spatial axes are in pixels and vertical axis is optical depth.

Thus, the time taken for an atom to fall across the entire resonant width of the output coupling pulse is

$$\begin{aligned} \tau_{fall} &= \frac{1}{g}\sqrt{\frac{8\pi\hbar m_F}{M\tau}} \qquad for \quad \delta\omega_{RF} > \Omega \\ \tau_{fall} &= \frac{1}{g}\sqrt{\frac{4\hbar m_F \Omega}{M}} \qquad for \quad \delta\omega_{RF} < \Omega \end{aligned} \tag{4.6}$$

For a 30 mG, $10\mu s$ pulse this time is 3 ms, while for a 1 mG, 20 ms pulse it is 0.5 ms.

In the limit that the coupling region is narrower than the condensate, the timescale in which atoms will flow *into* the coupling region from the rest of the condensate may also become important. It is given by the healing time of the condensate and can be estimated in the TF approximation as $\tau_\xi = \xi/c = \frac{\hbar}{\sqrt{2}\mu}$ where $\xi = (8\pi n a)^{-\frac{1}{2}}$ is the healing length, and $c = (U_{3D}n/m)^{\frac{1}{2}}$ is the speed of sound in a BEC of density n [22]. For our parameters, the healing time at the centre of the

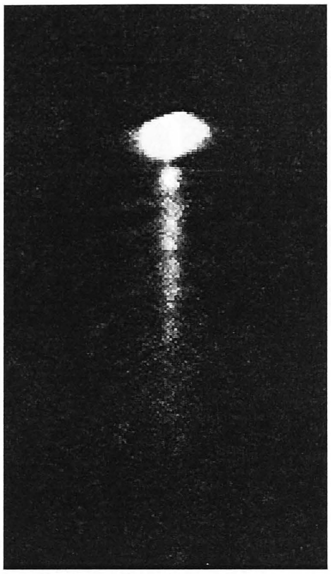

Figure 4.4: Pulsed atom laser in the strong coupling regime. Twenty $10\mu s$ pulses have been applied to the condensate at a pulse rate of 2.5 kHz. The peak-to-peak magnetic field strength is 33 mG.

condensate is $\tau_\xi \approx 0.07ms$. Generally, for weak RF output coupling τ_ξ will always be the shortest timescale in the problem, however for Raman-type output coupling (see section 2.8.1) this time scale becomes important.

We are now in a position to define a number of regimes of operation of the atom laser. We define the *weak output coupling regime* by the two conditions $\delta\omega_{RF} < \Delta\omega_{RF}$ and $\tau_R \gg \tau_{fall}$. We therefore require primarily, that the width of output coupling resonance is smaller than the condensate, and secondly, that the atoms fall from the coupling region on a timescale much less than the effective Rabi coupling time, τ_R. For our trap and condensate sizes, these conditions translate into $B_{RF} \ll$ 2.6 mG and $\tau > 400$ μs, where τ is the output coupling pulse time. These conditions are easily achieved experimentally using small field strengths and long coupling times and an experimental realisation of an atom laser operating in this regime is shown in figure 4.3. A more stringent criterion suggested by Steck et al [146] also requires that $\Omega \ll \omega_\rho$ (i.e. that $B_{RF} \ll 0.7mG$). However, this condition was derived in the absence of a gravitational field.

The regime of strong output coupling occurs when atoms make many Rabi oscillations before leaving the coupling region, expressed simply as $\delta\omega_{RF} \geqslant \Delta\omega_{RF}$ and $\tau_R \ll \tau_{fall}$. For short pulses and our trap, these conditions are $B_{RF} > 10mG$ and $\tau \ll 400$ This regime is also easily accessible experimentally and an example of a multiple pulse atom laser, in the strong coupling regime, is shown in figure 4.4.

Experimentally, a quasi-continuous atom laser based on resonant output coupling puts stringent limits on the stability of cold atom traps [5]. Typical condensates have a resonant width of about 5-10 kHz. Well defined continuous output

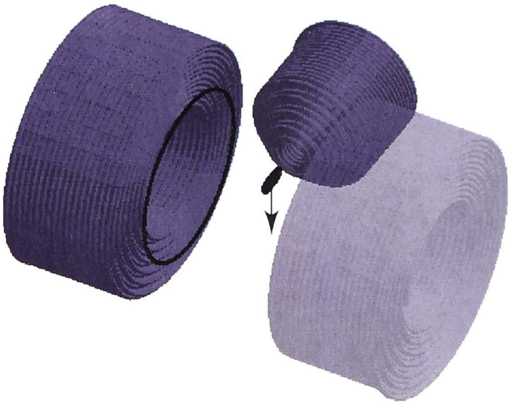

Figure 4.5: Schematic of the atom laser system. The cylindrical shaped condensate is oriented along the Ioffe (small) coil axis. The RF coil is perpendicular to the long axis of the condensate, in line with the quadrupole coils. The condensate is imaged directly through the quadrupole coils.

coupling requires a stable magnetic bias, B_0, at the 0.1 mG level, one to two orders of magnitude better than typical magnetic traps. In comparison, a pulsed atom laser is relatively straightforward to implement. A 10μs pulse has a frequency width of 200 kHz, significantly broader than both the 5 kHz resonant width of the condensate, and the instability of the trap which fluctuates within the range ±15 kHz over a number of hours due mainly to thermal fluctuations of the coils.

4.4 Production of a pulsed atom laser

In this experiment, we produce an $F = 2, m_F = 2$ ^{87}Rb condensate, consisting of approximately 50,000 atoms, via evaporation in a water-cooled QUIC magnetic trap [97] with a radial trapping frequency $\nu_r = 253$ Hz, an axial trapping frequency $\nu_z = 20$ Hz, and a bias field $B_0 = 1$ G. The QUIC trap is ideally suited to atom laser studies as it can be run at extremely low current, and when optimised (as discussed in Chapter 6) has the potential to form tight traps while dissipating less than 50 W, thus generating extremely stable magnetic potentials without the restrictions of active cooling systems. The general geometry of the trap is presented in figure 4.5. After evaporative cooling the BEC is left to equilibrate, both thermally and motionally, for 100 ms. We then apply a TTL initialization signal to a pulse generator which is used to drive the TTL input of an RF signal generator (Agilent) set in gated burst mode (max 7 dBm). The RF pulses are amplified (35 dB) and radiated perpendicular to the magnetic bias field of the trap through a 22 mm radius single loop, approximately 18 mm from the BEC. To ensure that all experimental parameters had been calibrated correctly, an initial series of measurements were

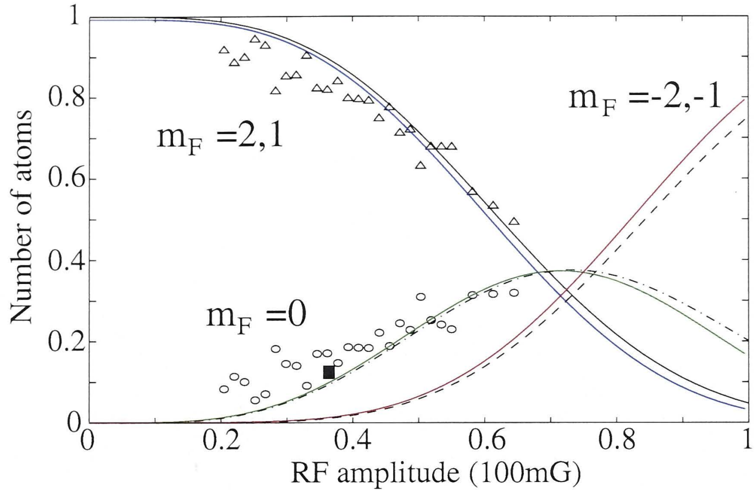

Figure 4.6: Outcoupled fraction as a function of RF amplitude. The solid square is the RF amplitude at which the results of Fig.4.7 were generated. Theoretical curves generated by the author are: Solid line, $m_F = 2, 1$ trapped states, dot-dashed $m_F = 0$ and dashed, $m_F = -2, -1$ anti-trapped states. The experimental results are: triangles, $m_F = 2, 1$ trapped states, circles $m_F = 0$. Typical error bars are ±5% vertically and ±10% horizontally. Simulation parameter: $\Delta = -640$. The coloured lines represent a numerical simulation of the experiment from a single particle rate equation model of the five level system **generated by Simon Haine** [100].

made of the number of trapped and un-trapped atoms after the application of single RF pulses of varying amplitude. It was critical to establish agreement between experiment and theory in a simple mode of operation before pursuing studies of more complex dynamics. To calculate the RF amplitude, and hence the Rabi frequency, of the experimental data we used the peak voltage of the RF signal after the amplifier into the internal impedance of the amp (50 Ω) to give the maximum current in the coil. From this we used the equations for the off-axis field of a single current loop to calculate the local RF magnetic field at the BEC. For the experiment described hereafter we selected an RF amplitude that coupled only a very small fraction of atoms into the anti-trapped states while giving a large enough number in the $m_F = 0$ state for a good signal to noise ratio. In Fig. 4.6, we show the results of these measurements in comparison with a numerical calculation employing a *one dimensional* model obtained by rigorous dimensionality reduction of Eq. 4.2. The excellent agreement between experiment and theory shown in Fig.4.6 indicates that we have a well calibrated and repeatable experiment. Up to the experimental uncertainty in the detuning Δ, there are no free parameters in the 1D GP model. The theoretical results of the Rabi oscillations presented in Fig. 4.6 are in good agreement with the approximate analytic theory presented by Graham and Walls for the limit of strong out-coupling [151].

4.5 Classical noise and flux: the limits of multi-state atom lasers

This section shows, using a direct comparison between experiment and theory, that the classical noise on a multi-state atom laser beam increases with increasing flux. The trade off between classical noise and flux will be an important consideration in future precision interferometric measurement utilizing atom lasers.

It is the high flux, spectral density, and associated first order coherence that has made the optical laser central to many technologies. In the field of precision measurement, atom lasers hold similar promise [8, 109, 152]. In a Sagnac interferometer, for example, the inherent sensitivity of a matter wave gyroscope exceeds that of a photon gyroscope with the same particle flux and area by 11 orders of magnitude [153]. In any practical application of interferometry to high precision measurement, whether it be with photons or atoms, there will be a trade off between the classical noise (due to the presence of unwanted excited dynamic modes) and the quantum noise or flux of the source. In this section, we investigate this trade off for an atom laser.

We use periodic 10μs radio-frequency pulses to couple atoms out of an $F = 2, m_F = 2$ ^{87}Rb Bose-Einstein condensate. The resulting atom laser beam has suprising structure which is explained using three dimensional simulations of the five state Gross-Pitaevskii equations (Eq. 4.2). The agreement between our experimental results and a full 3D Gross-Pitaevskii (GP) model is significant. It is highly likely that the much sought-after pumped atom laser will operate under rather specific conditions of scattering length, temperature and number density [154, 155]. Future work will need to be guided by accurate theoretical models that must be validated against experiments if we are to trust their detailed predictions. We have opted to study a pulsed atom laser to ensure shot to shot reproducibility and allow detailed quantitative comparison to numerical models. We have chosen to study atom laser beams derived from an $F = 2, m_F = 2$ condensate because of the richness and complexity offered by the system, although non-Markovian effects are present even in two-component atom lasers due to the nonlinear atomic dispersion relations.

4.5.1 Experimental results

In the experimental data shown in Fig.4.7, we present five pulse trains outcoupled from separate F=2, $m_F = 2$ condensates. In each case, the pulse train has been outcoupled in an 8 ms time frame. We wait 2 ms after the pulse window before turning the trap off to allow the final atomic pulse to completely separate from the condensate. After a further 2 ms, to allow expansion of the condensate, we image the condensate and pulses with a single lens onto a 12 bit CCD camera. For one, two (see figure 4.8), three and four RF pulses, we observe predictable outcoupling from the atom laser system. Figure 4.7(a) is indicative of this behaviour, where four RF pulses (separation 2 ms) have been applied to the BEC, and we see four $m_F = 0$ atomic pulses in the positions expected from gravity. In 4.7(b) five

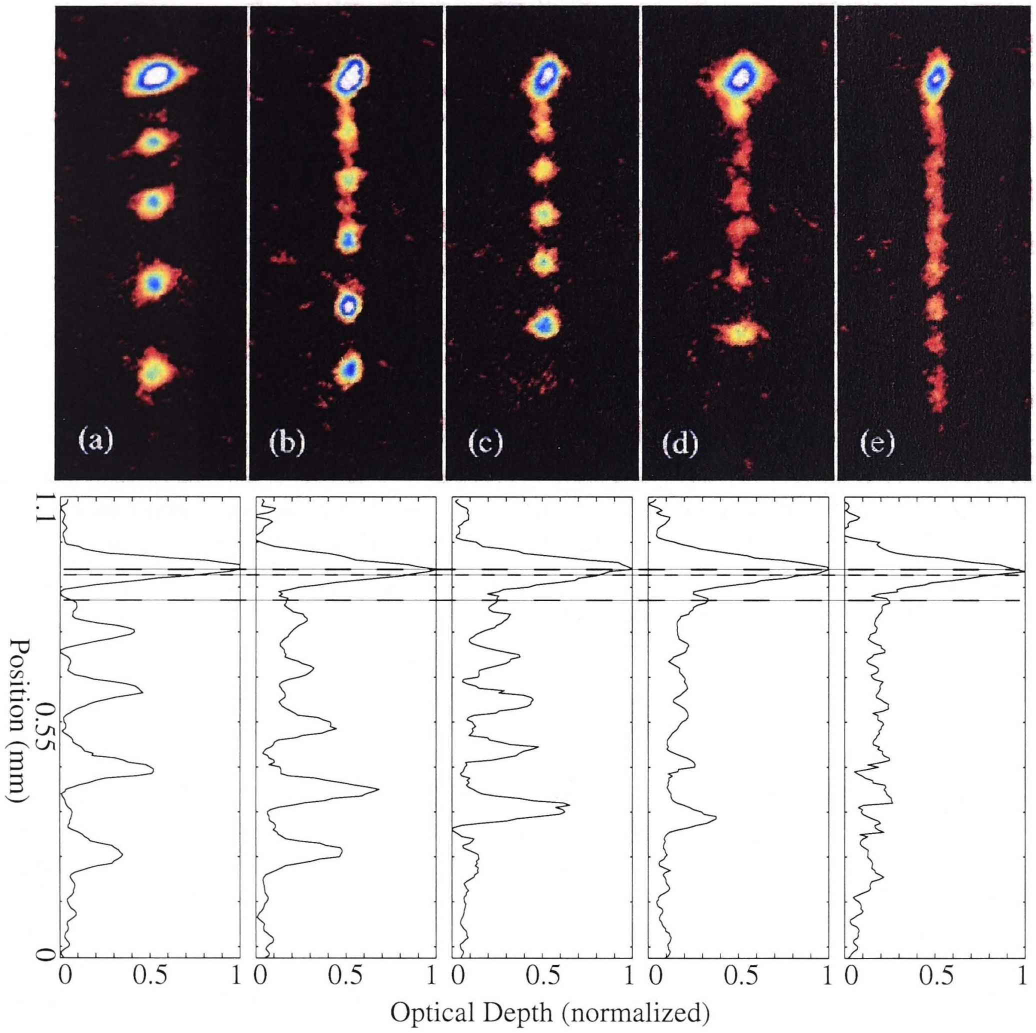

Figure 4.7: (color) A series of pulsed atom lasers at different pulse rates. The number of applied radio-frequency (RF) pulses are varied from (a) 4, (b) 5, (c) 6, (d) 7, and (e) 10 pulses in an 8 ms window. The lower plots show a cross-section down the centre of the absorption data. The three dashed lines correspond, in descending order, to the centre of the condensate, the half-width of the 200 kHz RF resonance (100 kHz $\approx 12\mu$ m in our trap) and the position coinciding with the final RF out-coupling pulse (4 ms prior to imaging).

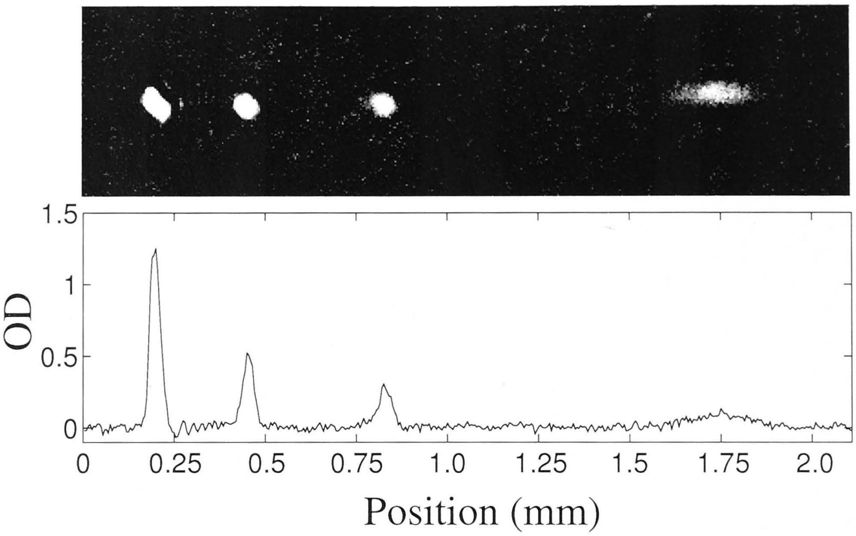

Figure 4.8: A two-pulse atom laser in the strong coupling regime. Two $10\mu s$ output coupling pulses have been applied to the condensate at a pulse rate of 250 Hz. The peak-to-peak magnetic field strength is 33 mG. Gravity is to the right. The diffuse pulse on the right-hand side of the image corresponds to an anti-trapped state.

RF pulses (separation 1.6 ms) have been applied and we observe five atomic wavepackets, again in the expected positions. However, we note that in the later 3 pulses there is a significant blurring with atoms appearing between the expected positions of the pulses. This effect is not due to interference between the wavepackets. The transition from constant pulse amplitude shown in Fig.4.7(a) to varying or noisy pulse amplitude with increasing repetition rate shows a clear trade off between classical noise and flux in the atom laser output. In Fig.4.7(c) six RF pulses were applied (separation 1.2 ms), however only five atomic pulses were observed, with the first atomic pulse being entirely absent. This observation is quite repeatable. The complete absence of a pulse is an extreme example of the trade off between classical noise and flux, and it is the dynamics behind this phenomenon that we wished to understand by comparison with a complete 3D GP model. At the higher pulse repetition rate used in Fig.4.7(d) where the separation between pulses is 1 ms, the output is further distorted from the ideal. In Fig.4.7(e), where the time between pulses has been reduced to 800μs, the atom laser beam is longer than expected from pure gravitational acceleration. This can be explained by the influence of the the anti-trapped m_F states on the $m_F = 0$ atoms that comprise the outcoupled beam. The full image of this situation is shown in Fig. 4.9. It is quite clear from the data that increasing flux (and therefore decreasing shot noise) comes at the price of increasing classical noise.

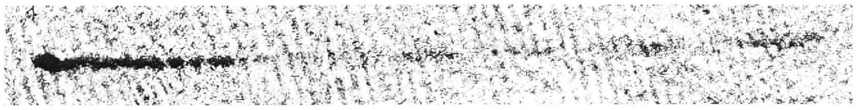

Figure 4.9: A ten pulse atom laser in the strong coupling regime. Ten $10\mu s$ output coupling pulses have been applied to the condensate at a pulse rate of 1.25 kHz. The peak-to-peak magnetic field strength is 33mG. The dark beam corresponds to atoms falling under gravity (~ 0.7 mm long). The anti-trapped Zeeman states that contribute significantly to the atom laser dynamics can be seen faintly on the right hand side of the image. Gravity is to the right.

4.5.2 Theoretical results

To understand the experimental results described in the previous section, the experiment has been quantitatively modelled with a full 3D GP simulation including all five Zeeman states and with only the detuning Δ as a free parameter (Eq. 4.2). The simulations were performed by Dr. Craig Savage with the active participation of the author in interpreting the numerical results. This full 3D simulations are a unique feature of the work presented here and allow us to understand all aspects of the experiment. A 1D model accurately describes a single out-coupling pulse because it is essentially independent of the spatial structure. However, we found that a full 3D simulation was needed to accurately track the spatio-temporal dynamics of a multi-pulse experiment. We simulated up to 3.2 ms, allowing three pulses for each case. Parallelised code was run on twelve processors of the APAC National Facility [156], requiring up to 800 hours of processor time per simulation. The numerical method was the psuedo-spectral method with Runge-Kutta split time step developed at the University of Otago [157]. Spatial grid sizes and time steps were monitored throughout the simulations to ensure the accuracy of the numerical solutions; e.g. the preservation of the normalisation. Spatial grids were grown, and time steps decreased, as required. At the end of simulations, spatial grids in the direction of gravity were 2048 points for the trapped ($m_F = 2, 1$) and anti-trapped ($m_F = -2, -1$) Zeeman states, and 4096 for the atom laser output state ($m_F = 0$). In the tight and loose transverse directions, 128 and 32 points were used respectively. The corresponding spatial lengths were chosen so that both the momentum space and real space GP functions fit the grid. This was about 40 μm and 140 μm in the tight and loose trap directions, respectively. In the direction of gravity, it was 120 μm for the $m_F \neq 0$ states, and twice that for the $m_F = 0$ state. Absorbing boundaries were used for the $m_F = 0, -1, -2$ states.

The simulations reveal that *all five Zeeman states are involved in determining the final form of the atom laser output.* The $m_F = -2$ state has the least effect, as it is not strongly populated, and it quickly disperses in its anti-trapping potential. However the $m_F = -1$ anti-trapped state is highly populated and is directly involved in the loss of the initial pulse for the case of Fig.4.7(c). The simulation in the left section of Fig. 4.10 shows how the first $m_F = 0$ atom laser pulse is destroyed by the second RF pulse: it transfers nearly all of the $m_F = 0$ component, produced by the first pulse, into the other four Zeeman states (second row, Fig. 4.10). A new $m_F = 0$ pulse, somewhat lower than the first, originates from the $m_F = -1$ state. However, it retains the momentum spread due to the anti-trapping potential, which causes it to disperse and be lost, so that it is not observed in the experiment.

The second atom laser pulse is in fact two distinct pulses; an upper one originating from the $m_F = 2$ state, and a lower one from the $m_F = 1$ state. This can be seen most clearly in the third row of Fig. 4.10, after they have become well separated. Since the two pulse components are not resolvable in the experiment, this is an example of the dynamics revealed by simulation. These components have different initial momenta. The $m_F = 1$ component, which originated from the $m_F = 2$ state in the first RF pulse, was moving down towards its trap equilibrium when the second RF pulse arrived.

The lower $m_F = 0$ pulse created by the second RF pulse escapes the fate of the first pulse because its downward momentum takes it lower than the first pulse, away from resonance. In fact, its position is close to that of the upper second $m_F = 0$ pulse during the third RF pulse in the case of Fig.4.7(b), and it survives for similar reasons. This can be seen by comparing the bottom rows of the $m_F = 0$ columns of Fig. 4.10. Similarly the simulations explain the relative intensity of the first and second $m_F = 0$ pulses in the experimental case of Fig.4.7(b).

4.5.3 Conclusion

By conducting experimental and numerical studies of the $F = 2$ atom laser we have demonstrated that beyond a critical flux the classical noise on the output beam increases with increasing flux. The prospect of combining atom lasers with atom chips opens up enormous possibilities in precision measurement. Considerations of the trade off between classical noise and flux in atom lasers will be important in many applications in this field. We would expect many of the effects described here to be smaller for the $F = 1$ atom laser but not absent. Rather than the two trapped states present in the $F = 2$ laser, only the $m_F = -1$ state is trapped. Although atoms in the $m_F = 1$ state are anti-trapped for the $F = 1$ laser, this state would be significantly populated for strong outcoupling and could be expected to contribute to classical noise on the $m_F = 0$ output beam just as the anti-trapped $m_F = -1$ state does for the $F = 2$ laser studied in this chapter. The effects that we have described will be important not only for pulsed atom lasers, but also for unpumped continuous atom lasers. Just as in the pulsed case, at high flux, atoms will not only be coupled to the output beam, they will also be coupled to other trapped and untrapped Zeeman states and can be backcoupled from the output beam to the condensate. The situation is complex and requires detailed investigation. The quantitative comparison between theory and experiment presented here is unique and points the way to the future development of atom laser sources for precision measurement. This is particularly true for the development of the pumped atom laser, one of the most important and sought-after devices in the field of atom optics.

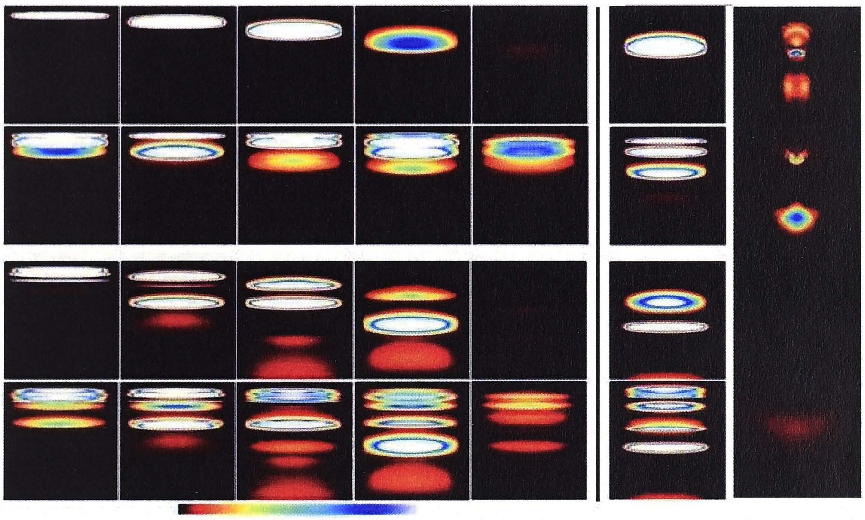

Figure 4.10: (color) Numerical simulations of the multiple-pulse atom laser experiments **produced by Dr. Craig Savage** for the cases of Fig. 4.7(c) and 4.7(b). Case 4.7(c) is to the left of vertical line. Each image shows the GP wavefunction density, in arbitrary units, integrated through the tight trap direction. Density is indicated by the colobar at the bottom of the figure, with black and white corresponding to zero and high density respectively. Each image is 120μm in both directions. From top to bottom the rows are: $t = 1.2$ ms, just before the 2nd RF pulse; just after the 2nd RF pulse; $t = 2.4$ ms, just before the 3rd RF pulse; just after the 3rd RF pulse. $t = 0$ is the beginning of the first RF pulse. The columns from left to right are the $m_F = 2, 1, 0, -1, -2$ states. The top-left image therefore shows the trapped position of the initial $m_F = 2$ condensate. Case 4.7(b) is to the right of vertical line. Only the $m_F = 0$ state is shown. The rows are as before but the RF pulses occur at $t = 1.6$ ms and $t = 3.2$ ms. Each image is 120μm vertically and 140μm horizontally. The rightmost image shows the $m_F = 0$ state density on a slice plane through the tight trap direction, just after the 3rd RF pulse. It is 40μm horizontally and about 150μm vertically, allowing the first pulse to be seen. Dimensionless simulation parameters: $\Delta = -633$, $\Omega = 457$. See text for discussion.

CHAPTER 5

Pumping an atom laser

In Chapter 4, we showed that the stability of an atom laser output beam is limited by classical ('technical') noise and nonlinear dynamical effects. In this chapter, we theoretically investigate the output flux of an atom laser, in the presence of a generic pumping mechanism. We fully model the output beam and experimentally important physics such as three-body recombination using a comprehensive one dimensional mean-field simulation. Previous theoretical studies have highlighted both the similarities and the differences between optical and atom lasers (e.g. [41, 158, 159, 160, 161, 162]). The differences arise because atoms are more complex than photons: they have mass, giving a different free space dispersion relation, and they interact with each other, producing strong nonlinearities. The latter generates complex dynamics, potentially complicating certain experimental measurements, of quantum noise for example. Nevertheless, a knowledge of the output beam dynamics might be useful in probing the excitations of the trapped condensate [163, 164].

A classical nonlinear model of the laser as a noise driven van der Pol oscillator shows that the noise power, in both the phase and the amplitude, decreases in inverse proportion to the laser power [166]. Schawlow and Townes showed that optical lasers' first order coherence, or linewidth is limited, and decreases in inverse proportion to the laser power [48]. Analogous results have been derived for atom lasers [151]. In practice, however, the Schawlow-Townes limit is not achieved, because the linewidth is dominated by technical noise and by dynamical effects rather than by quantum noise. For example relaxation oscillations, due to the nonlinear interaction between the inversion and the light, are the primary determinant of the low frequency noise spectrum in many optical lasers [167].

In the following, we focus on one aspect of the nonlinear dynamics of a pumped atom lasers: the frequency spectrum of the atom laser output beam density. In particular, we investigate how the spectrum depends on the pumping rate. An experimentally measured spectrum would also include genuine "noise" due to physical processes that we do not model, such as fluctuations in the trapping potential. This investigation is motivated by the inverse relation between noise power and pumping rate in the optical laser. We choose to focus on the density because it is possible to measure it experimentally using continuous optical techniques [7, 176].

The main conclusion of this chapter is that three-body recombination plays a

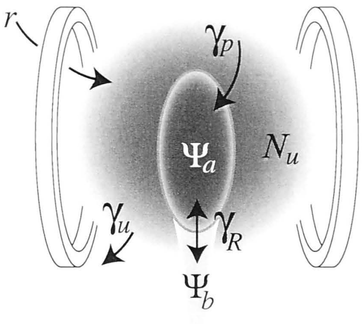

Figure 5.1: Schematic representation of our atom laser model. The rings represent coils producing the trapping potential. The symbols are defined in the text. Atoms are injected into the non-condensed fraction. They can then either be lost from the interaction region or pump the condensate. They are coupled out of the condensate by a Raman transition and then fall in the gravitational field.

major role in the high frequency dynamics. As the pumping rate is increased, the spectral peaks weaken and move to higher frequencies. Since the pumped atom laser is yet to be realised, this knowledge of the fluctuation properties of the output will serve as an important guide for atom laser experiments and measurements of their noise properties.

5.1 The model

Our atom laser model is schematically illustrated in Fig.5.1. It consists of a dilute gas Bose-Einstein condensate trapped by a highly anisotropic, effectively one-dimensional, potential. This is pumped from a reservoir of non-condensed trapped atoms. We consider a different mechanism of condensate output coupling from that presented in Chapter 4, and assume that the output atom laser beam is generated by a Raman transition (see section 2.8.1) to an untrapped atomic state. Unlike the 5-state model of the unpumped atom laser introduced in Chapter 4, here we assume a two state atom laser created from the $F = 1, m_F = -1$ state of ^{87}Rb. The output coupling is weak so that the anti-trapped state $F = 1, m_F = 1$ is not populated. Our model builds on that of Kneer *et al.*[161] by adding three-body recombination and a propagating output beam. In the following, we will refer to the trapped Bose-Einstein condensate as the "condensate", and to the output beam as the "beam". We make the mean-field approximation in which the condensate and beam are described by the classical fields $\Psi_a(x,t)$ and $\Psi_b(x,t)$ respectively, which obey Gross-Pitaevskii type equations [22]. Our model is more complete than previous mean-field treatments of a 1D atom laser model [161, 118, 148, 145, 169] since we include pumping, output coupling, three-body recombination, and explicitly model the dynamics of the pump reservoir, the condensate, and the beam. Although the extension to three dimensions is straightforward, we do not perform it here due to the computational demands of 3D numerics.

To describe the pumping we use a phenomenological model, which imitates the pumping of an optical laser [161]. It depends only on the total number of atoms in the uncondensed component, $N_u(t)$, not on its spatial structure. The condensate atoms are coupled, by a reversible Raman transition [4, 118, 59], to an untrapped electronic state forming the atom laser beam. The Raman transition imparts a momentum kick $\hbar k$ to the out-coupled atoms. The beam evolves under the influences of gravity and atom-atom interactions, which are dominated by those due to the condensate. We have considered only the particular case in which the Raman coupling is tuned to transfer atoms starting from the centre of the harmonic trap [118]. Hence, the output beam overlaps with the lower half of the condensate. Experimentally, three-body recombination is well described as a collisional loss process occurring at a rate proportional to the cube of the local density [170]. We follow Kagan *et al.* [171] in incorporating three-body recombination into the atom laser Gross-Pitaevskii equations.

Our model is defined by the following dimensionless equations:

$$
\begin{aligned}
\frac{dN_u}{dt} &= r - \gamma_u N_u - \gamma_p N_u N_a, \\
i\frac{\partial \Psi_a}{\partial t} &= -\frac{1}{2}\frac{\partial^2 \Psi_a}{\partial x^2} + \frac{1}{2}x^2\Psi_a + U_a\Psi_a|\Psi_a|^2 \\
&\quad + U_{ab}\Psi_a|\Psi_b|^2 - i\gamma_r\Psi_a(|\Psi_a|^4 + |\Psi_b|^4) \\
&\quad + \gamma_R e^{ikx}\Psi_b + \frac{i}{2}\gamma_p N_u \Psi_a, \\
i\frac{\partial \Psi_b}{\partial t} &= -\frac{1}{2}\frac{\partial^2 \Psi_b}{\partial x^2} + Gx\Psi_b + U_b\Psi_b|\Psi_b|^2 \\
&\quad + U_{ab}\Psi_b|\Psi_a|^2 - i\gamma_r\Psi_b(|\Psi_a|^4 + |\Psi_b|^4) \\
&\quad + \gamma_R e^{-ikx}\Psi_a.
\end{aligned} \tag{5.1}
$$

The model is made dimensionless using the characteristic trap length $l = (\hbar/\omega m)^{1/2}$ and angular frequency ω, with m the atomic mass. Hence time t, position x, and the wavefunctions are measured in units of ω^{-1}, l and $l^{-1/2}$, respectively. Experimentally reasonable values of the parameters are: a trap frequency $\omega \approx 125$ Hz [3], and the atomic mass of sodium $m = 3.8 \times 10^{-26}$ kg. These give a time scale of $\omega^{-1} = 8$ ms, and a length scale of $l = 4.7$ μm.

Atoms are injected into the uncondensed fraction at the rate r, are lost at the rate $\gamma_u N_u$, and pump the condensate at the rate $\gamma_p N_u N_a$, where $N_a = \int_{-\infty}^{\infty} |\Psi_a|^2 dx$ is the total condensate population. U_a and U_b are the intra- and U_{ab} the inter- species two-body interaction coefficients. The dimensionally correct coefficients can be written as $U_{a,b,ab} = 4\pi a_s/(\hbar/\omega m)^{1/2}$ with a_s the appropriate s-wave scattering lengths [118]. We have previously found that three-body recombination, with coefficient γ_r, is necessary for the system to reach a quasi-stationary-state on a timescale comparable to experimental condensate lifetimes [172]. The three-body recombination rate $\gamma_r =$

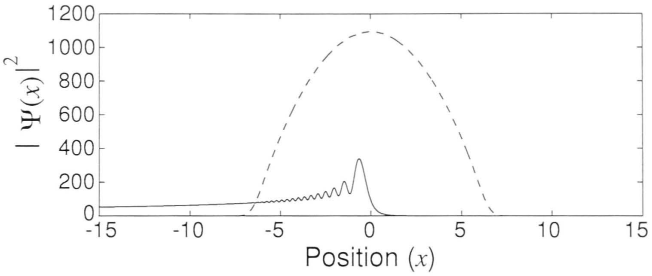

Figure 5.2: Densities of the condensate (dashed) and beam (solid) versus position. All quantities are dimensionless. The plotted beam density is 100 times the true value. These results are a numerical solution of Eqs. (5.1) at $t = 200$ after starting from a seed condensate. Parameters are: $r = 1600$, $U_a = U_b = 0.02$, $U_{ab} = 0.01$, $G = 12$, $\gamma_R = 0.5$, $\gamma_u = \gamma_p = 0.1$, $\gamma_r = 10^{-7}$ and $k = 5$. Gravity is to the left.

10^{-7} is chosen to produce $N_a \approx 3500 - 9500$ condensed atoms at steady state, as the pump rate varies from $r = 200$ to 1600. For simplicity, we assume that the inter- and intra-species three-body recombination rates are the same. G is the scaled gravitational acceleration [173]. Gravity has not been explicitly included for the trapped atoms, since, for the purposes of this work, it is equivalent to a spatial shift of the trap potential. The Raman coefficient γ_R is a function of the Raman laser amplitude and detuning [59].

Our numerical method for solving Eq. 5.1 is a split-step Fourier method [175] with a fourth order Runge-Kutta in place of the usual nonlinear step (see appendix B). We have absorbing boundaries at the ends of the spatial grids to prevent reflections.

5.1.1 Numerical results

Typical results for quasi-stationary-state spatial profiles of the condensate and beam densities are shown in Fig. 5.2. For our parameters, the condensate shape is well described in the Thomas-Fermi approximation. Note that the plotted output beam density has been scaled up by a factor of 100. The flux in the beam is about 90 atoms per unit dimensionless time, or about 1.1×10^4 atoms per second with $\omega = 125$ Hz. The prominent spatial oscillations of the output beam, occurring within the extent of the condensate, have been observed in previous work [148, 174] and are related to the oscillatory Airy type eigenfunctions of the condensate wavefunction in the linear gravitational potential.

In Fig. 5.3, we show the output beam density $|\Psi_b(x_0, t)|^2$ as a function of time at a fixed position far from the trapped condensate. The time span has been chosen to be longer than that of the transient dynamics associated with the growth of the condensate from a seed, and short enough to be experimentally accessible. Quasi-stationary, nearly periodic dynamics develop, becoming approximately har-

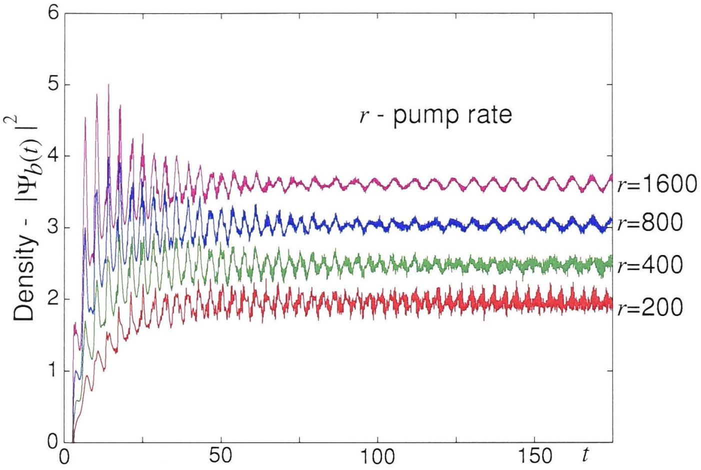

Figure 5.3: The output beam density, $|\Psi_b(x_0, t)|^2$, as a function of time at position, $x_0 = -45$, for different pump rates: from bottom to top $r = 200$, 400, 800, and 1600. All quantities are dimensionless. Other parameters are as for Fig. 5.2.

monic for large pump rates r. We have verified that the quasi-stationary dynamics is independent of the particular form of the seed used to initiate the condensate growth. The fundamental oscillation of the beam, at higher pump rates, arises from the well known Kohn mode [22], corresponding to a rigid "sloshing" back and forth of the condensate at the trap frequency.

Fig. 5.4 shows the frequency spectra of the density time series in Fig. 5.3, and is the central result of this chapter. The spectra are those of the final, quasi-steady, parts of the time series ($t > 100$ in Figure 5.3). The frequencies are well approximated by the eigen-frequencies of an uncoupled 1D condensate in a harmonic trap. Kneer *et al.* [161] found these to be $\Omega = \omega\sqrt{n(n+1)/2}$ where $n = 1, 2, 3, \ldots$, with the corresponding spatial modes given by the Legendre polynomials $P_n(x)$. The Kohn sloshing mode at ω is $n = 1$, and $n = 2$ is the breathing mode at $\sqrt{3}\,\omega$.

Fig. 5.4 shows that as the pumping rate r increases, the slow beam oscillations change from the frequency of the condensate breathing mode (prominent peak at $\sqrt{3}\,\omega$ in top panel) to that of the sloshing mode (prominent peak at ω in lower panel). This is because the *trapped* condensate dynamics changes from breathing to sloshing at higher pumping rates. As Kneer *et al.* [161] noted, the sloshing mode is spatially asymmetric and hence must be excited by a spatially asymmetric perturbation, such as the output beam. This is consistent with the observed increase of the sloshing mode power with the density of the output beam, that is with pumping rate. On the other hand, mode damping due to three-body recombination increases rapidly with density. We have verified that in a simple model of the Kneer *et al.* [161] form, the breathing mode decays with pumping rate.

Although the classical noise frequencies in the output beam are primarily de-

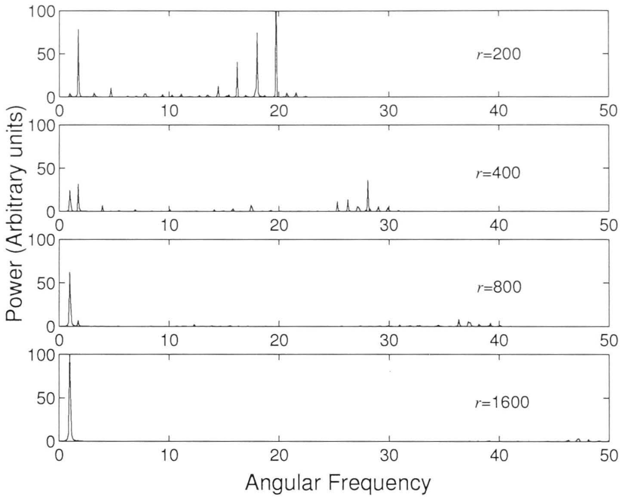

Figure 5.4: Frequency spectra of the time dependent density of the fields in Fig. 5.3, calculated as $S(\omega) = |\Phi_b(\omega)|^2$ where $\Phi_b(\omega)$ is the Fourier transform of $\Psi_b(t)$. All quantities are dimensionless. The spectra are those of the time series from $t = 112.5$ to $t = 175$. The pump rates from top to bottom are $r = 200$, 400, 800, and 1600. The normalization has been chosen so that the largest peak height (that near 20 frequency units for r=200) is 100 units. The peaks just below 50 frequency units, for $r = 1600$, are almost invisible on this scale.

termined by the condensate, there is a complex relationship between the power spectra of the condensate and that of the beam. In particular, the beam spectrum reflects the spatial dependence of the condensate spectrum. Consider, for example, the condensate Kohn sloshing mode. The magnitude of the local density change varies with the spatial derivative of the density profile. It is maximum where the condensate has greatest slope, and zero at the center where the slope is zero. The prominence of the Kohn mode frequency in the power spectrum of the output beam indicates that the coupling between the condensate and the beam is not confined to the center of the condensate. Similar observations apply for the high frequency components of the power spectrum.

As the pumping rate increases, Fig. 5.4 shows that the mean frequency of the high frequency spectral components of the noise increases and the noise power decreases rather dramatically. A decrease of spectral power with pumping rate, due to gain saturation, is characteristic of optical lasers (see discussion in section 1.6.2). Since three-body recombination contributes to gain saturation in atom lasers, we have investigated its role in a simplified pumped atom laser model with a spatially uniform phenomenological loss rather than an explicitly modelled output beam. Without three-body recombination the condensate density power spectrum simply rolls off at high frequencies. Adding three-body recombination produces a high frequency spectral group, such as seen in Fig. 5.4. The precise origin and the dynamics of this spectral group is described in detail in an extension of the work presented in this chapter [154, 155].

5.2 Conclusion

In conclusion, we have explored some of the rich and complex behavior of the atom laser with a model incorporating important experimentally relevant physics, such as three-body recombination. The latter was found to strongly influence the spectrum of the atom laser output beam. This work represents a first step towards the future goal of understanding and measuring the noise properties of the pumped atom laser. We have show that at high pump rates three-body recombination plays a role in suppressing the high frequency dynamics, which would otherwise limit the stability of the output beam.

CHAPTER 6

Next generation atom laser machine

6.1 Design philosophy

This chapter details the design of our third generation BEC machine, although the machine is not yet fully operational at the time of writing. Having obtained stable BEC in our second generation machine (see chapter 3), our primary goal was to construct an extremely stable machine specifically for the production and study of continuously pumped atom laser systems. As a secondary consideration, we wanted the ability to quickly implement different optical dynamical detection systems (as described in [176]) around the magnetic trap. Finally, we wanted the machine to run with a minimum amount of supervision from the user while automatically supplying useful dynamical information from run to run. Design of the new magnetic trap and geometry of the experiment dedicated to the new atom laser machine are outlined below. The details of the pumping mechanism are currently being finalised as part of a theoretical research program, and will not be discussed in this chapter.

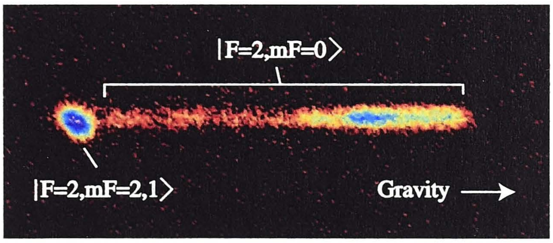

Figure 6.1: The quasi-continuous atom laser produced by the author shows a non-uniform beam flux, which is associated with the short term bias field stability of our present magnetic trap ($\approx$ 1mG over the 12 ms out-coupling time). The long term fluctuations lie within a range of ± 12 mG.

6.2 An optimized QUIC trap for BEC

The recipe for producing Bose-Einstein condensation (BEC) by a combination of optical cooling followed by forced evaporation in a magnetic trap is now well established, based mainly on the pioneering work of the MIT and JILA groups [1]. As discussed in Chapter 2, initial work on evaporative cooling found that atomic confinement in a linear quadrupole magnetic trap failed at low kinetic temperatures due to Majorana spin flip losses [136]. A number of solutions were found to this problem including optical plugs [1], time orbiting potentials (TOP) [93], and the Ioffe-Pritchard (IP) trap [54], all of which yielded BEC. Of these solutions the DC IP-trap is arguably the simplest, even in its most complex realization (up to eight coils). However designing a trap of any type for BEC experiments is a formidable task as many parameters must be balanced and fine tuned in order to get a workable system. Considerations such as power dissipation, mechanical stability, optical access and inductance (switching times) must be combined with the requirement to achieve a high geometric trapping frequency (for optimal evaporative cooling) and a stable bias field. Stability of the trap bias is especially critical for studies of the atom laser. Although continuous atom lasers have been demonstrated by a number of groups (see Fig. 6.1 and [5, 116, 105]), repeatable, reliable operation of the trap bias to approximately the 0.1 mG level is required for experiments with continuous outcoupling. Typical magnetic traps for BEC report stabilities of more than 100 times this value.

In this section we describe a general methodology for the complete design and optimization of a three coil IP trap conceived by Söding et.al [96] and developed into the tightly confining quadrupole Ioffe configuration (QUIC) design at Munich [97]. In particular, we point out that for studies of atom lasers inherent thermal stability of the magnetic trap is as important a figure of merit as well as the previously suggested radial gradient of an IP trap [95]. The relatively simple configuration of the QUIC trap has allowed us to combine numerical optimization with geometrical arguments to obtain a set of theoretical tools for the design optimization of our magnetic traps. The resulting system can be operated in a 'high power' regime at 500 W to achieve radial trapping frequencies of greater than 630 Hz and in 'low power' mode at 60 W generating radial frequencies of 220 Hz. In the second case, air cooling is more than sufficient to dissipate the heat generated.

6.2.1 Three loop QUIC trap

The theoretical framework developed by Bergeman et. al. [177] can be applied to generic IP trap configuration to obtain analytic equations for the trapping field as a function of the geometrical parameters of the trapping coils. One of the important and often quoted results of this work is, that for an IP-type trap, the field is approximately harmonic about a non-zero field minimum (B_0), the radial (tight) trapping scaling with the inverse of B_0 (see Equations 2.3,2.4).

The configuration of the QUIC trap is shown in Fig. 6.2(a). In this setup, an Ioffe-Pritchard trap is generated by two quadrupole loops (oriented along the

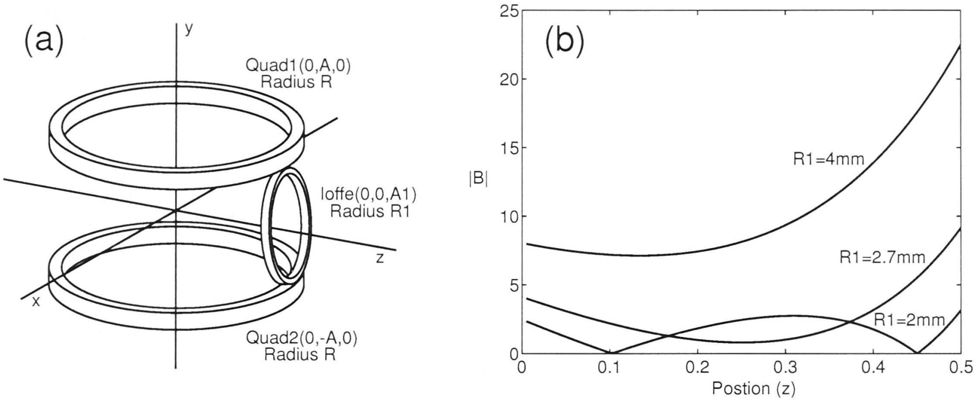

Figure 6.2: (a) Schematic of the QUIC magnetic trap, showing the relative position of each coil. (b) Formation of an IP trap at $R1 = 2.7$ mm, a harmonic trap with a high bias at $R1 = 4$ mm and two quadrupole traps at $R1 = 2$ mm, all parameters of the trap are held constant and the radius of the Ioffe coil, $R1$, is adjusted as described in the text.

y-axis) with opposite current which produce a field $\mathbf{B_Q}$ which increases linearly in all directions from a zero at the origin. The Ioffe loop (oriented along the z-axis) produces a non-linear magnetic field, $\mathbf{B_I}$, which, when summed with the linear quadrupole field, gives an approximately harmonic field along the z-axis. In the radial directions, the Ioffe field equalizes the gradient produced by the quadrupole coils to produce a radially symmetric trap. Unless arranged appropriately the three loops will produce a field, $|\mathbf{B}|$, along the Ioffe (z) axis consisting of either two quadrupole traps or a harmonic trap with a very large bias, B_0, as shown in Fig 6.2(b).

Order	Coefficient
0	$\frac{1}{2}\frac{I\,\mu\,R1^2}{(R1^2+A1^2)^{(3/2)}}$
1	$-\frac{1}{32}\frac{I\,\mu\,R^2\,A(48\,R^{12}+720\,A^4\,R^8+288\,R^2\,A^{10}+288\,A^2\,R^{10}+48\,A^{12}+720\,A^8\,R^4+960\,A^6\,R^6)}{(R^2+A^2)^{(17/2)}}+\frac{3}{2}\frac{I\,\mu\,R1^2\,A1}{(R1^2+A1^2)^{(5/2)}}$
2	$\frac{1}{2}\frac{I\,\mu\,R1^2\,(6\,A1^2-\frac{3}{2}\,R1^2)}{(R1^2+A1^2)^{(7/2)}}$
3	$\frac{3}{128}\frac{I\,\mu\,R^2\,A\,(-320\,A^2\,R^8-80\,A^4\,R^6+480\,A^6\,R^4+520\,R^2\,A^8-120\,R^{10}+160\,A^{10})}{(R^2+A^2)^{(17/2)}}+\frac{5}{4}\frac{I\,\mu\,R1^2\,A1\,(4\,A1^2-3\,R1^2)}{(R1^2+A1^2)^{(9/2)}}$
4	$\frac{1}{2}\frac{I\,\mu\,R1^2\,(\frac{15}{8}\,R1^4-\frac{45}{2}\,A1^2\,R1^2+15\,A1^4)}{(R1^2+A1^2)^{(11/2)}}$
5	$-\frac{5}{256}\frac{I\,\mu\,R^2\,A\,(-420\,A^2\,R^6-1134\,A^4\,R^4-168\,R^2\,A^6+336\,A^8+210\,R^8)}{(R^2+A^2)^{(17/2)}}+\frac{21}{16}\frac{I\,\mu\,R1^2\,A1\,(5\,R1^4-20\,A1^2\,R1^2+8\,A1^4)}{(R1^2+A1^2)^{(13/2)}}$
6	$\frac{1}{2}\frac{I\,\mu\,R1^2\,(-\frac{35}{16}\,R1^6+\frac{105}{2}\,R1^4\,A1^2-105\,R1^2\,A1^4+28\,A1^6)}{(R1^2+A1^2)^{(15/2)}}$
7	$\frac{35}{2048}\frac{I\,\mu\,R^2\,A\,(-2352\,R^2\,A^4-245\,R^6+1960\,R^4\,A^2+448\,A^6)}{(R^2+A^2)^{(17/2)}}-\frac{7}{32}\frac{I\,\mu\,R1^2\,A1\,(35\,R1^6-280\,R1^4\,A1^2+336\,R1^2\,A1^4-64\,A1^6)}{(R1^2+A1^2)^{(17/2)}}$

Table 6.1: Polynomial coefficients for the magnetic field, $|B_z| = a + bz + cz^2....$, produced along the z-axis of the QUIC trap. The terms on the far right are contributions from the Ioffe coil (including the zero order term). Here A and R are respectively the position and radius of the quadrupole coils. A1 and R1 are respectively the position and radius of the Ioffe coil. I is the current and μ is the permeability of free space.

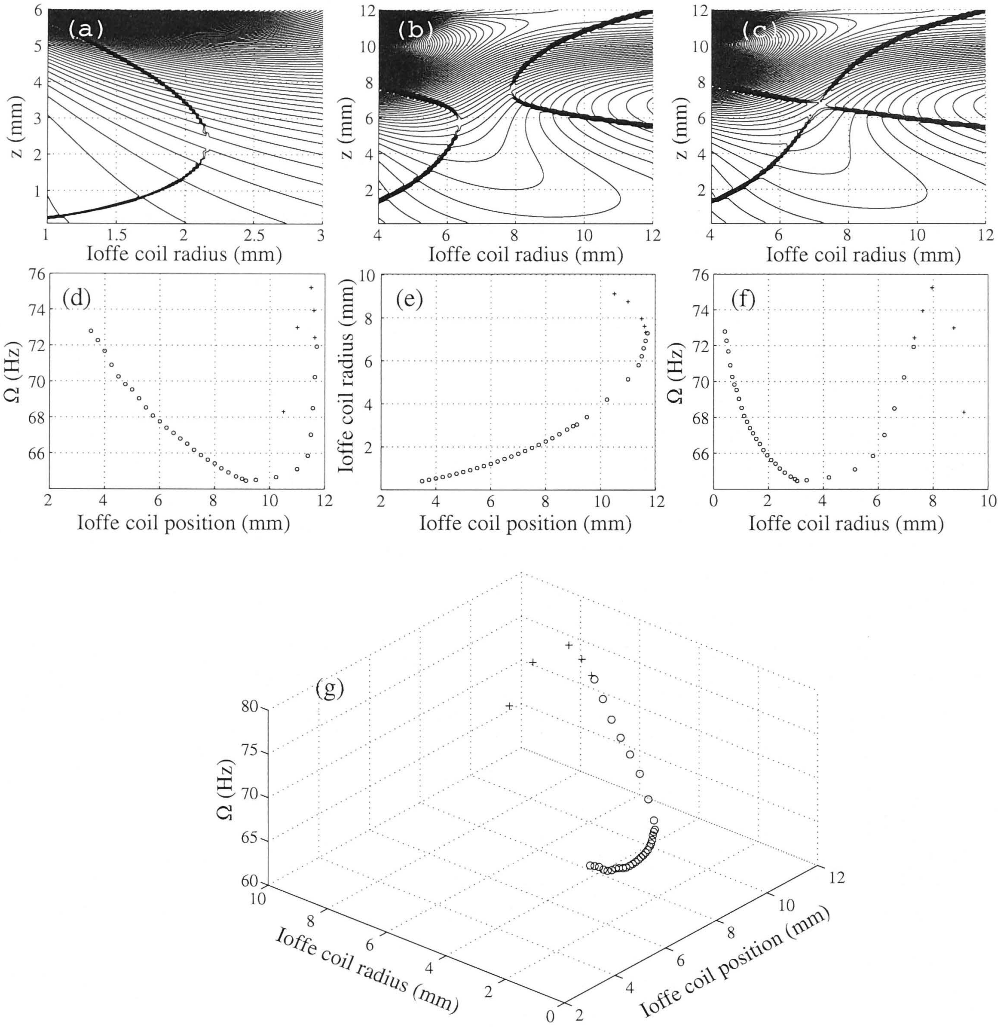

Figure 6.3: The upper row of the figure shows a series surface contour plots of the gradient of the modulus of the magnetic field along the z-axis of the trap, for varying values of the Ioffe coil radius. These plots are a 'device' for clearly identifying the transition from quadrupole to Ioffe trap. The dark lines indicate the discontinuity of the gradient coinciding with the magnetic field zero of the quadrupole trap. For this calculation the radius of the quadrupole coils was set to 1 cm and they were positioned at $y = \pm\ 0.5$ cm. Current in all coils was 100 A. (a) Ioffe coil position 0.8 cm, (b) Ioffe coil position 1.16 cm, (c) Ioffe coil position is 1.17 cm. Panels (d), (e) and (f) show *elevations* of the 3 dimensional space in (g), defined by the geometric trapping frequency as a function of position and radius of the Ioffe coil. Crosses representing the second larger Ioffe coil solutions and open circles representing the first (smaller coil) standard solution.

An added difficulty is that for a QUIC trap, it is generally not possible to know where the axial (z) field minimum will be prior to making numerical calculations of the magnetic field. This is because the equations for the radial and axial magnetic field of a coil contain elliptic integrals which can be evaluated only numerically. As a rule of thumb, the trap will form at roughly the radius of the Ioffe coil used to produce it. Some further insight can be gained by using the formalism of Bergeman et. al. [177] which allows one to approximate the magnetic trapping fields in multipole polynomial expansions, allowing the generation of accurate analytic expressions for the magnetic fields produced by the QUIC trap configuration. In table 6.1, we tabulate the results of our calculations for the total magnetic field generated by the three single turn coils in the QUIC-trap configuration detailed in Fig. 6.2(a) along the axis of the Ioffe coil. Each term in the table corresponds to the coefficient of a polynomial describing the field component, $|B_z| = a+bz+cz^2$..... Note that the quadrupole coils produce a field in *odd powers*. For a fixed position of all coils, a Taylor expansion around the trap minimum shows that this is the physical reason why the Ioffe coil alone determines the bias field ($\propto 1/R_1$) and axial trapping frequency ($\propto 1/R_1^3$).

We also point out, that for the QUIC magnetic trap, a *large* Ioffe coil can produce geometrical trapping frequencies, $(\omega_\rho^2\omega_z)^{1/3}$, greater than a small Ioffe coil, contrary to previous understanding [97]. This result cannot be derived from the analytics in the preceding table, as an expansion to unreasonable orders would be required to accurately represent the exact numerical solution. To demonstrate this point, we fix the radius and position of the quadrupole loops as well as the current in all coils and then calculate the geometric trapping frequency at a given bias field, B_0, generated at varying positions and radii of the Ioffe coil. In figure 6.3, we present the results of our numerical calculations, which can be summarized as follows. If the Ioffe coil position along the z-axis is less than the *radius* of the quadrupole coils, then there is a unique radius of the Ioffe coil that produces an IP trap at a particular bias field (see Figure 6.3(a)). As the Ioffe coil is moved away from the origin of the z-axis, the geometric trapping frequency decreases (see Figure 6.3(d)). If the Ioffe coil is placed beyond the radius of the quadrupoles coils, two different radii of the Ioffe coil will produce an IP trap of the same bias at different positions (see Figure 6.3(b)). In particular, as the coil is moved further out the geometric trapping frequency rises asymptotically until the two solutions merge and a IP trap can no longer form (see Figure 6.3(c)). This analysis points to the possibility of producing tight trapping with larger coils than are traditionally used, which may be advantageous under particular experimental conditions.

6.2.2 The ideal QUIC trap and figures of merit

It is difficult to discuss any implementation of a magnetic trap without imposing some physical limitations on the system (such as accommodating vacuum and laser systems). Some general comments can be made about magnetic traps. Smaller coils produce inherently larger gradients and hence are ideal for neutral atom traps. This principle has been applied extremely successfully to produce magnetic micro-traps or BECs-on-a-chip (see [12] and references therein) with radial trapping frequencies in the 10's of KHz providing fast evaporation and extreme aspect ratios. For macro-magnetic traps the figure of merit for the efficiency of a trap is widely accepted to be the ratio of the radial gradient of the IP trap to the power dissipation [95, 178]. The best designs will minimize power dissipation while maximizing the gradient. Here we emphasize that stability of the trap is critical to the production of a continuous atom laser and hence we introduce a further criterion for the magnetic trap: thermal stability. This relates to the run to run temperature rise of the magnetic trap and the efficiency of a cooling system to remove the heat generated. Run to run temperature changes must be minimised in order to avoid runaway resistive heating, particularly so for a many turn solenoid.

Let us consider the three loop system from the perspective of generating the largest possible geometric trapping frequency under some realistic experimental constraints. The configuration that produces maximum radial gradient from two loops of wire in a quadrupole configuration can be calculated analytically. The radial gradient will be maximized when the loops satisfy the condition $R_Q = \sqrt{2/3}A_Q$ (Note that the 'true' anti-Helmholtz configuration $R_Q = 2A_Q$ generates a gradient about a factor of 3 smaller at the centre of the quadrupoles). Thus the only free parameters are the Ioffe loop position and radius. As was shown in the previous section, if the position of the Ioffe loop lies within the radius of the quadrupole coils then at each position of the loop there is a unique radius of the coil that forms an IP magnetic trap at a given bias field. In this situation, the highest trapping frequency will be achieved by placing the Ioffe loop as close a possible to the centre of the quadrupole coils. For positions of the Ioffe loop outside the radius of the quadrupole coils the radial trapping frequency increases similarly to Figure 6.3(d) for increasing distance of the coil from the centre of the quadrupole trap. However for the optimized quadrupole loops the asymptotic value of the Ioffe coil radius that produces comparable trapping frequencies to small close coils is unreasonably large (2-3 times the radius of the quadrupole coils). For any geometrical experimental constraints we can use this optimized system of three loops to calculate the maximum geometrical trapping frequency for a given number of Amp-turns per loop and compare the result with a more realistic trap composed of solenoids.

Having found the optimum three loop configuration for a QUIC trap, we now turn our attention to the optimisation of the solenoids that comprise a real magnetic trap. There is a long history of optimizing magnetic coils for the production of extremely high magnetic fields dating as far back as Maxwell in 1870 [179]. It was pointed out by Fabry [180, 181] that the magnetic field produced by a solenoid could be expressed in terms of a dimensionless form-factor (now known as the Fabry G-factor). With reference to Figure 6.4 the expression for the magnetic field at any point, B, along the coil axis can be derived as [182]

$$B = \mu_0 \sqrt{\frac{P\lambda}{\rho r_{int}}} G \tag{6.1}$$

where P is the total power dissipated, λ is the fill factor determined by the ratio of winding volume to total coil volume, ρ is the conductor resistivity, r_{int} is the

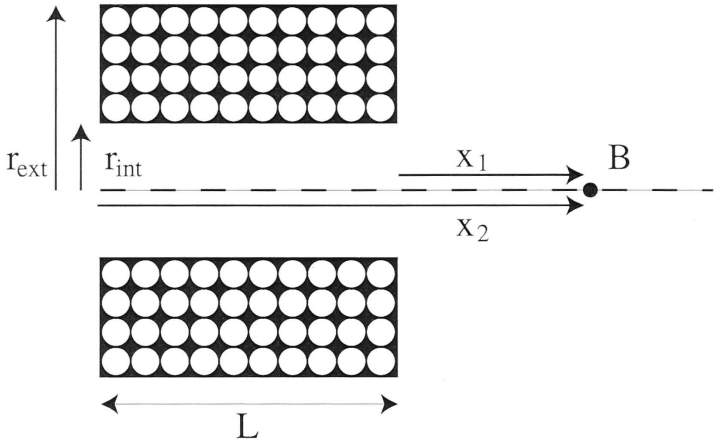

Figure 6.4: Dimensions of a magnetic coil and distances to measurement point, B. The fill factor λ is the ratio of the area of white wires to black total coil volume.

internal radius of the coil and G is the Fabry factor given by

$$G = \sqrt{\frac{1}{8\pi\beta(\alpha^2-1)}}\left((\gamma+\beta)\ln\frac{\alpha+\sqrt{\alpha^2+(\gamma+\beta)^2}}{1+\sqrt{1+(\gamma+\beta)^2}} - (\gamma-\beta)\ln\frac{\alpha+\sqrt{\alpha^2+(\gamma-\beta)^2}}{1+\sqrt{1+(\gamma-\beta)^2}}\right) \tag{6.2}$$

where $\alpha = r_{ext}/r_{int}$, $\beta = L/(2r_{int})$ and $\gamma = (x_1 + x_2)/(2r_{int})$. This expression is typically found in the literature in a form where the field at the centre of the coil is the only point of interest ($x_1 = -x_2$) in which case for a given power and inner radius of the coil, the G-factor and hence the magnetic field is optimised under the conditions $\alpha = 3.09$ and $\beta = 1.81$ (this is for a homogeneous current density). It is important to note that these conditions do not provide a maximum G external to the coil, a condition that can only be found through numerical optimisation. Equation 6.1 provides an important guide in the design of magnetic coils for producing BEC. Prior to even choosing coil geometry one sees that for maximum efficiency, the internal radius of the coil should be made as small as possible and the fill factor, λ, should be made as close as possible to its maximum of 1. The hollow copper tubing used in most BEC machines (used to facilitate water cooling) is hence a poor choice giving fill factors of around 0.6 compared to solid wound solenoids that can come very close to 1. This amounts to almost a 25% reduction in efficiency for tube based coils.

6.2.3 Geometrical considerations

With the help of the previous section, it is now straightforward to design an optimum QUIC trap. One proceeds as follows: in order to keep power dissipation to a minimum, the coils should be placed as close to the vacuum system as possible, thus fixing the coil position. The quadrupole coils are designed first as these determine the radial gradient of the trap - the primary figure of merit of the trap [95]. The internal radius of the quadrupoles is fixed by a requirement that one has maximum optical access to the experimental chamber (we fix this to our glass cell size) for MOT beams. Particular care should be taken in setting this value if one intends to image the condensate through the quadrupole coils as the minimum of the IP trap can lie outside the field of view. Next, equation 6.1 is used to numerically optimize the *geometry* of the quadrupole coils to produce the largest radial gradient for a fixed power at the centre of the quadrupoles given that the coils are as close as possible to the trapping region. This procedure generates the most efficient quadrupole coils for a given vacuum system. The reader should note that at no stage was it necessary to use the number of windings of the coil or the operating current. Next, the Ioffe coil is designed. It was shown in section 6.2.1 that there are two possible configurations for the Ioffe coil. In the first, the coil lies between the quadrupole coils with its front facet as close as possible to the centre of the quadrupoles (in practice this position is once again set by restraints imposed by MOT beams and the vacuum system). Further, from equation 6.1, the internal radius should be made as small as practicable. Given a fixed position of the front facet of the coil and the internal radius, numerical optimisation at a fixed power yields a coil length and outer radius (limited by the position of the quadrupoles) that maximise efficiency. In the second configuration, the front facet of the Ioffe coil lies outside the radius of the quadrupole coils. In this case, there are no geometrical constraints on any of the parameters of the coil and there is no clear numerical optimum solution. Instead, we suggest here that for greatest stability, an Ioffe coil of exactly the same shape and power dissipation as the quadrupoles is used.

The above procedure sets the geometrical characteristics and positions of the coils and once settled on the characteristics of the coils, the wire diameter (which can be different for the Ioffe and quadrupoles), number of windings and current are then chosen to match the designed power dissipation. One can choose many windings at low current or fewer windings at high current. Generally the coil windings should be kept to a minimum to decrease inherent switching times via the smaller self-inductance. Using a simple diode/zener diode pair across a set of coils dramatically reduces the switch off time of the system (this time must be shorter than the period of one oscillation in the trap so that the atomic distribution is unaffected). In addition, common mode current noise is eliminated by running all three of the trap coils in series.

If three coils of the same power dissipation and geometric shape are used to create the QUIC trap, then three benefits are immediately clear. First, the coils' inductances are matched and hence so are the coil switching times, removing the need to carefully switch the coils to avoid spin flips prior to imaging [28, 138]. Second, any thermally related shape changes in the coils will be matched during an evaporative cooling run, reducing this source of trap instability in a similar way to the common mode noise reduction achieved by running the coils in series. Finally, because the Ioffe coil has the same shape as the quadrupole coils, it does not limit optical access to the trapping region. This inherently stable configuration is ideal for the production and study of continuous atom lasers, and we have named it the inherently thermally stable (ITS) QUIC trap.

6.2.4 Concrete examples

In this section, we examine three examples of the QUIC trap each based around a glass cell a little less than 30 mm×30 mm with 5 mm thick glass walls. In the first case, we consider an ITS QUIC magnetic trap that requires full MOT access where the trap is loaded diagonally and the MOT beams coincide with the faces of the glass cell as for example in the work of Myatt et al [123]. This configuration would also suit the production of 3D optical lattices. In the second case, we calculate an ITS QUIC trap configuration where the MOT is not coincident with the magnetic trap and the atoms are transported to the magnetic trap either via magnetic transport [183] or a moving quadrupole trap [184]. Finally, we consider a standard QUIC magnetic trap optimised to produce the tightest possible magnetic trap under the same conditions as case 2.

- For case one, the above analysis suggests that the front facets of the quadrupole coils should be placed at ±15 mm. We choose an inner radius of $R_{int} = 10mm$ to allow the largest possible MOT beams for the given cell. Optimising for maximum gradient yields $R_{ext} = 30.8mm$ and $L = 15.7mm$. The Ioffe coil is automatically taken to be the same as the quadrupole coils and is placed at the end of the glass cell, with imaging in the plane of the quadrupoles. Choosing wire diameters of 1.6 mm for the coils, we fit 147 turns into the coil volume giving a resistance of about 0.161Ω per coil. At a current of 25 A running through all coils the total power dissipation is around 300 W. With a bias field of 0.8G the IP trap minimum is at 11.1mm from the quadrupole symmetry axis with a curvature of $203G/cm^2$ and radial gradient of $232G/cm$ giving axial and radial trapping frequencies, $\omega/2\pi$, for $^{87}Rb\ m_F = 2$ of 18Hz and 335Hz respectively.

- As with case 1, the front facet of the quadrupole coils should be placed as close as possible to the glass cell at ±15 mm. In this case optical access through the quadrupole coils is not needed as there is no coincident MOT and the quadrupole coil internal radius is set to 5 mm. Numerical optimisation yields an external radius of 28.5mm and a length of 13.5mm. The Ioffe coil is taken to be the same as the quadrupole coils. If each coil is wound with 1.6mm wire it will have 143 turns. At 25 A the total power dissipated for all coils is 240 W. This winding produces a trap with an axial curvature of $294G/cm^2$ and a radial gradient of $282G/cm$, producing axial and radial trapping frequencies, $\omega/2\pi$, for $^{87}Rb\ m_F = 2$ of 22Hz and 407Hz respectively. By winding each coil with 1.33mm wire (each coils has 207 turns) at 25 A the total power dissipation is doubled to 500 W, giving an axial curvature of $425G/cm^2$ and a radial gradient of $406G/cm$, producing axial and radial trapping frequencies, $\omega/2\pi$, for $^{87}Rb\ m_F = 2$ of 26Hz and 585Hz respectively.

- The quadrupole coils are taken as for case 2. The Ioffe coil inner radius is set to 2mm (allowing some optical access) and with the guidance of Equation 6.1 the external radius is set to 15mm (the maximum possible, limited by the quadrupole coil positions). The length of the Ioffe coil is optimised for highest efficiency and is found to be 7.9mm. Choosing a wire diameter of 1.33mm for all coils we fit 207 turns in each quadrupole coil and 67 turns in the Ioffe coil. At 25 A running through all coils the total power dissipated is 365 W. With a bias field of 0.8G the trap minimum is at 5.7mm from the centre of the quadrupole coils with an axial curvature of $703G/cm^2$ and a radial gradient of $465G/cm$. In this case the axial and radial trapping frequencies, $\omega/2\pi$, for ^{87}Rb $m_F = 2$ are 34Hz and 670Hz respectively.

In each case the traps can be specified to run at extremely low power so that the need for active cooling (water, air or peltier) is all but eliminated. For example in the configuration of case 3 running at 9.26 A total power dissipation is 50 W. This produces a magnetic trap with a bias field of 0.8G, and axial and radial trapping frequencies, $\omega/2\pi$, for ^{87}Rb $m_F = 2$ of 20.9Hz and 249Hz respectively. Although case 3 produces the highest trapping frequencies, the small size of the Ioffe coil means that it will heat considerably more that the larger quadrupole coils. Large coils change temperature less over each experimental run (at a given input power), and hence are desirable as they virtually eliminate the effects of runaway resistive heating.

6.2.5 Construction techniques

The coils themselves can be wound directly onto the copper or teflon formers using a manually turned lathe and a teflon friction feed-through for the wire to keep tension. A removable teflon front former is always used to minimize the distance between the coils and vacuum system. Each layer of coil is wound and then a thin (but complete) covering of a high thermal conductivity epoxy resin (Duralco 132) is applied before winding the next layer. The outermost layer should have no epoxy resin to increase convective cooling (larger surface area of the ribbed copper compared to smooth epoxy). Care should be taken to ensure that all permanent metal formers are split to reduce eddy currents when the coils are switched off. Coils should be wound very carefully if design specifications are to be met, and that the coils must be positioned relative to one-another with close to μm accuracy.

6.2.6 Experimental verification

Once the coils are constructed, it is important to measure a number of properties of the magnetic trap prior to installation around the vacuum system:

- Trap power dissipation and cooling systems which are a significant contributing factor to the stability of the magnetic trap through heating effects. This test should be conducted to imitate as closely as possible the actual operation of the magnetic trap in a normal BEC run.

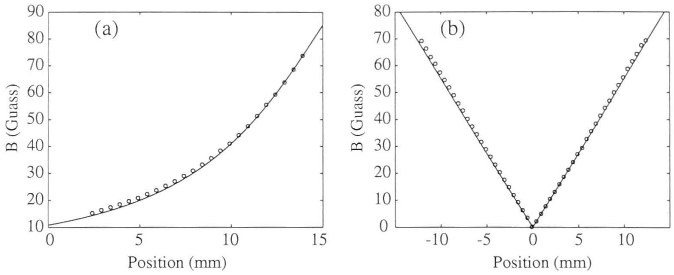

Figure 6.5: In (a) and (b) the field generated by our electromagnets is compared with the predictions of our models for the Ioffe coil and quadrupole trap respectively. Solid lines are numerical calculations of the solenoid fields using the law of Biot and Savart. Open circles are the measured field data. The coils are placed as they would be in the final trapping configuration, and are set to 3 A.

- Coil inductance and switching times. These are not so important as one can use an external scheme to speed up switching, but are still an important characteristic of the coils.

- Direct Gaussmeter measurements of magnetic field strength which are an important indicator that the coils have been built to specification.

Finally, once the trap is installed and running with ultra-cold atoms, a direct measurement of the trap frequencies can be made. This is an extremely important measurement as accurate calculations of the properties of a BECs cannot be made without this knowlege [53]. In Figure 6.5, we show a typical measurement of the magnetic field strength from a set of our coils. A Gaussmeter with an accuracy of ±0.01 G in 100 G full range was mounted on a micrometer translation stage to map out the magnetic field.

6.2.7 Conclusions

A careful analysis of the QUIC trap system has been undertaken in order to produce highly optimised traps for the production of BEC and studies of the continuous atom laser. We have introduced a methodology for the design of the QUIC magnetic trap based primarily on geometrical considerations to optimise the conversion of electric power to magnetic field strength. We have introduced the idea of thermal matching as an important design consideration, and described a number optimised traps, which operate at low powers but are able to produce very tight trapping.

6.3 Overview of the new system

Because the new machine is not fully operational, it seems inappropriate to give any more than a cursory overview of the system. Here, some of the more novel aspects of the design are highlighted. In order to best utilise the trap designs of the previous section, we decided that the UHV MOT should not be coincident with the magnetic trap. In this case, we did not have to compromise on trapping efficiency to accommodate large MOT beams. We needed a system that would be able to transport optically cooled atoms from the UHV MOT region to the UHV trap with a minimum of losses or heating. Two techniques had been tested in the literature and shown to be extremely efficient: the moving quadrupole trap used at NIST [184] and the magnetic transport system developed by the Munich group [183]. We chose the former for our system as we felt it had a good combination of simplicity and utility. Our current implementation uses a computer controlled PI M-521 20cm high precision linear translation stage to move a low profile, low current (10 A) quadrupole trap from UHV MOT to IP magnetic magnetic trap (a distance of approximately 15cm - which can be covered by the translation stage in just over 1 second). The UHV MOT and magnetic trap are situated in the same glass cell, a specially made 20 cm by 3cm by 3cm unit from Starna UK. The glass walls are 5mm thick and hence the biggest MOT beams we can use are 2cm in diameter. We use the same optical system as previously described in this thesis. The lasers in the horizontal plane are oriented at 45 degrees to the glass cell (which is not AR coated) and the vertical laser is retro-reflected from a mounted quater-wave plate and mirror in the moving quadrupole assembly as shown in figure 6.6. The magnetic trap is essentially the design of configuration 2 in the previous section. It is water cooled by a temperature stabilized recirculating system and is run continuously, turning off only for the atoms to be delivered by the moving coil assembly or for imaging. Imaging is in the horizontal plane perpendicular to the weak axis of the magnetic trap. The UHV MOT is loaded from a vapor cell $2D^+$ MOT.

The vacuum system is extremely simple and is based on the observation that in our previous machine, a pressure difference of approximately three orders of magnitude was maintained purely by the 0.3 l/s impedance between vapour cell collection MOT and the UHV system. The vapour cell pump in the old machine has not run for three years yet we see no adverse effects on the lifetime of atoms in the UHV magnetic trap (greater than 60 seconds). In addition, we have used our titanium sublimation pump only twice (both times more than three years ago). Hence, it, as well as the vapour cell ion pump, both appear to be non essential to achieving the UHV required for BEC experiments. The new vacuum system consists of a single 40 l/s ion pump attached by a standard length nipple to a 2.75" 6 way cube cross which forms the core of the assembly. Two UHV compatible optical quality glass cells are attached on opposite sides of the cross in the horizontal plane. The UHV MOT and magnetic trap are arranged around a 20 cm by 3 cm by 3 cm cell which is pumped directly by the 40 l/s ion pump. The other 10 cm by 3 cm by 3 cm vapor cell holds a $2D^+$ MOT which provides a very high flux atomic beam for loading the UHV MOT [105]. The $2D^+$ MOT is differentially pumped by a 0.3

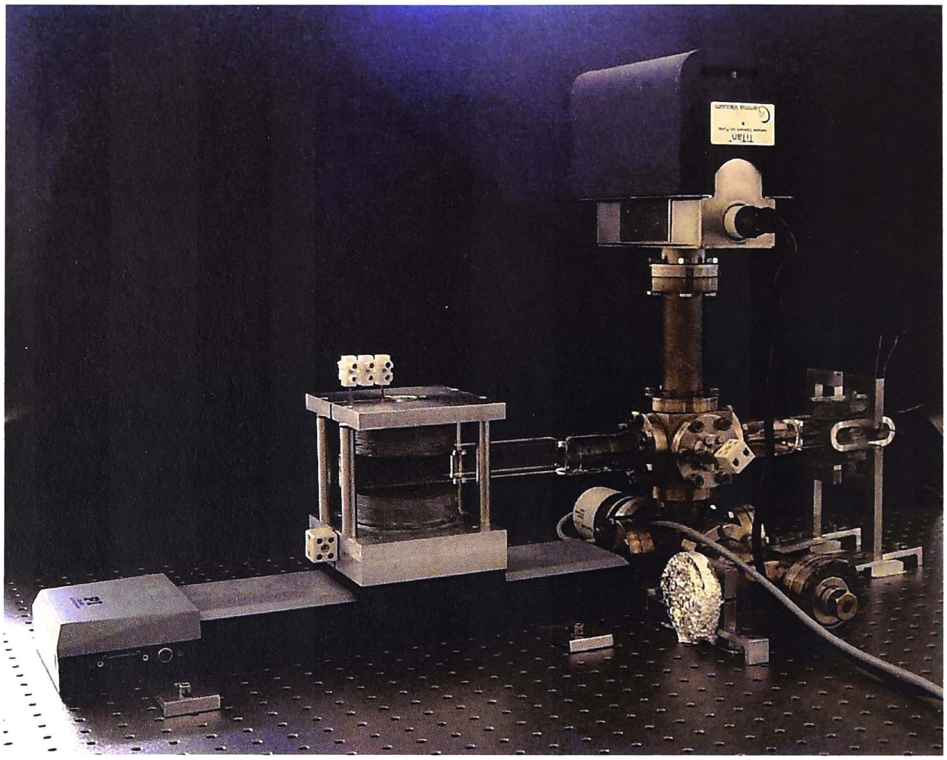

Figure 6.6: Construction of the new vacuum system described in this section.

l/s impedance. The impedance is constructed as follows. A solid copper gasket has three holes drilled in it; a one cm hole in the centre and two small holes to allow enamelled copper wire to supply a single SAES Rb dispenser with current. A 10 cm long stainless steel tube (external diameter 1 cm internal 7 mm) threaded at one end and with a highly polished 45 degree surface and an 0.8 mm hole at the other is attached by stainless steel nuts to the gasket. The only pumping to the vapor cell is through the 0.8 mm hole and the very small clearances of the feed-throughs on the gasket. A five way cross is attached to the lower flange of the cube cross and holds a vacuum feed-through, cold cathode gauge and UHV valve (to facilitate turbo pump connection for baking).

CHAPTER 7

Conclusions and outlook.

In order to study an atom laser, it is necessary to first create a source of condensed atoms. Chapter 3 of this thesis presents the design and construction of the optical cooling, magnetic trapping, and imaging systems necessary to achieve and accurately measure BEC. The final section of Chapter 3 presents our evidence for BEC in the new machine. In Chapter 6, our techniques for magnetic trapping were developed further, with the optimisation of a QUIC magnetic trap to produce a magnetic potential with a bias field of 0.8G, and axial and radial trapping frequencies, $\omega/2\pi$, for ^{87}Rb $m_F = 2$ of 20.9 Hz and 249 Hz respectively, while dissipating only 50 W. This highly stable trap will facilitate our future precision studies of atom lasers. The ultimate goal of this research, which extends beyond the scope of this thesis, is to create a trap suitable for the production of a continuously pumped atom laser.

In Chapters 4 and 5 we showed, experimentally, using a pulsed atom laser in the strong coupling regime, and theoretically, using a model of a pumped atom laser in the weak coupling regime, that the output flux of an atom laser is 'classically' noisy. This presents an immediate experimental challenge: can we reduce the classical noise of the atom laser, while at the same time producing a high flux output? Clearly, developing a continuous pumping mechanism would increase the flux, but this could be at the expense of a noisy output beam.

A number of recent theoretical studies have indicated that various forms of feed back can reduce the classical noise that results from collective oscillations of the trapped condensate due to pumping and output coupling [185, 186, 187]. These schemes rely on a measurement of fluctuations in the condensate and the output atom laser beam, both of which will need to be 'non-destructive'. By non-destructive we mean that while the stabilisation circuit is active, the atom laser beam can still be used in experiments (in analogy with active intensity stabilisation of an optical laser). Hence, the near future of atom laser research lies in the development of three key technologies; minimally destructive detection, feedback, and continuous pumping. Minimally destructive detection refers to the need to go beyond the current generation of detection systems. At present, far detuned phase contrast imaging on CCD cameras represents the cutting edge of BEC imaging technology [53]. Recent theoretical work by our group has shown that there are only two ways in which the signal-to-noise ratio of detection techniques (at fixed destruction) can go beyond current technology [176]. High finesse optical cavities and squeezed light both provide a clear path to fundamentally better detectors. However, their implementation represents a significant experimental challenge. On the other hand, new *dynamic* measurement devices based on interferometric systems operating at the current limits of destruction, will allow continuous detection of atom laser beams for use in feedback circuits, in the near future [188]. This in itself will represent an important step forward for the coherent atom optics of alkali atoms.

Experimentally, continuous pumping of the atom laser is a hard problem for a relatively straightforward reason. The most efficient way of cooling atoms from room temperature to the μK regime is with resonant light [38]. The only way, to date, to achieve BEC, is through forced RF evaporative cooling. In creating a BEC, one must first optically pre-cool and then transfer atoms into a magnetic trap. All the pre-cooling light must be thoroughly extinguished, otherwise the magnetically trapped atoms will quickly be lost; a single photon absorption is enough to raise the energy of an atom above the magnetic trap depth. Hence the loading of atoms and the holding and cooling of atoms cannot, in general, occur simultaneously, either temporally or spatially. Two schemes have been demonstrated that overcome this limitation in traditional BEC setups, both by using shutters in ultra-high vacuum [64, 183] to optically isolate the magnetic or optical trapping and optical loading stages of the experiment. The group at Laboratoire Kastler Brossel in Paris have made significant progress towards implementing a continuous atomic laser by evaporative cooling in a magnetic waveguide continuously loaded from a 2D-MOT [65, 66, 67]. For traditional BEC machines, such as described in this thesis, it is likely that non-resonant optical loading techniques, based on traveling wave dipole traps [189, 190, 191], hold the key to continuous replenishment of the condensate [192].

In conclusion, the continuous detection, feedback, loading, and cooling mechanisms for an atom laser are the next challenges that the field of atom laser research must meet.

APPENDIX A

Atomic tilt locking

We demonstrate novel modulation-free frequency locking of a diode laser, utilising a simple Sagnac interferometer to create an error signal from saturated absorption spectroscopy. The interference condition at the output of the Sagnac is strongly effected by the sharp dispersion feature around an atomic resonance. Slight misalignment of the interferometer and subsequent spatially selective, or tilt, detection allows this phase change to be converted into an error signal. Tilt locking has significant advantages over previously described methods, as it requires only a small number of low cost optical components and a detector. In addition the system has the potential to be constructed as a plug and play fibre-coupled monolithic device to provide sub-MHz stability for lasers in the commercial market.

A.1 Background

The locking of lasers to narrow atomic or cavity resonances is a prerequisite for many experiments in physics and precision industrial applications. In particular, saturated-absorption spectroscopy (SAS) is almost synonymous with frequency stabilisation of diode lasers in atomic physics in applications such as atomic clocks, laser cooling and Bose-Einstein condensation. Several methods for obtaining an error signal from an atomic transition are in common use. These generally rely on modulation of either the laser frequency or atomic reference source and subsequent electronic demodulation to produce the error signal required for locking [193]. More recently, modulation-free differencing techniques have come into use [194, 195, 196], whereby an error signal is produced by subtracting two frequency or phase shifted signals generated from the same atomic reference source. Modulation free schemes have the advantage of simplicity over more traditional methods as they potentially do away with the need for lock-in electronics and various modulation apparatus. The benefit is two-fold, a simplified experimental setup, and a reduction in broadening effects on the frequency reference and/or laser. To date, however, modulation free schemes have generally either included expensive apparatus such as acousto-optic modulators, strong magnetic fields leading to broadening of the atomic transition, or are very sensitive to alignment and vibration.

A.2 Tilt locking

In this appendix we present a novel differencing technique that combines the precision of spectroscopy with the sensitivity of interferometry to produce a robust, zero crossing error signal from an atomic transition. Our scheme is modulation and Doppler free, polarisation independent, requires no lock-in amplifier and consists of only a photodetector, gas cell and inexpensive optical components. We place a vapour cell and neutral density filter within a Sagnac interferometer (Fig A.1.). We use the Sagnac configuration because it is interferometrically insensitive to environmental drift due to the optical beams traveling the same path in opposite directions. The pump beam saturates the vapour cell and is then attenuated, while the probe beam is first attenuated and then probes the saturated transitions of atoms in the vapour cell. Upon recombination at the Sagnac beam splitter, both beams have experienced the linear absorption of the vapour cell and neutral density filter, while only the probe is amplitude and phase modified due to the Doppler free resonance it alone encounters. We use this Doppler-free phase shift to produce an interferometric error signal at the Sagnac output, achieved through the use of Tilt locking [197]. This scheme was originally conceived in relation to optical cavities, however, the concept of Tilt locking can be extended to two beam interferometers [198]. The output of a Sagnac, or any two beam interferometer, can be described in the basis of TEM modes, as can a cavity. In the case of a Sagnac, a TEM_{00} mode incident on the input of the interferometer will result in a dark output. If the interferometer is misaligned to produce a tilt error on recombination at the beamsplitter, the output will be a TEM_{01} mode that is $\pi/2$ out of phase with the original beams. Any phase shift introduced within the interferometer will lead to a power mismatch between the beam halves due to constructive interference between the TEM_{00} mode and TEM_{01} mode in one half of the beam while producing destructive $\text{TEM}_{00}/\text{TEM}_{01}$

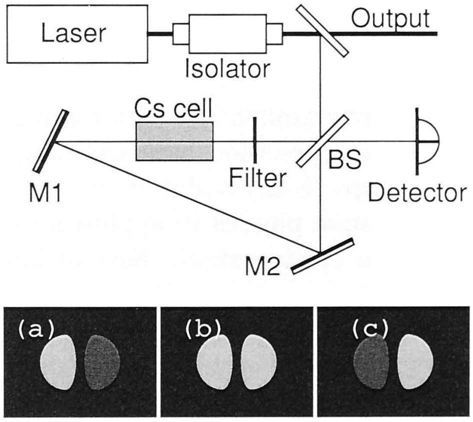

Figure A.1: The experimental setup for Tilt locking to an atomic transition. (a)-(c) illustrate the effect on the relative intensity of the beam halves of scanning across an atomic resonance.

interference in the other half.

A.3 Atomic phase shift

It is well known that associated with an atomic absorption feature there is also a sharp change in $n(x)$, the refractive index of the atoms [199], which in turn affects the phase of the interacting light. The phase change associated with the absorption feature can be expressed as

$$\phi = \frac{2\pi\nu}{c}\int_{-\infty}^{\infty}[n(x)-1]dx \tag{A.1}$$

where ν is the frequency of the light and x is the coordinate along the beam propagation path. The integral is taken over the length of the interaction region. The refractive index, $[n(x)-1]$, has a typical dispersive form with the zero crossing coinciding with the peak in absorption. By placing a vapour cell inside the interferometer, the phase change associated with a resonance and its resultant effect on the output of the interferometer can be used to frequency stabilize a laser, as described in the previous paragraph. This effect is shown schematically in Fig A.1(a)-(c). As the laser frequency is scanned across the atomic resonance, the phase shift induced by the Doppler-free atomic dispersion inside the interferometer adds or subtracts to the phase of the TEM$_{01}$ mode resulting in an intensity mismatch in the lobes. The magnitude of the phase shift is directly proportional, in sign and magnitude, to the detuning of the laser frequency with respect to the atomic resonance.

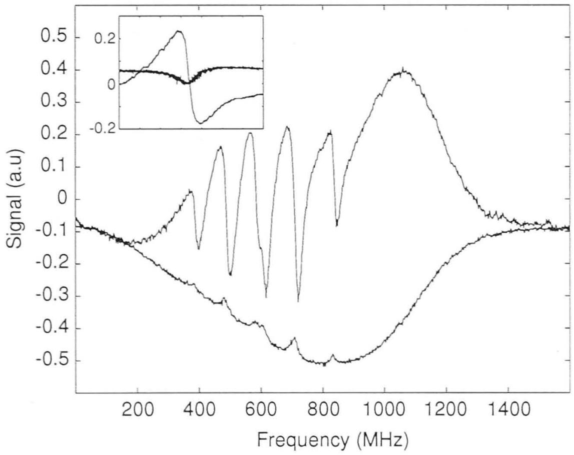

Figure A.2: Measured Cs $6^2S_{1/2}, F=4 \rightarrow 6^2P_{3/2}$ saturated absorption and error signals generated by the interferometer tilt locking system. We used spatial mode filtering via an optical fibre (ThorLabs TS-PM-4621) to provide a clean TEM$_{00}$ input to the interferometer. The inset shows the same information acquired from the $6^2S_{1/2}, F=4 \rightarrow 6^2P_{3/2}, F=5$ transition.

A.4 Experimental setup and results

Our experimental setup is shown in Fig. A.1. The laser is a 100mW SDL-5700-TO3 DBR diode operating at 852 nm. A small portion of the beam is split off and passed through a two mirror Sagnac interferometer. A cesium vapour cell and neutral density filter are placed inside the interferometer. In this configuration, the counter clock-wise beam passing through the filter before the cell acts as a probe, and the clock-wise beam as the pump, creating the conditions for Doppler-free saturated-absorption spectroscopy [200]. We typically used between 0.1 and 2 mW of power incident on the input port, with a beam diameter of $\approx$1mm and a filter with transmisivity 0.1. A simple CCD camera was used to check the output of the interferometer for coarse alignment of the dark port and tilt mode. The tilt output of the interferometer is achieved by misaligning the beamsplitter (or one of the mirrors) on the horizontal axis until the dark port changes to a clearly visible TEM_{01} mode. The detector is a commercial quadrant photodiode (EG&G C30843E) with the quadrants appropriately added to produce a vertically split two lobed tilt detector. The output of the lobes is then summed or subtracted allowing both the saturated-absorption and error signals to be monitored simultaneously. Finally, the error signal is amplified and passed to a servo-locking circuit which feeds back to the laser diode current.

A typical signal from the interferometer is shown in Fig. A.2. The transition is the Cs $6^2S_{1/2}, F = 4 \rightarrow 6^2P_{3/2}$ used for laser cooling. An extraordinary feature of our method is the large signal-to-noise ratio of the true zero crossing error signal, generated without the use of any modulation of the laser light or atoms. The inset shows the laser scan across the Cs $6^2S_{1/2}, F = 4 \rightarrow 6^2P_{3/2}, F = 5$ transition, illustrating the true zero crossing nature of the error signal. Once the system is operating, the error signal is insensitive to intensity fluctuations of the laser beam, and is strikingly immune to acoustic perturbations.

Figure A.3 shows the results of a simple analytic model of both the saturated absorption (a) and the resulting tilt locked error signal (b). In this model, we explicitly derive the real and imaginary coefficients for the complex refractive index for each transition within the Cs $6^2S_{1/2}, F = 4 \rightarrow 6^2P_{3/2}$ hyperfine manifold and then cascade these transitions before calculating the total complex refractive index as a function of optical frequency. Propagation around the Sagnac and through the Cs cell in one direction (pump) yields the Doppler broadened absorption spectrum while propagation in the other direction (probe) yields the saturated absorption spectrum. These two fields are then subtracted at the Sagnac dark fringe (π out of phase) output. We then vectorially add the tilt fields (at $\pi/2$ and $-\pi/2$ phase respectively) on each half of the output plane to give the resulting tilt error signal. The effects of polarization on population pumping have been included by matching the transition strengths to the experimental spectrum. This model gives a zero crossing error signal for each hyperfine transition (transitions 3 and 4 are almost merged).

In Fig. A.4 we show the error signal of a single laser as a function of time, the system is locked at t=20 seconds. Two lasers locked using this technique run our

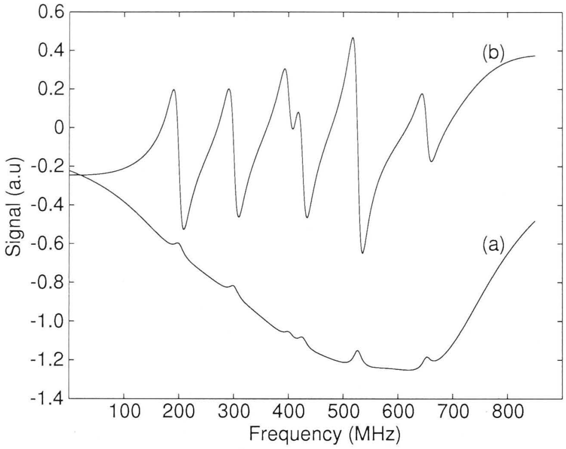

Figure A.3: Theoretical prediction of the Cs $6^2S_{1/2}, F = 4 \rightarrow 6^2P_{3/2}$ saturated absorption, (a), and error signals, (b) generated by the interferometer tilt locking system.

Cesium magneto-optical trap. The system runs over many hours without resetting of the lasers, indicating at least MHz frequency stability of each laser. In addition to this confirmation of the lock point stability, we have also made a heterodyne beat measurement of two independently tilt locked lasers. One laser is locked to the $F = 4 \rightarrow F = 4/5$ crossover 125MHz to the red of the second laser which is locked directly to the $F = 4 \rightarrow F = 5$ transition. The first laser is down shifted with an AOM by 64MHz. The beat signal at 189MHz, shown in the inset to Fig. A.4, is detected on an RF photodiode, fed to a spectrum analyzer (HP 8568B) and then to a computer data logger. We find that the center frequency is stable to the sub-MHz level indefinitely. The laser linewidth of our diodes is measured to be 5MHz. This linewidth is consistent with measurements made using our old locking techniques, and is not due to the tilt locking mechanism. The bandwidth of our servo-locking circuit is 100 Hz, providing good low frequency control of the central laser frequency, but has no effect on fast dynamics which determine the laser linewidth. A precise study of the noise properties of this atomic tilt locking system will be the subject of future work.

A.5 Conclusion

In conclusion we have developed a simple modulation free system for frequency stabilising a diode laser to an atomic transition. Our methods require no expensive components such as AOMs, EOMs, waveplates, or lock-in amplifiers. In addition we envisage that the system can be easily miniaturised as a monolithic structure to provide a fibre coupled device that requires no alignment and is able to provide robust sub-MHz frequency stability for diode lasers.

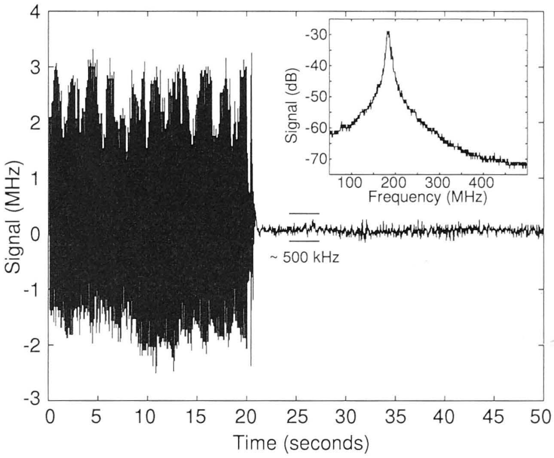

Figure A.4: Calibrated time trace of the interferometer error signal for a single laser; at 20 seconds the servo-lock is turned on. The inset shows the stabilised beat signal between two tilt locked lasers, which we have measured to be sub-MHz stable over many hours. The linewidth of this beat is measured to be 8MHz at the 3dB point with a resolution bandwidth of approximately 100 kHz. This width is to be expected from our lasers as discussed in the text.

APPENDIX B

Numerical Methods

B.1 Overview of the chapter

The research presented in some of Chapter 4 (Figure 4.6) and Chapter 5 of this thesis relies heavily on numerical methods, in both the generation of solutions of the GP equations and in the analysis of the resulting data. In this chapter we will review the general numerical scheme that we use to solve the system of model equations.

The Gross-Pitaevskii equation for the macroscopic wavefunction of a BEC is a partial differential equation of the generalised Nonlinear Schrödinger equation (NLS) type. The NLS equation has found particular application in the field of nonlinear optics, and hence there has been a rather massive body of work published on its analytic and numerical solutions. Although many of the NLS modifications (including complex equations with gain and loss) have been shown to lend themselves to analytical solution, only the one dimensional NLS equation,

$$-i\frac{\partial\Psi(x,t)}{\partial t}=\frac{1}{2}\frac{\partial^2\Psi(x,t)}{\partial x^2}+\Psi(x,t)|\Psi(x,t)|^2, \tag{B.1}$$

is completely integrable. In the case of this thesis we are investigating a significantly more complex system of coupled equations and hence a numerical approach is required.

Approaches to solving the NLS and associated equations are typically divided into two categories: finite difference methods [201] and pseudo-spectral method. Generally speaking pseudo-spectral methods have been found to be faster by an order of magnitude while still achieving the same level of accuracy [175]. A specific pseudo-spectral method that has found wide application in nonlinear dispersive systems (such as the system we consider in this thesis) is the split-step Fourier method [202]. This chapter will describe briefly how this method works and present its application to the system considerated in Chapter 5. To illustrate the main principles of the scheme, we will use Eq. (B.1).

B.2 The split-step Fourier method

B.2.1 The approximation

In order to understand how the split step method works it is useful to rewrite the Eq. (B.1) in the form

$$\frac{\partial \Psi}{\partial t} = (\hat{D} + \hat{N})\Psi, \tag{B.2}$$

where, in general, $\hat{D}$ is a differential operator and $\hat{N}$ accounts for effects such as non-linearities and potentials. This equation has an exact solution, if $\hat{N}$ is independent of t, given by

$$\Psi(t + \Delta t, x) = e^{\Delta t(\hat{D}+\hat{N})}\Psi(t, x) \tag{B.3}$$

In the split operator method we obtain an approximate solution by assuming that the operators act independently on Ψ. In effect, we break the time interval Δt in two. We then have

$$\Psi(t + \Delta t, x) \approx e^{\Delta t\hat{D}} e^{\Delta t\hat{N}} \Psi(t, x) \tag{B.4}$$

Utilising the Baker-Hausdorff formula for non-commuting operators,

$$e^{\Delta t\hat{D}} e^{\Delta t\hat{N}} \approx e^{\left[\Delta t\hat{D}+\Delta t\hat{N}+\frac{\Delta t^2}{2}[\hat{D},\hat{N}]+\frac{\Delta t^3}{12}[\hat{D}-\hat{N},[\hat{D},\hat{N}]]\ldots\right]}, \tag{B.5}$$

where $[\hat{D}, \hat{N}] = \hat{D}\hat{N} - \hat{N}\hat{D}$, we see that the split operator method ignores the non-commuting nature of the operators, the dominant error coming from the commutator $(1/2)\Delta t^2[\hat{D}, \hat{N}]$. Hence the errors in the split operator method are of the order $O(\Delta t^2)$.

B.2.2 Implementation for a generic NLS equation

Implementation of the Eq. (B.4) is straightforward. The execution of the first operator, $e^{\Delta t\hat{N}}$, is equivalent to advancing the solution using only the nonlinear part of Eq. (B.1):

$$i\frac{\partial \Psi(x, t)}{\partial t} = |\Psi(x, t)|^2\Psi(x, t) \equiv \hat{N}\Psi(x, t). \tag{B.6}$$

This can be solved exactly to yield

$$\Psi(x, \Delta t) = e^{i|\Psi(x,0)|^2\Delta t}\Psi(x, 0), \tag{B.7}$$

where $\Psi(x, \Delta t)$ is a solution of Eq. (B.6) and $\Psi(x, 0)$ is the solution of Eq. (B.1) at $t = 0$. The execution of the second operator, $e^{\Delta t\hat{D}}$, makes use of the discrete Fourier transforms:

$$\begin{aligned}
\Psi(k, t) &= F\Psi = \frac{1}{\sqrt{N}}\sum_k \Psi(x_j, t)e^{-ix_jk}, \\
\Psi(x_j, t) &= F^{-1}\hat{\Psi} = \frac{1}{\sqrt{N}}\sum_k \hat{\Psi}(k, t)e^{ix_jk},
\end{aligned} \tag{B.8}$$

where $k = -N/2, \ldots, -1, 0, 1, \ldots, N/2 - 1$. To advance the solution according to

$$-i\frac{\partial\Psi(x,t)}{\partial t} = \frac{1}{2}\frac{\partial^2\Psi(x,t)}{\partial x^2} \equiv \hat{D}\Psi(x,t), \tag{B.9}$$

we perform the Fourier transform of $\Psi(x,t)$, substitute the result into Eq. (B.9) and solve for $\Psi(k, t + \Delta t)$. The resulting wavefunction is found as

$$\Psi(x_j, t + \Delta t) = F^{-1}(e^{-ik^2\Delta t} F(\Psi(x_j, t))). \tag{B.10}$$

Equations (B.7) and (B.10) are repeatedly applied to the wavefunction $\Psi(x,0)$ to solve the initial value problem for the field at any later time. The accuracy of the method can be increased to third order in the temporal step size by including the effect of the nonlinearity in the middle of the propagation segment $(t + \Delta t)$, effectively symmetrising the split operator. In this case the procedure in Eq. (B.4) is replaced by

$$\Psi(x, t + \Delta t) \approx e^{\frac{1}{2}\Delta t\hat{D}} e^{\Delta t\hat{N}} e^{\frac{1}{2}\Delta t\hat{D}} \Psi(x,t). \tag{B.11}$$

Hence, in practice, we repeatedly evolve the system according to the following: for time $\Delta t/2$ use only the differential operator, Eq. (B.10), then multiply by the nonlinear term as in Eq. (B.7) – this represents the effect of the nonlinearity over a whole timestep Δt – and finally use the differential term over $\Delta t/2$ once again.

B.2.3 Split-step scheme for the atom laser model

Generalisation of the split operator method to two coupled NLS equations is relatively straightforward. A complicating factor that must be taken into account when attempting the numerical solution of the system (5.1) is that it includes time dependent linear coupling terms. In this case Eq. (B.6) for each of the fields Ψ_a and Ψ_b has the form

$$i\frac{\partial\Psi_{a,b}}{\partial t} = \hat{N}_{a,b}\Psi_{a,b} + \hat{L}(\Psi_{b,a}), \tag{B.12}$$

where $\hat{L}$ is a linear time-dependent operator. This equation can no longer be solved exactly. We replace the exact step (B.7) with a single 4th-order Runge-Kutta [149] step which can be represented by

$$\begin{aligned} A &= \hat{N}(\Psi_0)\Delta t, \\ B &= \hat{N}(\Psi_0 + \frac{1}{2}A)\Delta t, \\ C &= \hat{N}(\Psi_0 + \frac{1}{2}B)\Delta t, \\ D &= \hat{N}(\Psi_0 + C)\Delta t, \\ \Psi_1 &= \Psi_0 + \frac{1}{6}(A + 2B + 2C + D). \end{aligned} \tag{B.13}$$

Additionally, the two NLS-type equations in our model are coupled to the ODE for the pumping mechanism. To incorporate this into our numerical scheme we assume that $N_u(t)$ changes slowly over Δt, and thus assume it is constant over the single integration step for $\Psi_{a,b}$. At the end of each time step, $N_u(t + \Delta t)$ is calculated using the function $\Psi_a(x, t + \Delta t)$ and then used to advance $\Psi_{a,b}$ by next time step.

Another problem that we face in our numerical simulations is that we want to investigate the behaviour of the output *beam*. This poses two problems. The first is that as the atoms fall away from the condensate they are accelerated by gravity and hence their de Broglie wavelength decreases. This requires that the spatial numerical grid be made more *fine* to control numerical instabilities caused by high frequency Fourier components of the solution. The second problem is that as the beam travels away from the condensate we will need to increase the numerical grid *size*. If the beam interacts with the boundary of the grid the numerical scheme will break down, as it requires periodic boundary conditions. These two problems can be solved to some extent by the inclusion of a boundary absorber (BA) into the scheme. This is a numerical device that reduces the field to zero as it approaches the boundary of the spatial grid, without affecting accurate solution of the system away from the boundary. Using this method we can restrict our numerical grid to a region around the condensate, while still being able to observe the solution of the condensate and output fields at very long times (seconds). We use a simple exponential function added to the Runge-Kutta scheme, in which we can vary the strength of the absorber and the position at which it "turns on". However the reader should note that different numerical "beam-propagation" schemes may require different approaches to tackle the near-boundary regions.

Bibliography

[1] M. H. Anderson, J. R. Ensher, M. R. Matthews, C. E. Wieman, E. A. Cornell, Observation of Bose-Einstein condensation in a dilute atomic vapor. *Science*, **269** 198-201 (1995); K. B. Davis, M-O. Mewes, M. R. Andrews, N. J. van Druten, D. S. Durfee, D. M. Kurn, W. Ketterle. Bose-Einstein condensation in a gas of sodium atoms. *Phys. Rev. Lett.*, **75** 3969-3973 (1995); C. C. Bradley, C. A. Sackett, J. J. Tollett, R. G. Hulet. Evidence of Bose-Einstein condensation in an atomic gas with attractive interactions. *Phys. Rev. Lett.*, **75** 1687-1690 (1995), see also **78** 985 (1997).

[2] T. H. Maiman, Optical and Microwave-Optical Experiments in Ruby, *Phys. Rev. Lett.*, **4** 564-566 (1960). T. H. Maiman, *Nature*, **187** 493 (1960).

[3] M-O. Mewes, M. R. Andrews, D. M. Kurn, D. S. Durfee, C. G. Townsend, W. Ketterle. Output coupler for Bose-Einstein condensed atoms. *Phys. Rev. Lett.*, **78** 582-585 (1997).

[4] E. W. Hagley, L. Deng, M. Kozuma, J. Wen, K. Helmerson, S. L. Rolston, and W. D. Phillips. A Well-Collimated Quasi-Continuous Atom Laser. *Science* **283** 1706-1709 (1999).

[5] I. Bloch, Th. W. Hansch, and T. Esslinger. Atom Laser with a cw Output Coupler. *Phys. Rev. Lett.*, **82** 3008-3011 (1999).

[6] M. Köhl, T. W. Hänsch, and T. Esslinger, Measuring the Temporal Coherence of an Atom Laser Beam, *Phys. Rev. Lett.*, **87** 160404 (2001).

[7] M. Köhl, T. W. Hänsch, and T. Esslinger, Continuous detection of an atom laser beam, *Phys. Rev. A*, **65** 021606(R) (2002).

[8] S. L. Rolston and W. D. Phillips, Nonlinear and quantum atom optics, *Nature*, **416** 219 (2002).

[9] A. E. Siegman, *Lasers*, University Science Books, (1986).

[10] I. Bloch, T.W. Hänsch, and T. Esslinger, Measurement of the spatial coherence of a trapped Bose gas at the phase transition, *Nature*, *403* 166 (2000).

[11] M.-O. Mewes, M. R. Andrews, N. J. van Druten, D. M. Kurn, D. S. Durfee, C. G. Townsend, and W. Ketterle, Collective Excitations of a Bose-Einstein Condensate in a Magnetic Trap, *Phys. Rev. Lett.* **77** 988-991 (1996).

[12] A.E. Leanhardt, Y. Shin, A.P. Chikkatur, D. Kielpinski, W. Ketterle, and D.E. Pritchard, Bose-Einstein condensates near a microfabricated surface, *Phys. Rev. Lett.*, **90** 100404 (2003).

[13] W. Zhang, E. M. Wright, H. Pu, and P. Meystre, Fundamental limit for integrated atom optics with Bose-Einstein condensates, *Phys. Rev. A*, **68** 023605 (2003).

[14] Hilmar Oberst, Shigenori Kasashima, Victor I. Balykin, and Fujio Shimizu, Atomic-matter-wave scanner, *Phys. Rev. A*, **68** 013606 (2003).

[15] Immanuel Bloch, Michael Khl, Markus Greiner, Theodor W. Hnsch, and Tilman Esslinger, Optics with an Atom Laser Beam, *Phys. Rev. Lett.*, **87** 030401 (2001).

[16] R. B. Doak, R. E. Grisenti, S. Rehbein, G. Schmahl, J. P. Toennies, and Ch. Woll, Towards Realization of an Atomic de Broglie Microscope: Helium Atom Focusing Using Fresnel Zone Plates, *Phys. Rev. Lett.*, **83** 42294232 (1999).

[17] K. Helmerson, W. Phillips, K. Burnett, and D. Hutchinson. Atom lasers. *Physics World (http://www.physicsweb.org/*, **12** 31-35 (1999).

[18] A. Einstein.*Sitzungsber. Kgl. Preuss. Akad. Wiss*,**1** 3 (1925).

[19] F. W. Sears and G. L. Salinger. *Thermodynamics, Kinetic Theory, and Statistical Thermodynamics.* (Addison-Wesley: 1986).

[20] B. E. A. Saleh and M. C. Teich. *Fundamentals of Photonics.* (John wiley and sons: 1991).

[21] J. J. Sakurai. *Advanced quantum mechanics.* (Addison-Wesley: 1967)

[22] F. Dalfovo, S. Giorgini, L. P. Pitaevskii and S. Stringari, Theory of Bose-Einstein condensation in trapped gases. *Rev. Mod. Phys.* **71** 463-512 (1999).

[23] S. Stenholm. Validity of the Gross-Pitaevskii equation describing bosons in a trap. *Phys. Rev. A*, **57** 2942-2948 (1998).

[24] M. Randeria. BCS - BEC Crossover. *Lecture series, 2000 theoretical summer school in BEC*, ANU, Australia.

[25] J. R. Engelbrecht, M. Randeria, and C. A. R. Sáde Melo, BCS to Bose crossover: Broken-symmetry state, *Phys. Rev. B*, **55** 15153-15156 (1997).

[26] M. Randeria, in Bose-Einstein Condensation, edited by A. Griffin, D. Snoke, and S. Stringari Cambridge University Press, Cambridge, England (1994).

[27] A. Griffin. A brief history of our understanding of BEC: from Bose to Beliaev. In M. Inguscio, S. Stringari, and C. E. Wieman, editors, Bose-Einstein Condensation in Atomic Gases, Proceedings of the International School of Physics Enrico Fermi, Course CXL. IOS Press Ohmsha, 1999. see also *LANL cond-mat/9901123* (1999).

[28] E. A. Cornell, J. R. Ensher, and C. E. Wiseman. Experiments in dilute atomic Bose-Einstein condensation. In M. Inguscio, S. Stringari, and C. E. Wieman, editors, Bose-Einstein Condensation in Atomic Gases, Proceedings of the International School of Physics Enrico Fermi, Course CXL. IOS Press Ohmsha, 1999. see also *LANL cond-mat/9903109* (1999).

[29] C. E. Hecht. *Physica*, **25** 1159 (1959).

[30] I. F. Silvera and J. T. M. Walraven. Stabilization of atomic hydrogen at low temperature. *Phys. Rev. Lett.*, **44** 164-168 (1980).

[31] D. E. Pritchard. Cooling neutral atoms in a magnetic trap for precision spectroscopy. *Phys. Rev. Lett.*, **51** 1336-1339 (1983).

[32] H. F. Hess. Evaporative cooling of magnetically trapped and compressed spin-polarized hydrogen. *Phys. Rev. B.*, **34** 3476-3479 (1986).

[33] T. W. Hansch and A. L. Schawlow. Cooling of gases by laser radiation. *Opt. Commun.*, **13** 68-69 (1975).

[34] A. Ashkin. Trapping of Atoms by Resonance Radiation Pressure. *Phys. Rev. Lett.*, **40** 729-732 (1978)

[35] D. J. Wineland, R. E. Drukkinger and F. L. Walls. Radiation-pressure cooling of bound resonant absorbers. *Phys. Rev. Lett.*, **40** 1639-1642 (1978).

[36] S. Chu, L. Hollberg, J. E. Bjorkholm, A. Cable, A. Ashkin. Three-dimensional viscous confinement and cooling of atoms by resonance radiation pressure. *Phys. Rev. Lett.*, **55** 48-51 (1985).

[37] S. Chu. The manipulation of neutral particles. *Rev. Mod. Phys.*, **70** 685-706 (1998); C. N. Cohen-Tannoudji. Manipulating atoms with photons. *Rev. Mod. Phys.*, **70** 707-719 (1998); W. D. Phillips. Laser cooling and trapping of neutral atoms. *Rev. Mod. Phys.*, **70** 721-741 (1998).

[38] E. L. Raab, M. Prentiss, A. Cable, S. Chu, D. E. Pritchard. Trapping of neutral sodium atoms with radiation pressure. *Phys. Rev. Lett.*, **59** 2631-2634 (1987).

[39] E. A. Cornell and C. E. Wieman Bose-Einstein condensation in a dilute gas, the first 70 years and some recent experiments, *Rev. Mod. Phys.*, **74** 875-893 (2002);

W. Ketterle, When atoms behave as waves: Bose-Einstein condensation and the atom laser, *Rev. Mod. Phys.*, **74** 1131-1151 (2002).

[40] C. Wieman, G. Flowers and S. Gilbert. Inexpensive laser cooling and trapping experiment for undergraduate laboratories. *Am. J. Phys.*, **63** 317-330 (1995).

[41] H. M. Wiseman and M. J. Collett. An atom laser based on dark-state cooling. *Phys. Lett. A*, **202**, 246-252 (1995).

[42] H. M. Wiseman. Defining the (atom) laser. *Phys. Rev. A*, **56** 2068-2084 (1997).

[43] O. Svelto. *Principles of Lasers.* (Plenum Press: 1989).

[44] L. Mandel and E. Wolf. *Optical coherence and quantum optics.* (Cambridge University Press: 1995)

[45] R. J. Glauber, The Quantum Theory of Optical Coherence, *Phys. Rev.*, **130** 2529 (1963); R. J. Glauber, Coherent and Incoherent States of the Radiation Field, *Phys. Rev.*, **131** 2766 (1963); M. Naraschewski and R. J. Glauber. Spatial coherence and density correlations of trapped Bose gases. *Phys. Rev. A*, **59** 4595-4607 (1999).

[46] H. M. Wiseman, Light amplification without stimulated emission: Beyond the standard quantum limit to the laser linewidth, *Phys. Rev. A*, **60** 4083-4093 (1999)

[47] H. M. Wiseman and John A. Vaccaro, Atom lasers, coherent states, and coherence. I. Physically realizable ensembles of pure states, *Phys. Rev. A*, **65** 043605 (2002).

[48] A. L. Schawlow and C. H. Townes Infrared and Optical Masers *Phys. Rev.*, **112** 1940 (1958).

[49] J. P. Gordon, H. J. Zeiger and C. H. Townes The maser - new type of microwave amplifier, frequency standard and spectrometer. *Phys. Rev*, **99** 1264 (1955).

[50] M. Köhl, M. J. Davis, C. W. Gardiner, T. W. Hänsch, and T. Esslinger, Growth of Bose-Einstein Condensates from Thermal Vapor, *Phys. Rev. Lett.*, **88** 080402 (2002).

[51] D. S. Petrov, G. V. Shlyapnikov, and J. T. M. Walraven, Phase-Fluctuating 3D Bose-Einstein Condensates in Elongated Traps, *Phys. Rev. Lett.*, **87** 050404 (2001).

[52] S. Dettmer, D. Hellweg, P. Ryytty, J. J. Arlt, W. Ertmer, and K. Sengstock , S. Petrov1,2 and G. V. Shlyapnikov, Observation of Phase Fluctuations in Elongated Bose-Einstein Condensates, *Phys. Rev. Lett.*, **87** 160406 (2001).

[53] W. Ketterle, D. S. Durfee, and D. M. Stamper-Kurn. Making probing and understanding Bose-Einstein condensates. In M. Inguscio, S. Stringari, and C. E. Wieman, editors, Bose-Einstein Condensation in Atomic Gases, Proceedings

of the International School of Physics Enrico Fermi, Course CXL. IOS Press Ohmsha, 1999.

[54] M.-O. Mewes, M. R. Andrews, N. J. van Druten, D. M. Kurn, D. S. Durfee, and W. Ketterle, Bose-Einstein Condensation in a Tightly Confining dc Magnetic Trap, *Phys. Rev. Lett.*, **77** 416419 (1996).

[55] M. J. Holland, D. S. Jin, M. L. Chiofalo, and J. Cooper, Emergence of Interaction Effects in Bose-Einstein Condensation, *Phys. Rev. Lett.*, **78** 38013805 (1997).

[56] D. Hellweg, L. Cacciapuoti, M. Kottke, T. Schulte, K. Sengstock, W. Ertmer, and J. J. Arlt, Measurement of the Spatial Correlation Function of Phase Fluctuating Bose-Einstein Condensates, *Phys. Rev. Lett.*, **91** 010406 (2003).

[57] M. Olshanii, Y. Castin, and J. Dalibard, *Proceedings of the 12th International Conference on Laser Spectroscopy* (World Scientific, Singapore: 1995).

[58] R. J. C. Spreeuw, T. Pfau and M. Wilkens, Laser-like scheme for atomic-matter waves, *Europhys. Lett.*, **32** 469-474 (1995).

[59] G. M. Moy, J. J. Hope, and C. M. Savage, Atom laser based on Raman transitions, *Phys. Rev. A*, **55** 3631-3638 (1997).

[60] M. Holand, K. Burnett, C. Gardiner, J. I. Cirac, and P. Zoller, Theory of an atom laser, *Phys. Rev. A*, **54** R1757-R1760 (1996).

[61] A. M. Guzman, M. Moore, and P. Meystre, Theory of a coherent atomic-beam generator, *Phys. Rev. A*, **53**, 977-984 (1996).

[62] see e.g. XmdS (eXtensible multi-dimensional Simulator) home page, http://www.xmds.org/

[63] P. Treutlein, K. Y. Chung, and S. Chu, High-brightness atom source for atomic fountains, *Phys. Rev. A*, **63** 051401(R) (2001).

[64] A. P. Chikkatur, Y. Shin, A. E. Leanhardt, D. Kielpinski, E. Tsikata, T. L. Gustavson, D. E. Pritchard, and W. Ketterle, A Continuous Source of Bose-Einstein Condensed Atoms, *Science*, **296** 2193 (2002).

[65] C.F. Roos, P. Cren, D. Gury-Odelin and J. Dalibard, Continuous loading of a non-dissipative atom trap, *Europhys. Lett.*, **61** 187-193 (2003).

[66] P. Cren, C.F. Roos, A. Aclan, J. Dalibard and D. Gury-Odelin, Loading of a cold atomic beam into a magnetic guide, *Eur. Phys. J. D*, **20** 107-116 (2002).

[67] E. Mandonnet, A. Minguzzi, R. Dum, I. Carusotto, Y. Castin, J. Dalibard Evaporative cooling of an atomic beam, *Eur. Phys. J. D*, **10** 9-18 (2000).

[68] Dale G. Fried, Thomas C. Killian, Lorenz Willmann, David Landhuis, Stephen C. Moss, Daniel Kleppner, and Thomas J. Greytak, Bose-Einstein Condensation of Atomic Hydrogen, *Phys. Rev. Lett.*, **81** 38113814 (1998)

[69] F. Pereira Dos Santos, J. Lonard, Junmin Wang, C. J. Barrelet, F. Perales, E. Rasel, C. S. Unnikrishnan, M. Leduc, and C. Cohen-Tannoudji. Bose-Einstein Condensation of Metastable Helium, *Phys. Rev. Lett.*, **86** 3459-3462 (2001).

[70] A. Robert, O. Sirjean, A. Browaeys, J. Poupard, S. Nowak, D. Boiron, C. I. Westbrook, and A. Aspect, A Bose-Einstein Condensate of Metastable Atoms, *Science*, **292** 461-464 (2001).

[71] C. C. Bradley, C. A. Sackett, J. J. Tollett, R. G. Hulet. Evidence of Bose-Einstein condensation in an atomic gas with attractive interactions. *Phys. Rev. Lett.*, **75** 1687-1690 (1995), see also **78** 985 (1997).

[72] K. B. Davis, M-O. Mewes, M. R. Andrews, N. J. van Druten, D. S. Durfee, D. M. Kurn, W. Ketterle. Bose-Einstein condensation in a gas of sodium atoms. *Phys. Rev. Lett.*, **75** 3969-3973 (1995);

[73] B. DeMarco and D.S. Jin, Onset of Fermi Degeneracy in a Trapped Atomic Gas, *Science*, **285** 1703 (1999);

G. Modugno, G. Ferrari, G. Roati, R. J. Brecha, A. Simoni, and M. Inguscio, Bose-Einstein Condensation of Potassium Atoms by Sympathetic Cooling, *Science*, **294** 1320-1322 (2001).

[74] M. H. Anderson, J. R. Ensher, M. R. Matthews, C. E. Wieman, E. A. Cornell, Observation of Bose-Einstein condensation in a dilute atomic vapor, *Science*, **269** 198-201 (1995).

[75] . L. Cornish, N. R. Claussen, J. L. Roberts, E. A. Cornell, and C. E. Wieman, Stable 85Rb Bose-Einstein Condensates with Widely Tunable Interactions, *Phys. Rev. Lett.*, **85** 1795-1798 (2000).

[76] Tino Weber, Jens Herbig, Michael Mark, Hanns-Christoph Ngerl, and Rudolf Grimm, *Science*, **299** 232-235 (2002).

[77] Y. Takasu, K. Maki, K. Komori, T. Takano, K. Honda, M. Kumakura, T. Yabuzaki, and Y. Takahashi, Spin-Singlet Bose-Einstein Condensation of Two-Electron Atoms, *Phys. Rev. Lett.*, **91** 040404 (2003).

[78] A.C.Wilson & C.R.Mckenzie. Experimental Aspects of Bose-Einstein Condensation. Bose-Einstein Condensation: from atomic physics to quantum fluids. Proceedings of the 13th Physics Summer School, edited by C.M. Savage and M. Das (World Scientific, Singapore, 2000).

[79] W. Demtröder, *Laser Spectroscopy*, Springer.

[80] Wolfgang Ketterle, Kendall B. Davis, Michael A. Joffe, Alex Martin, and David E. Pritchard, High densities of cold atoms in a dark spontaneous-force optical trap, *Phys. Rev. Lett.*, **70** 22532256 (1993).

[81] M. H. Anderson, W. Petrich, J. R. Ensher, and E. A. Cornell, Reduction of light-assisted collisional loss rate from a low-pressure vapor-cell trap, *Phys. Rev. A*, **50** 3597-3600 (1994).

[82] S. Jochim, M. Bartenstein, A. Altmeyer, G. Hendl, S. Riedl, C. Chin, J. Hecker Denschlag, and R. Grimm, Bose-Einstein Condensation of Molecules, *Science Express*, Published online November 13, 2003;

[83] O. Stern and W. Gerlach, Der experimentelle Nachweis des magnetischen Moments des Silberatoms, *Z. Phys.* **8** 110 (1921).

[84] W. Gerlach and O. Stern, Der experimentelle Nachweis der Richtungsquantelung im Magnetfeld, *Z. Phys.* **9** 349 (1922).

[85] H. Metcalf and P. van der Straten, *Laser Cooling and Trapping*, Springer (2002).

[86] J. Dalibard, C. Cohen-Tannoudji, Laser cooling below the Doppler limit by polarization gradients: simple theoretical models, *J. Opt. Soc. Am. B*, **6** 2023 (1989).

[87] A. Ashkin, J. P. Gordon, Stability of radiation-pressure particle traps: an optical Earnshaw theorem, *Opt. Lett.*, **8** 511 (1983).

[88] G. Breit and I. I. Rabi. Measurement of nuclear spin, *Phys. Rev.*, **38** 2082 (1931).

[89] W. Wing, *Prog. Quant. Elect.*, **8** 181 (1985). see also W. H. Wing. Some problems and possibilities for quasistatic neutral particle trapping. In W. D. Phillips, editor, Proceedings of the Workshop on Spectroscopic Applications of Slow Atomic Beams, volume 653. NBS, Gaithersburg, April 1983.

[90] E. Majorana, *Nuovo Cimento*, **9** 43 (1932) .

[91] C. Zener, Non-adiabatic crossing of energy levels. *Proceedings of the Royal Society of London Series A*, **137** 696 (1932); J. R. Rubbmark, M. M. Kash, M. G. Littman, and D. Kleppner, Dynamical effects at an avoided level crossing: A study of the Landau-Zener effect using rydberg atoms, *Phys. Rev. A*, **23** 3107 (1981).

[92] A. L. Migdall, J. V. Prodan, W. D. Phillips, T. H. Bergeman, and H. J. Metcalf, First Observation of Magnetically Trapped Neutral Atoms, *Phys. Rev. Lett.*, **54** 2596-2599 (1985).

[93] W. Petrich, M. H. Anderson, J. R. Ensher, and E. A. Cornell, Stable, Tightly Confining Magnetic Trap for Evaporative Cooling of Neutral Atoms, *Phys. Rev. Lett.*, **74** 3352-3355 (1995)

[94] D. E. Pritchard. Cooling atoms in a magnetic trap for precision spectroscopy, *Phys. Rev. Lett.*, **51** 1336 (1983).

[95] Dan .M. Stamper-Kurn, Peeking and poking at a new quantum fluid: Studies of gaseous Bose-Einstein condensates in magnetic and optical traps, PhD Thesis, MIT (2000).

[96] J. Söding, D. Guéry-Odelin, P. Desbiolles, G. Ferrari, and J. Dalibard, Giant Spin Relaxation of an Ultracold Cesium Gas, *Phys. Rev. Lett.*, **80** 1869-1872 (1998).

[97] T. Esslinger, I. Bloch, and T. W. Hänsch, Bose-Einstein condensation in a quadrupole-Ioffe-configuration trap, *Phys. Rev. A*, **58** 2664-2667 (1998).

[98] M. D. Barrett, J. A. Sauer, and M. S. Chapman, All-Optical Formation of an Atomic Bose-Einstein Condensate, *Phys. Rev. Lett.*, **87** 010404 (2001).

[99] P. Valkering. Optimization of evaporative cooling of rubidium atoms in a magnetic trap. Masters thesis, University of Utrecht, February (1999).

[100] Peter Kuffna, Honour's thesis, Australian National University (2003).

[101] C. Myatt. Bose-Einstein Condensation Experiments in a Dilute Vapor of Rubidium. PhD thesis, University of Colorado, Boulder, Colorado, (1997).

[102] O. J. Luiten, M. W. Reynolds, and J. T. M. Walraven, Kinetic theory of the evaporative cooling of a trapped gas, *Phys. Rev. A*, **53** 381-389 (1996).

[103] W. Ketterle and N. J. van Druten, Evaporative cooling of trapped atoms, *Advances in Atomic, Molecular, and Optical Physics*, **37** 181 (1996).

[104] E. Arimondo, E. Cerboneschi, and H. Wu, In M. Inguscio, S. Stringari, and C. E. Wieman, editors, Bose-Einstein Condensation in Atomic Gases, Proceedings of the International School of Physics Enrico Fermi, Course CXL. IOS Press Ohmsha, 1999.

[105] Kai Deickmann. Bose-Einstein Condensation with High Atom Number in a Deep Magnetic Trap, PhD thesis, AMOLF (2001).

[106] E. P. Gross, *Nuovo Cimento*, **20** 454 (1961); E. P. Gross, *J. Math. Phys.*, **4** 195 (1963); L. P. Pitaevskii, *Zh. Eksp. Teor. Fiz.*, **40** 646 (1961). [*Sov. Phys. JETP*, **13** 451 (1961).]

[107] Keith Burnett, Finite-temperature effects in Bose-Einstein condensates. Bose-Einstein Condensation: from atomic physics to quantum fluids. Proceedings of the 13th Physics Summer School, edited by C.M. Savage and M. Das (World Scientific, Singapore, 2000).

[108] A. E. Leanhardt, Y. Shin, D. Kielpinski, D. E. Pritchard, and W. Ketterle, Coreless Vortex Formation in a Spinor Bose-Einstein Condensate, *Phys. Rev. Lett.*, **90** 140403 (2003).

[109] W. Ketterle, *Physics Today*, **52** 30 (1999).

[110] M. Edwards and K. Burnett, Numerical solution of the nonlinear Schrödinger equation for small samples of trapped neutral atoms, *Phys. Rev. A*, **51** 13821386 (1995).

[111] B. P. Anderson and M. A. Kasevich, *Science*, **282** 1686 (1998).

[112] J L Martin, C R McKenzie, N R Thomas, D M Warrington and A C Wilson, *J. Phys. B: At. Mol. Opt. Phys.*, **33** 39193927 (2000).

[113] M. W. Jack, M. Naraschewski, M. J. Collett and D. F. Walls, Markov approximation for the atomic output coupler, *Phys. Rev. A*, **59** 2962-2973 (1999).

[114] G. M. Moy, J. J. Hope, and C. M. Savage, Born and Markov approximations for atom lasers, *Phys. Rev. A*, **59** 667-675 (1999).

[115] M. R. Andrews, C. G. Townsend, H.-J. Miesner, D. S. Durfee, D. M. Kurn, and W. Ketterle, Observation of Interference Between Two Bose Condensates, *Science*, **275** 637 (1997).

[116] Y. Le Coq, J. H. Thywissen, S. A. Rangwala, F. Gerbier, S. Richard, G. Delannoy, P. Bouyer, and A. Aspect, Atom Laser Divergence, *Phys. Rev. Lett.*, **87** 170403 (2001).

[117] Giovanni Cennini, Gunnar Ritt, Carsten Geckeler, and Martin Weitz All-Optical Realization of an Atom Laser, *Phys. Rev. Lett.*, **91** 240408 (2003).

[118] M. Edwards, D. A. Griggs, Ph. L. Holman, Ch. W. Clark, S. L. Rolston, and W. D. Phillips, Properties of a Raman atom-laser output coupler, *J. Phys. B: At. Mol. Opt. Phys.*, **32** 2935-2950 (1999).

[119] M. Trippenbach, Y. B. Band, M. Edwards, M. Doery, and P. S. Julienne, L. Deng, M. Kozuma, K. Helmerson, S. L. Rolston, W. D. Phillips, Coherence properties of an atom laser, *J. Phys. B: At. Mol. Opt. Phys.*, **33** 47-54 (2000).

[120] J. J. Hope and C. M. Savage, Mechanical potentials due to Raman transitions, *Phys. Rev. A*, **53** 1697-1701 (1995).

[121] http://www.ripplon.com/BiotSavart/

[122] W. Kohn, Cyclotron Resonance and de Haas-van Alphen Oscillations of an Interacting Electron Gas, *Phys. Rev.*, **123** 1242-1244 (1961)

[123] C. J. Myatt, N. R. Newbury, R. W. Ghrist, S. Loutzenhiser, C. E. Wieman, Multiply loaded magneto-optical trap, *Opt. Lett.*, **21** 290 (1996).

[124] C. J. Dedman, K. G. H. Baldwin, and M. Colla, Fast switching of magnetic fields in a magneto-optic trap, *Rev. Sci. Instrum.*, **72** 4055 (2001).

[125] D. W. Sesko, T. G. Walker, C. E. Wieman, Behavior of neutral atoms in a spontaneous force trap, *J. Opt. Soc. Am. B*, **8** 946 (1991).

[126] M. Kasevich, D. S. Weiss, E. Riis, K. Moler, S. Kasapi, and S. Chu, Atomic velocity selection using stimulated Raman transitions, *Phys. Rev. Lett.*, **66** 22972300 (1991).

[127] K. Gibble, S. Chang, and R. Legere, Direct Observation of s-Wave Atomic Collisions, *Phys. Rev. Lett.*, **75** 26662669 (1995).

[128] Shin Inouye, Manipulating Bose-Einstein condensates with laser light, PhD thesis, MIT (2001).

[129] Special Issue, *J. Opt. Soc. Am. B*, **11** 2020-2270 (1989).

[130] C. G. Townsend, N. H. Edwards, C. J. Cooper, K. P. Zetie, and C. J. Foot A. M. Steane, P. Szriftgiser, H. Perrin, and J. Dalibard, Phase-space density in the magneto-optical trap, *Phys. Rev. A*, **52** 14231440 (1995).

[131] W. Petrich, M. H. Anderson, J. R. Ensher, E. A. Cornell, Behavior of atoms in a compressed magneto-optical trap, *J. Opt. Soc. Am. B*, **11** 1332 (1994).

[132] J. W. Jun, S. Chang, H. S. Lee, V. Minogin, W. Jhe, Double-structure potential due to multiphoton processes in a magneto-optical trap, *Phys. Rev. A*, **60** 47384742 (1999).

[133] I. Guedes, H. F. Silva Filho, and F. D. Nunes, Theoretical analysis of the spatial structures of atoms in magneto-optical traps, *Phys. Rev. A*, **55** 561567 (1997).

[134] Thomas E. Barrett, Samuel W. DaporeSchwartz, Mark D. Ray, and Gregory P. Lafyatis, Slowing atoms with σ-polarized light, *Phys. Rev. Lett.*, **67** 34833486 (1991).

[135] J. Ensher, The First Experiments with Bose-Einstein Condensation of ^{87}Rb, PhD thesis, University of Colorado (1998).

[136] K. B. Davis, M.-O. Mewes, M. A. Joffe, M. R. Andrews, and W. Ketterle, Evaporative Cooling of Sodium Atoms, *Phys. Rev. Lett.*, **75** 2909 (1995).

[137] L. Hartshorn, Radio-frequency measurements, Wiley & Sons Inc. (1940).

[138] J. E. Lye, C.S. Fletcher, U. Kallman, H. -A. Bachor, and J. D. Close, *J. Opt. B, Quantum and Semiclass. Opt.*, **4** 57 (2002).

[139] Y. Castin and R. Dum, Bose-Einstein Condensates in Time Dependent Traps, *Phys. Rev. Lett.*, **77** 53155319 (1996).

[140] K. Bongs, S. Burger, G. Birkl, K. Sengstock, W. Ertmer, K. Rzazewski, A. Sanpera, and M. Lewenstein, Coherent Evolution of Bouncing Bose-Einstein Condensates, *Phys. Rev. Lett.*, **83** 3577-3580 (1999).

[141] M. Kozuma, L. Deng, E. W. Hagley, J. Wen, R. Lutwak, K. Helmerson, S. L. Rolston, and W. D. Phillips, Coherent Splitting of Bose-Einstein Condensed Atoms with Optically Induced Bragg Diffraction, *Phys. Rev. Lett.*, **82** 871-875 (1999).

[142] J. Stenger, S. Inouye, A. P. Chikkatur, D. M. Stamper-Kurn, D. E. Pritchard, and W. Ketterle, Bragg Spectroscopy of a Bose-Einstein Condensate, *Phys. Rev. Lett.*, **82** 45694573 (1999).

[143] M. R. Matthews, D. S. Hall, D. S. Jin, J. R. Ensher, C. E. Wieman, E. A. Cornell, F. Dalfovo, C. Minniti, and S. Stringari, Dynamical Response of a Bose-Einstein Condensate to a Discontinuous Change in Internal State, *Phys. Rev. Lett.*, **81** 243-247 (1998).

[144] E. Hecht, Optics, Addison-Wesley, (1987).

[145] R. J. Ballagh, K. Burnett, and T. F. Scott, Theory of an Output Coupler for Bose-Einstein Condensed Atoms, *Phys. Rev. Lett.*, **78** 1607-1611 (1997).

[146] H. Steck, M. Naraschewski, and H. Wallis, Output of a Pulsed Atom Laser, *Phys. Rev. Lett.*, **80** 1-5 (1998).

[147] W. Zhang and D. F. Walls, Gravitational and collective effects in an output coupler for a Bose-Einstein condensate in an atomic trap, *Phys. Rev. A*, **57** 1248-1252 (1998).

[148] J. Schneider and A. Schenzle, Output from an atom laser: theory vs. experiment, *Appl. Phys. B*, **69** 353-356 (1999).

[149] W. Press, S. Teukolsky, W. Vetterling, and B. Flannery. *Numerical Recipes in C* (Cambridge University Press: 1992) Second Edition.

[150] Jan Max Walter Krüger, Dynamical Behaviour of Radio Frequency Output Couplers for a Bose-Einstein Condensate, MSc., University of Otago (2000).

[151] R. Graham and D. F. Walls, Theory of strong outcoupling from Bose-Einstein condensates, *Phys. Rev. A*, **60** 1429-1441 (1999).

[152] . J. R. Aglin and W. Ketterle, BoseEinstein condensation of atomic gases, *Nature*, **416** 211 (2002).

[153] T. L. Gustavson, P. Bouyer, and M. A. Kasevich, Precision Rotation Measurements with an Atom Interferometer Gyroscope, *Phys. Rev. Lett.*, **78** 2046 (1997).

[154] S. A. Haine, J. J. Hope, N. P. Robins, and C. M. Savage, Stability of Continuously Pumped Atom Lasers, *Phys. Rev. Lett.*, **88** 170403 (2002).

[155] S. A. Haine and J. J. Hope, Mode selectivity and stability of continuously pumped atom lasers, *Phys. Rev. A*, **68** 023607 (2003).

[156] Australian Partnership for Advanced Computing National Facility: http://nf.apac.edu.au/

[157] B.M. Caradoc-Davies, Ph.D. Thesis, Univ. of Otago: http://www.physics.otago.ac.nz/bec2/bmcd/

[158] H. Wiseman, A. Martins and D. Walls, An atom laser based on evaporative cooling, *Quant. Semiclass. Opt.*, **8** 737 (1996).

[159] M. Holland, K. Burnett, C. Gardiner, J. I. Cirac and P. Zoller, Theory of an atom laser, *Phys. Rev. A*, **54** R1757 (1996).

[160] J. J. Hope, G. M. Moy, M. J. Collett and C. M. Savage, Steady-state quantum statistics of a non-Markovian atom laser, *Phys. Rev. A*, **61** 023603 (2000).

[161] B. Kneer, T. Wong, K. Vogel, W. P. Shleich, and D. F. Walls, Generic model of an atom laser, *Phys. Rev. A*, **58** 4841 (1998).

[162] M. Naraschewski, A. Schenzle, and H. Wallis, Phase diffusion and the output properties of a cw atom-laser, *Phys. Rev. A*, **56** 603 (1997).

[163] Y. Japha, S. Choi, K. Burnett, and Y. Band, Coherent Output, Stimulated Quantum Evaporation, and Pair Breaking in a Trapped Atomic Bose Gas, *Phys. Rev. Lett.*, **82** 1079 (1999).

[164] S. Choi, Y. Japha, and K. Burnett, Adiabatic output coupling of a Bose gas at finite temperatures, *Phys. Rev. A*, **61** 063606 (2000).

[165] R.J. Ballagh and C.M. Savage, Bose-Einstein Condensation: from atomic physics to quantum fluids. Proceedings of the 13th Physics Summer School, edited by C.M. Savage and M. Das (World Scientific, Singapore, 2000).

[166] J.A. Armstrong and A.W. Smith, Prog. Opt. VI, 211 (1967).

[167] A. Yariv, Quantum Electronics (Wiley, NY, 1989).

[168] J.E. Lye, B.D. Cuthbertson, H.-A. Bachor, J.D. Close, Phase modulation spectroscopy: a non-destructive probe of Bose-Einstein condensates, *J. Opt. B: Quant. Semiclass. Opt.*, **1** 402 (1999).

[169] Y. B. Band, P. S. Julienne and M. Trippenbach, Radio-frequency output coupling of the Bose-Einstein condensate for atom lasers, *Phys. Rev. A*, **59** 3823 (1999).

[170] E.A. Burt, R.W. Ghrist, C.J. Myatt, M.J. Holland, E.A. Cornell, C.E. Wieman, Coherence, Correlations, and Collisions: What One Learns about Bose-Einstein Condensates from Their Decay, *Phys. Rev. Lett.*, **79** 337 (1997).

[171] Yu. Kagan, A. E. Muryshev, and G. V. Shlyapnikov, Collapse and Bose-Einstein Condensation in a Trapped Bose Gas with Negative Scattering Length, *Phys. Rev. Lett.*, **81**, 933-937 (1998).

[172] N. Robins, C. Savage and E. Ostrovskaya, Walls Memorial Volume, edited by H.J. Carmichael et al., (Springer 2000).

[173] For reasons of computational efficiency, we found it convenient to use G=12. This is because higher values produce faster atoms with shorter de Broglie wavelengths , requiring smaller spatial grid sizes, and hence bigger computations. For the preceding parameters g=9.8 ms^{-2} corresponds to G=132. Physically, low G values might correspond to the atom laser beam propagating in a tilted wave-guide. Alternatievly, a trap frequency about five times higher ($\omega \approx$ 625Hz) would make G=12 correspond to g=9.8 ms^{-2} .

[174] J. Schneider and A. Schenzle, Investigations of a two-mode atom-laser model, *Phys. Rev. A*, **61** 053611 (2000).

[175] Th. R. Taha and M. J. Ablowitz. Analytical and Numerical Aspects of Certain Nonlinear Evolution Equations: II. Numerical, Nonlinear Schrödinger Equation. *J. Comp. Phys.*, **55** 203-230 (1984).

[176] J. E. Lye, J. J. Hope, and J. D. Close, Nondestructive dynamic detectors for Bose-Einstein condensates, Phys. Rev. A 67, 043609 (2003).

[177] T. Bergeman, G. Erez, and H. J. Metcalf, Magnetostatic trapping fields for neutral atoms, *Phys. Rev. A*, **35** 1535-1546 (1987).

[178] L. Vestergaard Hau, B. D. Busch, C. Liu, Z. Dutton, M. M. Burns, and J. A. Golovchenko, Near-resonant spatial images of confined Bose-Einstein condensates in a 4-Dee magnetic bottle, *Phys. Rev. A*, **58** R54-R57 (1998).

[179] J. C. Maxwell, Treatise on Electricity, third ed. **2** 719 (1891).

[180] Ch. Fabry, *L'Eclairage électrique*, **17** 133 (1898).

[181] Ch. Fabry, *J. de Recherches du C.N.R.S.*, **9** 129 (1910).

[182] D. B. Montgomery, The generation of high magnetic fields, *Rep. Progr. Phys.*, **26** 69 (1963).

[183] M. Greiner, I. Bloch, T. W. Hnsch, and T. Esslinger, Magnetic transport of trapped cold atoms over a large distance, *Phys. Rev. A*, **63** 031401 (2001).

[184] H. J. Lewandowski, D. M. Harber, D. L. Whitaker, and E. A. Cornell, Simplified System for Creating a Bose-Einstein Condensate, *J. Low Temp. Phys.*, **132** 309 (2003).

[185] H. M. Wiseman and L. K. Thomsen, Reducing the Linewidth of an Atom Laser by Feedback, *Phys. Rev. Lett.*, **86** 1143 (2001).

[186] L. K. Thomsen and H. M. Wiseman, Atom-laser coherence and its control via feedback, *Phys. Rev. A*, **65** 063607 (2002).

[187] S. A. Haine, A. J. Ferris, J. D. Close, and J. J. Hope, Control of an atom laser using feedback, accepted *Phys. Rev. A* (2003).

[188] J. E. Lye, J. J. Hope, and J. D. Close, Rapid real-time detection of cold atoms with minimal destruction, accepted *Phys. Rev. A* (2003).

[189] S. Kuhr, W. Alt, D. Schrader, M. Mller, V.Gomer, D. Meschede, Deterministic Selivery of a Single Atom, *Science*, **293** 278 (2001).

[190] D. Schrader, S. Kuhr, W. Alt, M. Mller, V. Gomer, D. Meschede, An optical conveyor belt for single neutral atoms, *Appl. Phys. B*, **73** 819 (2001).

[191] S. Kuhr, W. Alt, D. Schrader, I. Dotsenko, Y. Miroshnychenko, W. Rosenfeld, M. Khudaverdyan, V. Gomer, A. Rauschenbeutel, and D. Meschede, Coherence Properties and Quantum State Transportation in an Optical Conveyor Belt, *Phys. Rev. Lett.*, **91** 213002 (2003).

[192] J. Williams, R. Walser, C. Wieman, J. Cooper, and M. Holland, Achieving steady-state Bose-Einstein condensation, *Phys. Rev. A*, **57** 2030 (1998).

[193] K. B. MacAdam, A.Steinbach, and C. Wieman, A narrow-band tunable diode laser system with grating feedback and a saturated absorption spectrometer for Cs and Rb, *Am. J. Phys.*, **60** 1098-1111 (1992).

[194] K. L. Corwin, Z-T. Lu, C. F. Hand, R. J. Epstein, and C. E. Wieman, Frequency-stabilized diode laser with the Zeeman shift in an atomic vapor, *Appl. Opt.*, **37** 3295-3298 (1998).

[195] C. I. Sukenik, H. C. Busch, and M. Shiddiq, Modulation-free laser frequency stabilization and detuning, *Opt. Comm.*, **203** 133-137 (2002).

[196] S. E. Park, H. S. Lee, T. Y. Kwon, and H. Cho, Dispersion-like signals in velocity-selective saturated-absorption spectroscopy, *Opt. Comm.* **192** 49-55 (2001).

[197] D. A. Shaddock, M. B. Gray, and D. E. McClelland, Frequency locking a laser to an optical cavity by use of spatial mode interference, *Opt. Lett.*, **24** 1499-1501 (1999).

[198] D. A. Shaddock, Advanced interferometry for gravitational wave detection, Chapter 11, Doctoral Thesis, Australian National University (2000). http://thesis.anu.edu.au/

[199] A. Thorne, U Litzen. and S. Johansson, Spectrophysics, Principles and Applications, Springer-Verlag (1999).

[200] O. Schmidt, K. -M. Knack, R. Wynands and D. Meschede, Cesium saturation spectroscopy revisited: How to reverse peaks and observe narrow resonances, *Appl. Phys. B*, **59** 167-178 (1994).

[201] Q. Chang, E. Jia and W. Sun, Difference Schemes for solving the Generalised Nonlinear Schrödinger Equation, *J. Comp. Phys.*, **148** 397-415 (1999).

[202] A. C. Newell and J. V. Moloney, *Nonlinear optics* (Addison-Wesley: 1992).

[203] W. Press, S. Teukolsky, W. Vetterling, and B. Flannery. *Numerical Recipes in C* (Cambridge University Press: 1992) Second Edition.